THEORETICAL AND NUMERICAL ANALYSIS OF FRACTURE OF SHAPE MEMORY ALLOYS

by

İbrahim Selçuk Hazar

B.S., Mechanical Engineering, Middle East Technical University, Turkey

M.S., Mechanical Engineering, Högskolan Dalarna, Sweden

Submitted to the Institute for Graduate Studies in
Science and Engineering in partial fulfillment of
the requirements for the degree of
Doctor of Philosophy

Graduate Program in Mechanical Engineering

Boğaziçi University

2014

to my parents and my uncle, Capt. Teoman Hazar

THEORETICAL AND NUMERICAL ANALYSIS OF FRACTURE OF SHAPE MEMORY ALLOYS

APPROVED BY:

Prof. Günay Anlaş (Thesis Supervisor) .....

Prof. Ziad Moumni (Thesis Co-supervisor) .....

Assist. Prof. C. Can Aydıner .....

Prof. Tarak Ben Zineb .....

Prof. Jean-Jacques Marigo .....

Assist. Prof. Wael Zaki .....

DATE OF APPROVAL: 14.11.2014

ACKNOWLEDGEMENTS

I would like to express my deep gratitude to Professors Günay Anlaş and Ziad Moumni, my research supervisors, for their patient guidance, very valuable and constructive critiques of this research work.

I would also like to thank Assist. Prof. Wael Zaki, for his advice and assistance in keeping my progress on schedule. I would like to thank my committee members Prof. Jean-Jacques Marigo and Assist. Prof. C. Can Aydıner and reporters of the thesis Prof. Tarak Ben Zineb and Prof. Han Zhao.

I am grateful to my colleagues Onur Yuksel, Osman Yuksel, Erdem Eren, Oana Zenaida Pascan and Gu Xiaojun for their helps, sharing and illuminating views related to my thesis. I would like to express a special thanks to MD. Elif Bato for her continual support and encouragement during my research.

Finally, I wish to thank my parents for their support and especially my uncle Ocean-Going Master Teoman Hazar for his guidance and encouragement throughout my study life.

ABSTRACT

THEORETICAL AND NUMERICAL ANALYSIS OF FRACTURE OF SHAPE MEMORY ALLOYS

The subject of this thesis is theoretical and numerical analysis of the fracture of SMAs. First, the size of the martensitic region surrounding the tip of an edge-crack in a SMA plate is calculated analytically using the transformation function proposed by Zaki and Moumni (Zaki and Moumni, 2007) together with crack tip asymptotic stress equations. Transformation regions calculated analytically and computationally are compared to experimental results available in the literature (Robertson *et al.*, 2007). Second, fracture parameters such as stress intensity factors (SIFs), J-integrals, energy release rates, crack tip displacements and T-stresses are evaluated. The objective at this point is to understand the effect of phase transformation on fracture behavior of an edge-cracked Nitinol plate under Mode I loading. In the FE analysis of the edge-cracked plate under Mode I loading, the ZM model as well as the built-in model (Auricchio *et al.*, 1997) are used. Third, steady-state crack growth in an SMA plate is analysed. To this end, Mode I steady-state crack growth in an edge-cracked Nitinol plate is modeled using a non-local stationary method to implement the ZM model in Abaqus. The effects of reorientation of martensite near the crack tip, as a result of non-proportional loading, on fracture toughness is also studied. Finally, phase transformation regions are calculated analytically around the tip of an SMA specimen under Mode III loading. The analytical derivations are carried out first using a method proposed by Moumni (Moumni, PhD Thesis, École Nationale des Ponts et Chaussées, 1995) which relies on mapping the equations of the boundary value problem to the so-called "hodograph" plane. The influence of coupling on the extent of the phase transformation regions and on temperature distribution within the material is then investigated numerically.

ÖZET

ŞEKİL HAFIZALI ALAŞIMLARIN KIRILMASININ TEORİK VE NUMERİK ANALİZİ

Bu tez çalışmasının konusu şekil hafızalı alaşımların (ŞHA) kırılma mekaniğinin teorik ve numerik olarak analiz edilmesidir. İlk olarak, Zaki ve Moumni (Zaki and Moumni, J. Mech. Phys. Sol, 2007) tarafından geliştirilen transformasyon fonksiyonu çatlak ucu asimptotik gerilme denklemleri ile birlikte kullanarak kenar çatlak ucu çevresindeki martensit bölgesinin büyüklüğü, analitik olarak hesaplanmıştır. İkinci kısımda, gerilim şiddet çarpanları (GŞC), J-integrali değerleri, enerji salınım oranları, çatlak ucu açılma yer değiştirmeleri ve T gerilmeleri gibi kırılma parametreleri hesaplanmıştır. Bu noktada amaç, kenar çatlaklı Nitinol plakadaki faz transformasyonunun kırılma davranışına etkisini anlamaktır. Kenar çatlaklı plakanın sonlu elemanlar analizinde, Abaqus'e aktarılan Zaki- Moumni (ZM) modeli ve Abaqus'un içinde yer alan ve Auricchio modelini (Auricchio *et al.* Comp. Meth. Appl. Mech. Eng., 1997) temel alan ŞHA modeli kullanılmıştır. Üçüncü olarak, ŞHA plakada durağan durum çatlak ilerlemesi analiz edilmiştir. Bu amaçla bölgesel olmayan denklemler kullanılarak kenar çatlaklı plakada mod I kararlı durum çatlak ilerlemesi modellenmiştir. Oransal olmayan yüklemeden ötürü oluşan martensit'in çatlak ucunda yeniden oryantasyonunun kırılma tokluğuna etkileri de çalışılmıştır. Son olarak faz transformasyonu bölgeleri mod III yükleme altında analitik olarak hesaplanmıştır; ilk aşamada Moumni tarafından uygulanan (Ziad Moumni, Doktora Tezi, 1995) "hodograf" metodu kullanılarak kısmi diferansiyel eşitlik hodograf düzleminde doğrusal sınır değer problemine dönüştürülmüş ve çatlak ucundaki faz transformasyonu bölgeleri analitik olarak hesaplanmıştır. Analizin sonucunda termomekanik olarak tümüyle eşlenmiş transformasyon bölgesi ve çatlak ucu çevresindeki gizil isinin neden olduğu sıcaklık artısı numerik olarak hesaplanmıştır.

TABLE OF CONTENTS

ACKNOWLEDGEMENTS iii
ABSTRACT iv
ÖZET v
LIST OF FIGURES viii
LIST OF TABLES xiii
LIST OF SYMBOLS xiv
LIST OF ACRONYMS/ABBREVIATIONS xvi
1. INTRODUCTION 1
1.1. Phase Transformation in Shape Memory Alloys 1
1.2. Fracture Mechanics of SMAs 5
1.3. Review of Constitutive Models of SMAs 14
1.4. Industrial Applications of Shape Memory Alloys 22
1.5. Research Objectives 24
1.6. Outline of the Thesis 25
2. EVALUATION OF TRANSFORMATION REGION AROUND CRACK TIP IN SHAPE MEMORY ALLOYS 27
2.1. Introduction 27
2.2. Problem Statement and Formulation 34
2.3. Evaluation of Stress Intensity Factor 36
2.4. Evaluation of Transformation Region 38
2.5. Results and Conclusions 40
3. INVESTIGATION OF FRACTURE PARAMETERS OF SHAPE MEMORY ALLOYS UNDER MODE I LOADING 43
3.1. Introduction 43
3.2. Problem Statement and FEA 48
3.3. Fracture Parameters 53
3.3.1. J-Integral 53
3.3.2. Discussion on Strain Energy Stored 55

3.3.3. Stress Intensity Factor Calculations Using Strain Energy Release Rate . . . 57
3.3.4. Stress Intensity Factor Calculations Using Full Displacement Field and Asymptotic Equations . . . 58
3.3.5. Calculating the Extent of Transformation Region Using T-Stresses 61
3.3.6. Crack Tip Opening Displacement . . . 63
3.4. Crack Initiation and Stability of Crack Growth . . . 64
3.5. Fracture Toughness . . . 66
3.6. Summary and Conclusions . . . 69
4. MODELING OF STEADY-STATE CRACK GROWTH IN SHAPE MEMORY ALLOYS USING A STATIONARY METHOD . . . 72
4.1. Introduction . . . 73
4.2. Problem Statement . . . 77
4.3. Solution Methodology . . . 82
4.4. Results and Conclusions . . . 91
5. MODELING OF ANTI-PLANE SHEAR CRACK IN SMAS INCLUDING THERMOMECHANICAL COUPLING . . . 95
5.1. Modeling of Phase Change . . . 96
5.2. Anti-plane Shear Crack in SMAs . . . 101
5.3. Problem Statement . . . 102
5.4. Hodograph Method . . . 106
5.5. Solution of the Problem . . . 112
5.6. Thermomechanical Coupling . . . 115
5.7. Derivation of Heat Equation . . . 119
5.8. Numerical Analysis . . . 120
5.9. Results and Discussion . . . 122
6. SUMMARY & CONCLUSION . . . 130
REFERENCES . . . 134

LIST OF FIGURES

Figure 1.1. Stress-temperature diagram for a SMA (NiTi). 2

Figure 1.2. Stress-strain-temperature behavior of a SMA (NiTi). 3

Figure 1.3. Stress-strain behavior of a SMA (NiTi). 4

Figure 2.1. (a) Edge cracked SMA CT specimen $B = 0.4$ mm (thickness), $W = 10.8$ mm, $a = 5.4$ mm, $h = 6.4$ mm. (b) Uniaxial stress-strain behavior of superelastic Nitinol. 35

Figure 2.2. Contours of u_y.The crack tip is located at the origin and the co-ordinates x and y are normalized by W Dashed lines with values in boxes are FE results, solid lines are from least squares fit of Equation 2.27 to FE results. 38

Figure 2.3. (a) Contour plot of normalized opening stress, $\frac{\sigma_{yy}}{\sigma_0}$ (σ_0, far field applied stress), green lines: full field finite element solution, black lines: asymptotic field. Red line $\zeta = 1$, and the region between red and blue lines, $0 < \zeta < 1$. Crack tip is located at the origin. (b) close up view of $\frac{\sigma_{yy}}{\sigma_0}$ near the crack tip. 39

Figure 2.4. Martensitic region around crack tip. 40

Figure 2.5. Transformation function, $F_\zeta = 0$, vs principle stresses. 42

Figure 2.6. Effect of SIF on transformation region. 42

Figure 3.1. (a) Edge-cracked thin SMA plate, (b) Geometry of the 2-D edge-cracked specimen, (c) Mesh of 2-D edge-cracked specimen, (d) Mesh configuration close to the crack tip ($H = 100\ mm$, $W = 100\ mm$ and $a = 20\ mm$). 49

Figure 3.2. (a) Stress-strain graph, (b) stress-temperature graph of Nitinol [1]. 50

Figure 3.3. Stress-strain relation simulated in Abaqus using both ZM and Auricchio Models. 51

Figure 3.4. (a) Phase transformation regions, $\zeta = 0^+$, (b) Full martensite region, $\zeta = 1$, ($a/W = 0.40$). 52

Figure 3.5. Transformation region, red ($\zeta = 1$), green ($0 < \zeta < 1$) and J-Integral contours (white and gray), ($a/W = 0.40$). 52

Figure 3.6. Martensite fraction, ζ along the crack tip in positive x direction as shown in Figure 3.2, u=0.1 mm. 53

Figure 3.7. Comparison of σ_{yy} contours. 54

Figure 3.8. Angular variation of the $\frac{\sigma_{yy}}{\sigma_T}$ where σ_T is the average transformation stress along a radial path ($r = 0.18mm$). The crack tip is located at the origin. ($a/W = 0.40$ and $u = 0.1\ mm$). 55

Figure 3.9. Solid lines are the phase transformation start boundary ($\zeta = 0^+$), dotted lines represents full martensite region ($\zeta = 1$), dashed lines are J-integral curves, circular gray curves are J-integral calculation contours ($a/W = 0.40$ and $u = 0.1\ mm$). 56

Figure 3.10. J-integrals calculated using Auricchio's model for different a/W ratios, u=0.1mm. 57

Figure 3.11. J-integrals calculated using ZM model for different a/W ratios, u=0.1mm. 57

Figure 3.12. Change of ALLSE (dotted line), ALLPD (solid line) and ELPD (dash line) during loading, ($u_T = 0.10\ mm$, $a/W = 0.40$). 58

Figure 3.13. (a) SIF calculated using G vs. u (b) SIF calculated using full field displacement equation vs. u. 59

Figure 3.14. Displacement field around the crack tip calculated using ZM model, a/W =0.40. 60

Figure 3.15. Comparison of stress intensity factors normalized by K_I^{aus}, which is the SIF calculated for a linear elastic material with material properties identical to NiTi in the austenitic phase. (ZM: Zaki–Moumni model A: Auricchio's Model). 60

Figure 3.16. Red line represents the fully martensite region, blue and green lines are contour plots of $\sigma_{ij}^A/\sigma_{app}$ and $\sigma_{ij}^{FE}/\sigma_{app}$ respectively, and dashes black lines are e contours (a/W =0.40, $u = 0.1\ mm$,σ_{app} is the applied load). 61

Figure 3.17. Comparison of the extent of transformation region r ($\theta = 0$) normalized by crack length a calculated using different methods. . . . 63

Figure 3.18. (a) Crack face opening profiles for increasing u. Half of the CTOD is measured from the intercept of 45^o line (dashed line starting from the crack tip) and the crack profile (b) CTOD values. 64

Figure 3.19. d_n values. 64

Figure 3.20. Effect or transformation strain on crack growth stability. 65

Figure 3.21. T-stresses normalized with the average transformation stress (σ_T) vs. applied displacement u/a (a/W =0.40). 68

Figure 3.22. Crack face opening profiles for different a/W, $u = 0.10\ mm$. Red curves represents ZM model and the blue curves are those out of Auricchio's model. 69

Figure 4.1. Crack growth in an infinitely long plate. 78

Figure 4.2. Schematical representation of solution methodology. 82

Figure 4.3. Finite element model. 83

Figure 4.4. Finite element mesh. 83

Figure 4.5. Integration point numbering. 84

Figure 4.6. Effect of reorientation and reversible transformation on transformation region. (a) plane stress (b) plane strain. 90

Figure 4.7. Effect of reorientation and crack growth on CFOD. (a) plane stress (b) plane strain. 91

Figure 4.8. σ_{yy} ($\sigma_{yy} = 580MPa$ is the average transformation plateau stress), contour plots under (a) plane stress (b) plane strain. 92

Figure 4.9. J-integrals calculated for cases II and III under plane stress and plane strain conditions. J_∞ is the J integral far from the crack tip where the material is in austenite phase. 93

Figure 5.1. Schematic representation of the coordinate system attached to the crack tip. 102

Figure 5.2. The domains of validity of the solution. 113

Figure 5.3. Free energy functions defined for each phase. 116

Figure 5.4. Martensite transformation region, thermomechanical coupling is not included, $T_0 = 343\ K$. 118

Figure 5.5. The geometry of the problem and the boundary conditions ($W = 100\ mm$, $H = 100\ mm$, $a = 50\ mm$). 122

Figure 5.6. Algorithm of thermo-coupling analysis for anti-plane loading. . . . 123

Figure 5.7. ζ contours. $\zeta = 1$ is the inner circle, $\zeta = 0.5$ is the middle circle, $\zeta = 1\times10^{-5}$ represents the outer circle. Colours: cyan: $\dot{k^{\infty}} = 2.56\times 10^{-5}$ (1/s), red: $\dot{k^{\infty}} = 1.280 \times 10^{-5}$ (1/s), blue: $\dot{k^{\infty}} = 0.64 \times 10^{-5}$ (1/s), green: $\dot{k^{\infty}} = 0.43\times10^{-5}$ (1/s), black: $\dot{k^{\infty}} = 0.32\times10^{-5}$ (1/s) and yellow curve is when the latent heat generation is neglected. . 124

Figure 5.8. Temperature increase due to thermomechanical coupling. 125

Figure 5.9. Isotherms around the crack tip. 126

Figure 5.10. The temperature contour plot where only intrinsic dissipation is taken into consideration and the latent heat is neglected. 127

Figure 5.11. The change of the area of transformation region, $\Delta S_{tr}/S_{cp}$, where $\Delta S_{tr} = S_{iso} - S_{cp}$, versus the applied load $\dot{k^{\infty}}$. 128

LIST OF TABLES

Table 3.1. Material parameters used in ZM model [2]. 50

Table 3.2. Material parameters used in Auricchio's model [3]. 51

Table 3.3. Comparison of SIFs.(Units: K $(MPa.mm^{1/2})$, $G \approx \frac{\Delta U}{\Delta A}$ and J $(\frac{mJ}{mm^2})$, A : Auricchio Model, ZM: Zaki Moumni model. 62

Table 3.4. K_I^G, determined Effect of volumetric strain on toughness. 67

Table 3.5. Comparison of SIFs calculated using Auricchio and ZM models to the SIFs of homogeneous plate. 68

Table 4.1. Material model parameters. 87

Table 5.1. Material properties used in the analysis. 118

LIST OF SYMBOLS

a, b, Γ	Material parameter of ZM model
A_s	Austenite start temperature
A_f	Austenite finish temperature
E_A	Young's modulus of austenite
(E^A_{ijkl})	Elastic stiffness tensor of austenite
E_M	Young's modulus of martensite
(E^M_{ijkl})	Elastic stiffness tensor of martensite
F^f_ζ	Forward transformation function of phase change
F^r_ζ	Reverse transformation function of phase change
G	Energy release rate
J	J-Integral
K_{TIP}	Crack tip SIF
K_C	Fracture toughness
K_{APP}	Far-field SIF
K_{TRAN}	SIF change due to transformation
M_d	Martensite desist temperature
M_s	Martensite start temperature
M_f	Martensite finish temperature
s	Entropy
T	Temperature
U	Internal energy
$U(e_{ij})$	Free energy of austenite
$V(f_{ij})$	Free energy of martensite
det()	Determinant
α, β, κ	Material parameters of ZM model
B	Bulk modulus
λ_m, π_n	Lagrange multiplier
$\mathcal{L}$	Lagrangian

ν	Poisson's ratio
μ_1	shear modulus of austenite
μ_2	shear modulus of martensite
(σ_{ij})	Cauchy stress tensor
(σ_{ij}^{d})	Deviatoric part of stress tensor
σ_{det}^{f}	Orientation finish stress
σ_{det}^{s}	Orientation start stress
σ_{Mf}	Martensite finish stress
σ_{Ms}	Martensite start stress
σ_{Af}	Austenite finish stress
σ_{As}	Austenite start stress
(ϵ_{ij}^{d})	Deviatoric part of strain tensor
(ϵ_{ij}^{ori})	Orientation strain tensor
ϵ_{ori}^{0}	Maximum transformation strain in tension
(ϵ_{ij}^{A})	Local strain tensor of austenite
(ϵ_{ij}^{M})	Local strain tensor of martensite
Ψ	Helmholtz free energy
Ψ_c	Thermodynamic potential of constraints
$\Re_H$	Hodograph plane
u_i	Displacement vector
ξ	Material parameter of ZM model
ζ	Martensite fraction

LIST OF ACRONYMS/ABBREVIATIONS

CT	Compact tension
CTOD	Crack tip opening displacements
CFOD	Crack face opening displacements
DIC	Digital image correlation
DSC	Differential scanning calorimeter
FE	Finite element
FEA	Finite element analysis
FEM	Finite element method
FSMA	Ferromagnetic shape memory alloys
LEFM	Linear elastic fracture mechanics
NiTi	Nickel Titanium alloy
NOL	Naval Ordenance Laboratory
PDE	Partial differential equation
RVE	Representative volume element
SIF	Stress intensity factor
SMA	Shape memory alloy
SME	Shape memory effect
UMAT	User defined material subroutine
VCE	Virtual crack extension
ZTC	Zirconia–Toughened Ceramics
ZM	Zaki–Moumni model

1. INTRODUCTION

1.1. Phase Transformation in Shape Memory Alloys

Shape Memory Alloys (SMAs) are smart materials that are capable of recovering their original shape after severe inelastic deformations when their temperatures are increased. In 1932, Ölander [4] discovered such a memory effect in AuCd and in 1938, Greninger and Mooradian [5] discussed shape memory effect (SME) in CuZn alloys. In 1962, William J. Buehler (and Wiley R. C.), from Naval Ordnance Laboratory (NOL), discovered the shape memory behavior of Nickel Titanium (NiTi) alloy [6, 7], which upon loading or changing temperature underwent solid–to–solid diffusionless phase transformation between two phases: parent phase called "austenite", stable at high temperature and low stress, and product phase "martensite", stable at low temperature and high stress. The alloy was named "*Nitinol*" (combination of "*NiTi*" and "*NOL*").

As shown in Figures 1.1 and 1.2, when the temperature of the alloy is decreased below the martensite transformation start temperature (M_s) (from state 1 to 3), under constant stress below orientation start stress σ^s_{det}, SMA starts to transform from austenite to martensite gradually. During this transformation, different variants form by twining. This mechanism is known as self-accommodation of the crystal structure. A self-accommodated microstructure means that martensitic variants are arranged in such a way that no observable deformation takes place. The variants formed in this self–accommodated microstructure have the same free energy [8]. When the self-accommodated martensite is heated up to austenite start temperature (A_s), the martensite phase transforms back to austenite (from state 3 to 1).

When the specimen is loaded under constant temperature (loading path 3 to 2 in Figure 1.1), variants rearrange themselves through orientation. At this stage, the microstructure consists predominantly of a single variant and martensite is said to be "detwinned". In detwinned martensite, only one of the variants exists and the formation of this variant depends on thermomechanical loading path. At this stage, if

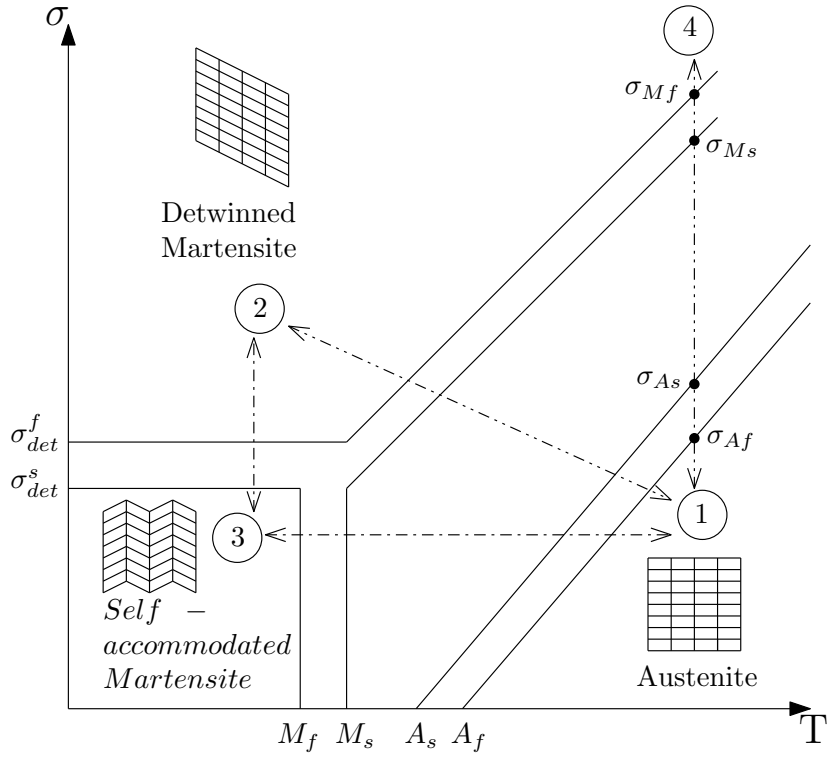


Figure 1.1. Stress-temperature diagram for a SMA (NiTi).

the alloy is heated up to a certain temperature, the detwinned martensite transforms back to austenite and the specimen returns back to its original shape (from state 2 to 1 in Figure 1.1). Almost all the strain induced during martensite orientation is recovered by heating. This behavior is called the shape memory effect.

When the NiTi specimen is at temperatures higher than the austenite finish temperature (A_f), it transforms to martensite and upon unloading the deformation in the material is recovered. The ability of SMAs to recover inelastic deformation by mechanical unloading is referred to as "superelasticity" or "pseudo-elasticity". According to Otsuka and Wayman [9], pseudo-elasticity is an apparent plastic deformation that is recovered from when the material is unloaded at a constant temperature irrespective of its origin. In addition, Otsuka and Wayman [9] stated that pseudo-elasticity is a general term that involves both "superelasticity" and "the rubber-like effect". According to earlier research [4], "the rubber-like effect" is defined as the transformation that occurs by the reversible movement of twin boundaries in the martensitic phase [9].

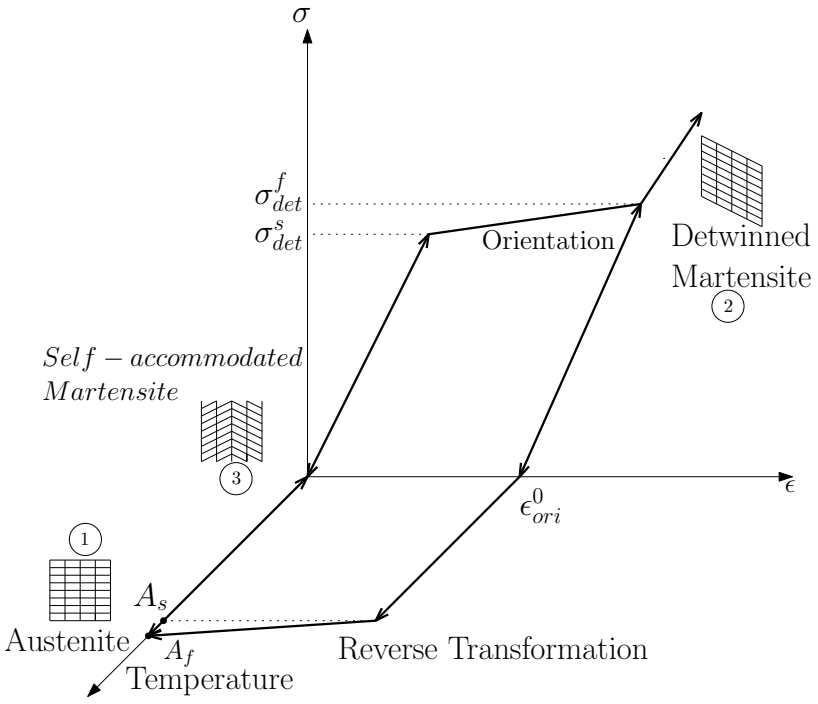


Figure 1.2. Stress-strain-temperature behavior of a SMA (NiTi).

Throughout this thesis, the term "superelasticity" is used to define stress–induced and reversible phase transformation between austenite and martensite phases.

In superelasticity, the material should be deformed above A_f, but below a certain temperature called martensite desist temperature (M_d) [10], that is the highest temperature over which stress–induced martensite can no longer form. In superelastic loading, there is a difference between forward transformation ($\sigma_{Ms} \rightarrow \sigma_{Mf}$) and backward transformation ($\sigma_{As} \rightarrow \sigma_{Af}$) stresses. This difference gives rise to a hysteresis loop (see Figure 1.3). Figure 1.3 shows that during superelastic deformation, SMA starts to deform linear elastically with an elastic modulus that is equal to that of austenite, E_A, until the stress reaches σ_{Ms}. When σ_{Ms} is exceeded, the martensitic transformation starts and the volume fraction ζ of martensite continues to increase until it reaches 1 when the stress reaches σ_{Mf}. For higher stress, the material behaves elastically again until yielding. If the stress is decreased before reaching the yield strength of the material, the stress-strain curve follows the same path up to σ_{As}, which is below σ_{Mf}, and follows a different path from that of forward transformation as shown in Figure 1.3.

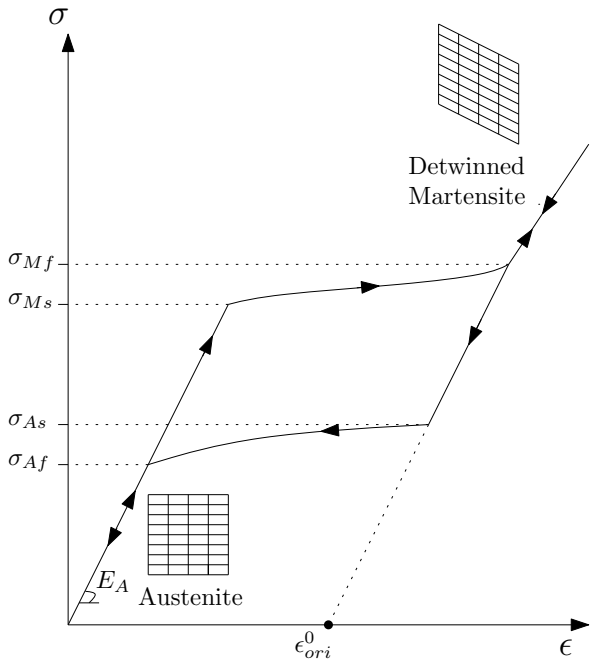


Figure 1.3. Stress-strain behavior of a SMA (NiTi).

If unloading continues, the stress-strain curve follows a transformation plateau until σ_{Af} then unloads elastically as austenite as shown in Figure 1.3. At the end of the transformation significant strains (5 %-6 %) can be recovered.

In Figure 1.1, the path 1–3–2–1 summarizes the shape memory effect and the path 1–4 represents the superelastic behavior. The explanations given above indicate that the transformation temperatures, A_s, A_f, M_s, M_f, play an important role in the characterization of the constitutive behavior of an SMA. These temperatures are measured using a Differential Scanning Calorimeter (DSC) [11].

In this study, the effect of superelastic phase transformation on fracture of NiTi is investigated. For this purpose two, internal state variables are used to describe the superelastic material behavior of Nitinol: the volume fraction of martensite (ζ) that is induced by mechanical loading and the martensite orientation strain tensor (ε_{ij}^{ori}). It is known that the reversible, pseudo-elastic deformation of SMAs is mainly due to the orientation of martensite variants. Consequently, the creation of martensite by thermal loading does not induce any macroscopic strains except thermal strains, in

the absence of stress. This chapter follows with a comprehensive literature survey on fracture behavior of SMAs and a review of constitutive models developed for SMAs which are available in the literature. Then the next section gives a brief overview of the engineering applications of SMAs and finally, the research objectives of this work are defined together with an outline of the thesis.

1.2. Fracture Mechanics of SMAs

After the discovery of the unusual thermomechanical properties of NiTi, its use in engineering applications is increased. In parallel to this development, the number of studies investigating fracture properties of NiTi started to increase as well. The motivation for this study is to improve the fundamental understanding of fracture in SMAs. In the following paragraphs, a summary of studies done by previous researchers on fracture mechanics and fracture toughness of SMAs are given in a chronological order.

One of the earliest discussions on the effect of phase transformation on stress intensity factor (SIF) and toughness is done by McMeeking and Evans [12]. According to the authors, if a particle undergoes stress-induced martensitic transformation its toughness increases due to the resulting residual strain field that restricts crack opening. The increase in toughness is then calculated from crack tip stress intensity change using Eshelby's [13] technique.

Stam and van der Giessen [14] investigated the influence of partial or full reversibility of stress-induced phase transformation on toughness during crack growth in zirconium ceramics and SMAs. In their finite elements analyses, they used the model of Sun and Hwang [15, 16] and simulated crack propagation considering small-scale transformation around the crack tip. They related crack tip SIF, K_{TIP}, and SIF corresponding to the applied Mode I loading, K_{APP}, by the equation K_{APP}/K_{TIP}=1-Δ K_{TIP}/K_C where K_C is the fracture toughness. They considered the material inside the fully transformed region as linear–elastic martensite and the region between fully transformed martensite and austenite as partially transformed non-linear. They simulated

the crack growth using a node release technique [17] and allowed the crack to grow when $K_{APP} = K_{TIP}$. Upon crack advance, the transformed material started to evolve in the wake region and the crack tip is shielded by transformation strain accumulated there. In addition to that, the authors investigated the influence of reversible phase transformation during crack growth and stated that not all the toughness increase due to phase transformation is lost during crack growth by means of reverse transformation. An important finding of this work was that the increase in toughness was higher in SMAs compared to zirconium ceramics.

In 1998, Birman [18] studied Mode I fracture of an SMA plate using the constitutive model of Tanaka [19] and crack tip asymptotic stress equations of LEMF to calculate the size of the phase transformation region and the effect of phase transformation on SIF. He found that the effect of phase transformation on the stress intensity factor is relatively small and concluded that the magnitude of the stress intensity factor can be evaluated using the properties of austenite only.

McKelvey and Ritchie [20] investigated experimentally, the effect of stress-induced martensite on resistance to crack growth in SMAs under dynamic loading in 1999. They showed that the fatigue crack growth resistance of NiTi is lowest compared to other biomedical implant alloys.

Simha [21] studied the fracture toughness of zirconium ceramics. According to Simha, the toughening of the material is mainly caused by the energy stored by the transformed inclusions in the wake of a propagating crack. He proposed to evaluate the steady-state toughening in zirconium ceramics by determining the difference in J-integrals at far field and at crack tip. He stated that his model can be applied to pseudo-elastic crack propagation in polycrystalline shape memory alloys.

The effect of phase transformation on the toughening in SMAs has been studied analytically and numerically by several other researchers. Yi and Gao [22] studied the fracture toughening mechanisms in SMAs as a result of stress-induced phase transformation under Mode I loading. In their analysis, they used Eshelby's method

[13], weight functions and Sun and Hwang's [15] constitutive model to investigate the transformation region around static and steadily advancing cracks. They defined the change in toughness with an approach similar to Stam and van der Giessen [14], using $\Delta\ K_{TIP}=K_\infty$ - K_{TIP}, K_∞ being the far field SIF. They determined the boundary of the transformation region by taking the average value for K, $K = (\ K_\infty + K_{TIP})\ /\ 2$, as calculated by Evans [23]. They stated that martensite transformation reduces the crack tip SIF and increases fracture toughness. Moreover, their results also showed that K_{TIP} decreased when the temperature is increased. They indicated that a sharp decrease in crack tip SIF can be obtained by using a material for which the difference in elastic stiffness between austenite and martensite is significant.

Not all the researchers have agreed on the conclusion that fracture toughness increases by phase transformation: some of the researchers put forward the claim that due to negative volume change during phase transformation, toughness of the material reduces. Yan *et al.* [24] studied quasi-statically growing crack using FEA to see the effect of stress-induced martensite transformation on fracture behavior of superelastic SMAs and compared their results to those obtained in the case of phase transformation in zirconium ceramics. They defined crack tip SIF as $K_{TIP} = K_{APP} + K_{TRANS}$. Once the transformation region is identified, they calculated K_{TRANS} using the equation given by Hutchinson [25] and McMeeking and Evans [12]. In their FEA, they used the node release technique assuming that the crack growth occurs under given K_{APP} without knowing the toughness of the material, K_C. In their calculations, they discovered that there is a volume contraction during austenite to martensite transformation. They stated that negative volumetric strain increases the effective SIF near an advancing crack tip and reduces the toughness. They assumed a partial reverse transformation in the wake region and stated that the effect of reverse transformation in the wake region is negligible. The results they obtained showed that volume-expanding phase transformation may increase toughness but reverse transformation in the wake can reduce this effect in a considerable amount.

In a following study in 2003, Yan *et al.* [26] studied the effect of plasticity on stress-induced transformation. They modified the constitutive model of Auricchio *et al.* [3]

and Lubliner and Auricchio [27], using Drucker–Prager yield function and considered the effect of plasticity and volume change during transformation. The authors showed that a fully martensite region can be observed around the crack tip, meaning that the influence of hydrostatic stress does not inhibit phase transformation completely.

After the discovery of the superior characteristics of ferromagnetic SMAs (FSMAs), work on fracture mechanism of those alloys is attracting increasing interest from the scientific community. Xiong *et al.* [28] studied thermally induced fracture in Ni–Mn–Ga, NiTi and Cu–Al–Ni single crystal. The results of their X–Ray diffraction experiments showed that the existence of twinned variants are the main driving force of the crack network leading to fracture. This study is mainly important to see the difference of fracture behavior between single crystal and polycrystal SMAs.

In NiTi, martensite forms around the crack tip at the early stages of loading and the geometry of the crack tip plays an important role in evolution of the martensite phase. For this reason, different notch shapes are studied to see the effect of notch geometry on toughness. Wang [29] investigated the effect of notch geometry on phase transformation and fracture toughness using NiTi compact tension (CT) specimens with different notch geometries under mode I loading. He defined NiTi as an elastic–plastic material by digitizing stress–strain data in Abaqus. He calculated phase transformation, and plastically deformed region boundaries under Mode I loading. He determined that changing the notch shape from blunt to acute increases stresses, and changes crack propagation from unstable to stable state. His results indicated that the size of the martensitic region around the tip of a sharp cracked and acute notched specimens are similar in shape but smaller than those of blunt notched specimens. As expected, around tip of sharply cracked specimen the plastic zone is observed at low stress levels. On the other hand, for bluntly notched specimens, higher load is necessary to form the same size of the plastic zone. Using a similar approach, Wang [30] studied the effects of phase transformation on fracture toughness in an SMA CT specimen under Mode I loading, and stated that the notch tip is blunted by transformation strain which causes the release of notch tip stresses as a result fracture toughness increases. In another study, Wang [31] calculated stress distribution around the tip of an

edge-cracked NiTi plate under Mode I loading and also of a linear elastic material with identical material properties with NiTi in the martensite phase. He used the stress–strain relation for NiTi given by McKelvey and Ritchie [20] and for the untransformed martensite he used the same curve without the transformation plateau. He digitized the two curves and used as an input to Abaqus. He found that martensite transformation increases the load needed to produce plastic deformation at the notch tip and decreases the maximum normal stress and plastic strain near the tip. He concluded that when the applied load increases, first partially and then fully martensitic zones develop around the crack tip, and afterwards a plastic deformation follows inside the fully martensitic zone. The plastic deformation tends to increase the resistance to crack nucleation and propagation in fully transformed martensite region which then increases the fracture toughness. He demonstrated that martensite transformation suspends crack nucleation and propagation at the tip, resulting in a 47 % increase in fracture toughness.

Standard tests for NiTi [11, 32, 33] have been used by some researchers to measure the material properties of SMA. The fracture toughness of SMAs is studied using standard experiments developed for commercial metals by some researchers. In 2008, Wang *et al.* [34] obtained the fracture toughness by performing experiments on CT specimens pre-cracked under fatigue load. They calculated the fracture toughness of the specimen to be as 39.4 MPa. Their observations showed that, a region in the proximity of crack tip is partly transformed to martensite during fatigue pre-crack process. They showed that there is always a small area around the crack tip that is fully transformed to martensite if the crack growth is fast. They concluded that the shape of the martensite transformation region resembles to plastic transformation region and can be modeled using methods similar to those of incremental plasticity.

Robertson *et al.* [35] used a more advanced method, X-ray diffraction to obtain the strain field around the tip of an edge–cracked thin NiTi specimen under Mode I loading. They showed that the redistribution of stress field because of phase transformation reduces stresses near the crack tip and increases the fracture resistance.

Daly *et al.* [36] used digital image correlation (DIC) to calculate the strain fields

in an edge-cracked thin NiTi sheet under Mode I loading, they calculated SIF using LEFM and obtained an empirical expression between the extent of the transformation region and K_I. They stated that a relatively high value of fracture toughness (K_C) for NiTi indicates a contribution of phase transformation to toughening of the alloy.

Gollerthan *et al.* [37] performed displacement controlled experiments using NiTi CT specimen and measured applied far–field load, P, to calculate the critical stress intensity factor using the empirical relation, $K = \frac{P}{B\sqrt{W}} f(a/W)$, where B, W and $f(a/W)$ are obtained from experiments given by the standards [38]. They used the calculated SIF and Irwin's plasticity corrected equation to estimate the length of the phase transformation zone along crack tip. Results confirmed that the length they calculated qualitatively agreed with the experimental observations.

Xiong and Liu [39] studied thermally induced fracture in Ni–Mn–Ga, NiTi, and Cu–Al–Ni and they proposed an analytical solution to calculate SIF increase around the crack tip. They used Irwin's correction together with the transformation function proposed by Tanaka and Sato [40] to find the extent of plastic region and phase boundaries analytically. They extended the work of Birman [18] considering stress redistribution as a result of phase transformation. They calculated that the volume change during martensitic transformation is composition dependent and can be either positive or negative. They found that stress redistribution occurs around the crack tip, which leads to an increase in crack tip SIF and a decrease in fracture toughness. According to their results, the effect of transformation region on SIF around the crack tip is a function of temperature and it is independent of crack size.

Freed and Banks-Sills [41] presented a FEA on transformation toughening behavior of a slowly propagating crack in an SMA plate under Mode I loading assuming small-scale transformation region around crack tip. To find the transformation region around the crack tip, they used the transformation surface equation proposed by Panoskaltsis *et al.* [42] and crack tip asymptotic stress equations. The transformation zones that they determined near the crack tip were similar to the shape of the plastic zone in plastically deformed materials. Furthermore, they used a cohesive zone model

to simulate crack growth using finite elements. They claimed that the choice of cohesive strength has a great influence on toughening behavior. They observed an increase in critical steady–state SIF due to phase transformation and mismatch between austenite and martensite elastic moduli. Their results lend support to the claim that reversible phase transformation reduces the amount of toughening in the alloy.

Overall, the studies summarized thus far highlight the need for accurate determination of the phase transformation region around the crack tip to investigate fracture parameters. Lexcellent and Thiebaud [43] presented an analytical approach using the constitutive model of Raniecki and Lexcellent [44], also used in Lexcellent and Blanc's [45] paper, together with asymptotic crack tip stress equations to determine the transformation region around the crack tip under Mode I loading. Using an equation similar to the one proposed by Freed and Banks-Sills [41], they calculated an average value of SIF, $(K_I^{app} + K_I^{tip})/2$, where K_I^{app} is the applied SIF and K_I^{tip} is the SIF governing the region near crack tip. Their results showed a big difference with the experimental results of Robertson *et al.* [35]. Falvo *et al.* [46] used both $\sigma_y = K_I/\sqrt{2\pi r}$ and Irwin's plasticity corrected formula to predict the extent of the stress-induced martensitic transformation. They compared their analytical results with FEA results, and showed that using Irwin's correction yields results closer to FEA results. Ma [47] proposed an analytical approach using Green's function to find the effect of martensitic and ferro–elastic transformation on fracture toughness in a semi-infinite crack under plane stress. His formulation, indicating the changes in stress intensity factor because of phase transformation, was in agreement with the result obtained by McMeeking and Evans [12].

Falvo *et al.* [46] studied the evolution of stress-induced martensitic transformation in front of the crack tip in a NiTi alloy. They used both $\sigma_y = K_I/\sqrt{2\pi r}$ and $\sigma_y = K_{Ieff}/\sqrt{2\pi(r - r_y)}$ to predict the extent of transformation region along the crack in a NiTi under plane stress. They compared their prediction to results they obtained using MARC and showed that results closer to experimental measurements are obtained when Irwin's plasticity corrected formula is used. Their model could not estimate the effective crack length when crack growth occurs. They stated that the martensite

volume fraction can be estimated from the distributions of the equivalent plastic strain. They concluded that the extent of transformation start region decreases rapidly with increasing temperature but the extent of fully martensitic region is nearly constant. In a very similar way to their previous work [46], Maletta and Furgiuele [48] proposed an analytical method, which is in agreement with the performed FEA to predict the extent of phase transformation region using Irwin's corrected formulation in combination with $K_I = \sigma^{\infty}\sqrt{\pi\alpha}$ in an infinite NiTi plate having a central crack under Mode I loading. In the following study, Maletta and Young [49] extended the previous work [48] to plane strain conditions and compared their results to experimental results of Gollerthan *et al.* [50]. They observed that experimentally calculated phase transformation length was between the lengths they calculated for plane stress and strain. Their FE results showed that increasing transformation strain and decreasing plateau stress increases the size of the transformation region. In a later study, Maletta and Furgiuele [51] calculated the extent of phase transformation region using their previous approach [48] and two different SIFs: one for austenitic region and another one for the transformed martensitic region near the crack tip. They calculated that the martensitic or crack tip SIF is always smaller than the LEFM predictions. Their analyses showed that the mismatch between austenite and martensite elastic moduli causes toughening at the crack tip.

In a recent work, Baxevanis and Lagoudas [52] calculated J-integral, crack tip opening displacements (CTODs), and size of the martensite transformation region around the tip of a center-cracked infinite SMA plate under Mode I loading. To calculate SIF, they used Dugdale's [53] assumption, $K_{ext} + K_{int} = 0$, where $K_{ext} = \sigma_{\infty}\sqrt{\pi a_1}$, σ_{∞} is the remote stress and K_{int} is the SIF generated by internal stress distribution. They estimated the total inelastic strain as presented by Rice [54]

$$\varepsilon_{22}^{in} = \delta/b, \tag{1.1}$$

In Equation 1.1, ε_{22}^{in} is the inelastic strain (addition of plastic strain and transformation strain), δ is the COD, and b is the thickness of the plate. They formulated the internal stress distribution around the crack tip in terms of the extents of fully martensitic

region I_M, transformation I_T, and plastic region I_{pl}, using a power-law form of stress to define stress distribution in the fully martensite region $\sigma_m(x_1)$ defined as

$$\sigma_m(x_1) = M\frac{1}{(x_1 - a)^\rho} + N, \tag{1.2}$$

where

$$M = \frac{(I_{pl} + I_M)^\rho}{\left(\frac{I_{pl}+I_M}{I_{pl}}\right)^\rho - 1}\left(\sigma_Y - \sigma_T\right), \tag{1.3}$$

$$N = \frac{\sigma_T\left(\frac{I_{pl}+I_M}{I_{pl}}\right)^\rho - \sigma_Y}{\left(\frac{I_{pl}+I_M}{I_{pl}}\right)^\rho - 1}. \tag{1.4}$$

σ_T and σ_Y are transformation and yield stresses respectively. They obtained that when the stress level is above yield stress, phase transformation region size increases with increasing maximum transformation strain, and the existence of phase transformation decreases the size of the plastic zone. In a subsequent work, Baxevanis *et al.* [55] calculated the size and shape of the martensitic transformation region and J-integral near an edge-crack using the constitutive model of Lagoudas *et al.* [56]. Their numerical simulation shows that around the crack tip, J-integral is path dependent and the difference between J_{tip} and far field applied J (J_∞) is smaller than the difference obtained in elastic–plastic materials. Which is also shown in earlier work of Simsek [57], Alkan [58], Yurtoglu [59] and Altan [60].

In view of the above discussion, it is concluded that in recent years a substantial effort has been devoted to the study of fracture properties of SMAs. But to date there is no consensus about the effect of phase transformation on fracture of SMAs. Researchers proposed different methods to determine the phase transformation region around the crack tip, to calculate crack tip SIF and to determine the crack growth resistance in SMAs. Discussions arose on former studies and methodologies that are used. They are taken into consideration while defining the objectives of this dissertation in the following chapters.

1.3. Review of Constitutive Models of SMAs

The references presented so far provide the evidence that to study the shape memory and superelasticity effects, an accurate measure of transformation region is required. Therefore, a sound constitutive model has to be used. In this section, a brief summary of existing constitutive models that are used in former studies are given. Then, the constitutive model used in this study is presented in detail.

In literature, most of the constitutive models for SMAs are derived using either macro–scale or micro–scale approaches. Macroscale models are commonly established using energy considerations or phase diagrams.

The concept of free energy is first mentioned by Carnot [61]. later Herman von Helmholtz defined "free energy" as: $\Phi = U - Ts$, where U is the internal energy, and s is the entropy. Free energy represents the amount of energy "free" for work under the given thermodynamic state. In most continuum models, the thermodynamic forces related to state variables (temperature, stress and strain) and internal state variables (martensite fraction, orientation strain, etc.) are defined using either Helmholtz [62–75] or Gibbs [15, 16, 44, 56, 76–83] free energies. Gibbs free energy is used when the model is going to be validated by a stress controlled experiment, but if it is a strain controlled experiment Helmholtz free energy is used to derive the constitutive relations. Determining thermodynamic forces and how they relate to the state variables are the main objectives. In the thermodynamic framework for constitutive modeling, thermodynamic forces are obtained through partial derivatives of free energy functions with respect to corresponding state variables.

Similar to continuum models in micro-scale models the free energy function is obtained for the representative volume element (RVE) and integrated over whole material point. Since the shape memory effect is observed as a result of twinning of martensite, the very first attempts to define the constitutive behavior are related to the crystallographic theory of martensite [84]. Wechsler *et al.* [85] represented a phenomenological theory to define the crystallographic behavior of martensite and to explain the forma-

tion of martensite and the interface between austenite and martensite. It is difficult to identify material parameters in micro-models that depend on twinning kinetics. Energy wells and energy minimization theories are used to define the formation of martensite [86]. In addition to these methodologies, there are only a few work on modeling of SMAs [87–89] at atomistic level.

Researchers developed different constitutive models using different state variables, where the main concern was to describe the phase transition characteristics of SMA such as: martensite volume fraction, reorientation of martensite and the energy dissipation during phase change. In most of the continuum models, the evolution of state variables is governed by transformation functions analogous to yield surfaces in plasticity theory.

1-D models, derived from free energy theories, have been the starting point during the development of constitutive models [62–65, 90–95]. One such model is proposed by Falk and Konopka [96] where they used a polynomial free energy potential to define pseudo-elasticity and SME. Achenbach [97] used potential energy well theory to determine the phase transformation probabilistically. The empirical equation developed by Koistinen and Marburger [98] for pure iron-carbon alloys and plain carbon steels is used by earlier researchers to calculate the extent of the transformation region.

Patoor *et al.* [99] proposed a model for polycrystalline Cu-based shape memory alloys that exhibit dissymmetry between tension and compression. The model developed by Gall and Sehitoglu [100] was based on Patoor *et al.*'s model [101] and that was the first model to include texture measurements coupled with a micro-mechanical model to predict dissymmetry between tension and compression.

In the last decade, 3-D constitutive model development for SMAs that considers thermal behavior and uses free energy approaches have attracted much attention from researchers [2, 66, 77, 83, 96, 102–108, 108–112]. One such model is proposed by Boyd and Lagoudas [77] which uses the volume fraction of martensite as internal variable. In their constitutive model, they proposed a polynomial transformation function that

relates transformation strain to martensite fraction which is analogous to flow rule in plasticity. Auricchio *et al.* [3] and Lubliner and Auricchio [27] worked on isothermal pseudo-elasticity and introduced the Drucker-Prager-type transformation function [27]. Their finite elements results showed good agreement with experimental measurements. Tanaka and Iwasaki [113], Tanaka and Al. [114] and Tanaka and Nagaki [115] investigated pseudo-elasticity and shape memory effect from a thermomechanical point of view, and set up thermomechanical constitutive equations along with the phase transformation kinetics based on an exponential hardening rule. Liang and Rogers [70] developed a multi dimensional constitutive model for SMAs that is based on both micro and macro mechanics approaches and assuming a cosine type transformation function. As a case study they calculated the stress distribution in an SMA rod under torsion to show the applicability of their model multi-dimensionally.

To characterize the material properties and to implement a constitutive behavior into Abaqus, a user defined material subroutine (UMAT) is needed. In this study, the constitutive model of Zaki and Moumni [2] is implemented in Abaqus based on a return mapping algorithm. In stress intensity factor analysis, for comparison purposes the built-in Abaqus model following the Auricchio-Taylor-Lubliner constitutive model is used as well.

Zaki–Moumni (ZM) model is developed according to the concept of generalized standard materials with internal constraints [116–118]. In ZM model, thermomechanical coupling due to the latent heat generation during phase change is taken into account [119, 120]. Extension of ZM model to the cyclic SMA behavior is considered by Zaki and Moumni [121]. The development of the model is achieved by including tension—compression asymmetry [122] and improved by including plastic deformation of martensite [123]. A key limitation of most of the models in the literature is that they do not address the martensitic variant reorientation. In ZM model, together with martensite fraction orientation strain is taken as a state variable.

State variables are the quantities that characterize the state of the system, e.g. consider a gas in a cylinder, state variables are given by the pressure P, the volume

V and the temperature T, on the other hand, heat and mechanical work are not state functions and they are defined to express all the thermodynamic characteristic of the material [124]. State function only depends on the state of the system and not on the manner in which this state is achieved. In vast majority of constitutive models summarized so far, the common idea is to use martensite volume fraction as the main internal state variable. The common idea of these models is to choose austenite as the parent phase and martensite is defined as product phase.

In ZM model the Helmholtz free energy is used as a thermodynamic potential and it is formulated as:

$$\begin{aligned}\Psi(\varepsilon_{ij}^{A}, \varepsilon_{ij}^{M}, T, \zeta, \varepsilon_{ij}^{ori}) = (1-\zeta)\left[\frac{1}{2}\varepsilon_{ij}^{A} E_{ijkl}^{A} \varepsilon_{kl}^{A}\right] \\ + \zeta\left[\frac{1}{2}\left(\varepsilon_{ij}^{M} - \varepsilon_{ij}^{ori}\right) E_{ijkl}^{M}\left(\varepsilon_{kl}^{M} - \varepsilon_{kl}^{ori}\right) + C(T)\right] \\ + \Gamma\frac{\zeta^2}{2} + \frac{\zeta}{2}\left[\alpha\zeta + \beta(1-\zeta)\right]\frac{2}{3}\varepsilon_{ij}^{ori}\varepsilon_{ij}^{ori}. \end{aligned} \tag{1.5}$$

In the equation above T, ζ and ε_{ij}^{ori} represent respectively temperature, martensite volume fraction, and orientation strain–tensor. ε_{ij}^{M} and ε_{ij}^{A} are local strain tensors of martensite and austenite phases. β controls the level of orientation of martensite variants created during forward phase change, Γ is responsible for orientation-independent interaction between martensite variants, the term starting with α is analogous to the linear kinematic hardening of a elasto–plastic material and controls the slope of the stress strain curve corresponding to martensite orientation. E_{ijkl}^{M} and E_{ijkl}^{A} are the elasticity tensors of martensite and austenite phases respectively. $C(T)$ is phase change heat density as shown below:

$$C(T) = \xi(T - A_f) + \kappa, \tag{1.6}$$

where ξ and κ are material parameters and A_f is the austenite finish temperature under

zero stress. ξ is written as follows:

$$\xi = \frac{\partial \Psi}{\partial T \partial \zeta}. \tag{1.7}$$

The details of these parameters and identification methods are represented in Zaki and Moumni [2].

The physical constraints on the state variables are accounted for by the ZM model using the theory of Lagrange multipliers. Reuss scheme is used to relate the total strain ε_{ij} in an RVE to the local strains in austenite and martensite as below:

$$\varepsilon_{ij} = (1-\zeta)\varepsilon_{ij}^{A} + \zeta\varepsilon_{ij}^{M}, \tag{1.8}$$

the internal state variable ζ should be bounded in the interval $[0, 1]$, therefore:

$$\zeta \geqslant 0 \quad \text{and} \quad (1-\zeta) \geqslant 0, \tag{1.9}$$

and the equivalent orientation strain has a maximum value ε_0

$$\varepsilon_{ori}^{0} - \sqrt{\frac{2}{3}\varepsilon_{ij}^{ori}\varepsilon_{ij}^{ori}} \geqslant 0. \tag{1.10}$$

As it is explained in Zaki and Moumni [2] the constraints defined in Equations 1.8, 1.9 and 1.10 are used to build the following constrains potential Ψ_c [117]:

$$\Psi_c = -\lambda_{ij}[(1-\zeta)\varepsilon_{ij}^{A} + \zeta\varepsilon_{ij}^{M} - \varepsilon_{ij}] - \left(\varepsilon_{ori}^{0} - \sqrt{\frac{2}{3}\varepsilon_{ij}^{ori}\varepsilon_{ij}^{ori}}\right) - \nu_1\zeta - \nu_2(1-z). \tag{1.11}$$

Where the Lagrange multipliers λ, μ, ν_1, ν_2 and μ obey the following conditions:

$$\nu_1 \geqslant 0, \quad \nu_1\zeta = 0, \quad \nu_2 \geqslant 0, \quad \nu_2(1-z) = 0 \quad \text{and} \quad \mu \geqslant 0, \mu\left(\varepsilon^0 - \sqrt{\frac{2}{3}\varepsilon_{ori}\varepsilon_{ori}}\right) = 0. \tag{1.12}$$

The Lagrangian is obtained as the sum of the two potentials defined in Equations 1.5 and 1.11 to derive state equations:

$$\begin{aligned}\mathcal{L} = &(1-\zeta)\left[\frac{1}{2}\varepsilon_{ij}^A E_{ijkl}^A \varepsilon_{kl}^A\right] + \zeta\left[\frac{1}{2}\left(\varepsilon_{ij}^M - \varepsilon_{ij}^{ori}\right)E_{ijkl}^M\left(\varepsilon_{kl}^M - \varepsilon_{kl}^{ori}\right) + C(T)\right] \\ &+ \Gamma\frac{\zeta^2}{2} + \frac{\zeta}{2}\left[\alpha\zeta + \beta(1-\zeta)\right]\frac{2}{3}\varepsilon_{ij}^{ori}\varepsilon_{ij}^{ori} \\ &- \lambda_{ij}[(1-\zeta)\varepsilon_{ij}^A + \zeta\varepsilon_{ij}^M - \varepsilon_{ij}] - \left(\varepsilon_{ori}^0 - \sqrt{\frac{2}{3}\varepsilon_{ij}^{ori}\varepsilon_{ij}^{ori}}\right) - \nu_1\zeta - \nu_2(1-z).\end{aligned} \tag{1.13}$$

A_z and A_{tr} being the only non-zero thermodynamic forces, the following state equations are derived from the Lagrangian (Equation 1.13):

$$\mathcal{L}_{,\varepsilon_{ij}} = \sigma_{ij} \quad \Rightarrow \quad \lambda_{ij} - \sigma_{ij} = 0, \tag{1.14}$$

$$-\mathcal{L}_{,\varepsilon_{ij}^A} = 0 \quad \Rightarrow \quad (1-\zeta)[\varepsilon_{kl}^A E_{ijkl}^A - \lambda_{ij}] = 0, \tag{1.15}$$

$$-\mathcal{L}_{,\varepsilon_{ij}^M} = 0 \quad \Rightarrow \quad \zeta[E_{ijkl}^M(\varepsilon_{kl}^M - \varepsilon_{kl}^{ori}) - \lambda_{ij}] = 0, \tag{1.16}$$

$$\begin{aligned}-\mathcal{L}_{,\zeta} = A_\zeta \quad \Rightarrow \quad A_\zeta = &\frac{1}{2}[\varepsilon_{ij}^A E_{ijkl}^A \varepsilon_{kl} - (\varepsilon_{kl}^M - \varepsilon_{kl}^{ori})E_{ijkl}^M(\varepsilon_{ij}^M - \varepsilon_{ij}^{ori})] \\ &- C(T) - \Gamma\zeta - \left[(\alpha-\beta)\zeta + \frac{\beta}{2}\right]\left(\frac{2}{3}\varepsilon_{ij}^{ori}\varepsilon_{ij}^{ori}\right) \\ &- \lambda_{ij}(\varepsilon_{ij}^A - \varepsilon_{ij}^M),\end{aligned} \tag{1.17}$$

$$\begin{aligned}\mathcal{L}_{,\varepsilon_{ij}^{ori}} = A_{\text{ori}} \quad \Rightarrow \quad A_{\text{ori}} = &\zeta\left[E_{ijkl}^M(\varepsilon_{kl}^M - \varepsilon_{kl}^{ori}) - \frac{2}{3}[\alpha\zeta + \beta(1-\zeta)\varepsilon_{ij}^{ori}]\right] \\ &- \frac{2\mu}{3}\frac{\varepsilon_{ij}^{ori}}{\sqrt{\frac{2}{3}\varepsilon_{ij}^{ori}\varepsilon_{ij}^{ori}}},\end{aligned} \tag{1.18}$$

$$-\mathcal{L}_{,\lambda_{ij}} = 0 \quad \Rightarrow \quad (1-\zeta)\varepsilon_{ij}^A + \zeta\varepsilon_{ij}^M - \varepsilon_{ij} = 0. \tag{1.19}$$

The state equations written above (Equations 1.14, 1.15, 1.16, 1.17, 1.18, and 1.19) yields the following stress–strain relation:

$$\sigma_{ij} = S^{-1}_{ijkl} : \left(\varepsilon_{kl} - \zeta \varepsilon^{ori}_{kl}\right), \tag{1.20}$$

in which S_{ijkl} is the compliance tensor defined as:

$$S_{ijkl} = (1-\zeta) S^{A}_{ijkl} + \zeta S^{M}_{ijkl}, \tag{1.21}$$

where S^{A}_{ijkl} and S^{M}_{ijkl} are the compliance tensors of austenite and martensite phases respectively.

According to the theory of generalized standard materials with internal constraints represented by Halphen and Nguyen [116] the thermodynamic forces that are related to the internal state variables ζ and ε^{ori}_{ij} are sub-gradients of a pseudo-potential. The pseudo-potential of dissipation defined by Zaki and Moumni [2] is given as follows:

$$D(\dot{\zeta}, \dot{\varepsilon}^{ori}_{ij}) = [a(1-\zeta) + b\zeta]|\dot{\zeta}| + \zeta^2 Y \sqrt{\frac{2}{3} \dot{\varepsilon}^{ori}_{ij} \dot{\varepsilon}^{ori}_{ij}}. \tag{1.22}$$

According to the definition, the constants a, b and Y are positive and material specific constants. As it is stated by Halphen and Nguyen [116], dissipation function should be non-negative, convex with respect to the fluxes of dissipative variables, lower semi-continuous and equal to zero when the fluxes are zero. According to the definition A_z is the sub–gradient of the convex function D, $A_z \in \partial_{\dot{z}} D$, $A_{ori} \in \partial_{\dot{\varepsilon}^{ori}_{ij}} D$. In other inequality form:

$$D(\zeta, \dot{\zeta}, \dot{\varepsilon}^{ori}_{ij}) - D(\zeta, 0, \dot{\varepsilon}^{ori}_{ij}) \geq A_{\zeta}(\dot{\zeta} - 0), \tag{1.23}$$

$$D(\zeta, \dot{\zeta}, \dot{\varepsilon}^{ori}_{ij}) - D(\zeta, \dot{\zeta}, 0) \geq A_{ori}(\dot{\varepsilon}^{ori}_{ij} - 0). \tag{1.24}$$

it follows from Equations 1.22 and 1.24 that the forward transformation function ($\dot{\zeta} \geq$

0),

$$F_\zeta^f = E'\frac{\sigma_e^2}{3} + \frac{1}{2}\left(\frac{1}{3}E' + \nu'\right)\sigma_{ii}^2 - C(T) + \sigma_{ij}\varepsilon_{ij}^{ori}$$
$$-(\Gamma + b)\zeta - a(1-\zeta) - \left[(\alpha-\beta)\zeta + \frac{\beta}{2}\right]\left(\frac{2}{3}\varepsilon_{ij}^{ori}\varepsilon_{ij}^{ori}\right) \leq 0, \tag{1.25}$$

and reverse transformation function ($\dot{\zeta} \leq 0$) is equal to:

$$F_\zeta^r = -E'\frac{\sigma_e^2}{3} - \frac{1}{2}\left(\frac{1}{3}E' + \nu'\right)\sigma_{ii}^2 + C(T) - \sigma_{ij}\varepsilon_{ij}^{ori}$$
$$+(\Gamma - b)\zeta - a(1-\zeta) + \left[(\alpha-\beta)\zeta + \frac{\beta}{2}\right]\left(\frac{2}{3}\varepsilon_{ij}^{ori}\varepsilon_{ij}^{ori}\right) \leq 0, \tag{1.26}$$

where σ_e is the von Mises stress, $\sigma_e = \sqrt{\frac{3}{2}\sigma_{ij}^d\sigma_{ij}^d}$, σ_{ij} is the Cauchy stress tensor, and σ_{ij}^d is the deviatoric part of σ_{ij}. $E^{'}$ and $\nu^{'}$ are given below:

$$E' = \frac{(1+\nu)(E_A - E_M)}{E_A E_M} \quad , \quad \nu' = \frac{\nu(E_M - E_A)}{E_M E_A}, \tag{1.27}$$

where E_M and E_A are the elastic moduli of austenite and martensite; ν is Poisson's ratio of the material ($\nu_A = \nu_M = \nu$). a and b are defined as:

$$a = \frac{1}{2}\left[\left(\frac{1}{E_M} - \frac{1}{E_A}\right)\frac{\sigma_{Ms}^2 - \sigma_{Af}^2}{2} + (\sigma_{Ms} - \sigma_{Af})\varepsilon_0^{ori}\right], \tag{1.28}$$

$$b = \frac{1}{2}\left[\left(\frac{1}{E_M} - \frac{1}{E_A}\right)\frac{\sigma_{Mf}^2 - \sigma_{As}^2}{2} + (\sigma_{Mf} - \sigma_{As})\varepsilon_0^{ori}\right], \tag{1.29}$$

where σ_{Ms}, σ_{Mf}, σ_{As} and σ_{Af} are martensite start, martensite finish, austenite start and austenite finish stresses respectively. In the case of forward transformation, terms a and b define the stresses at the beginning and end of the martensite transformation. ε_0^{ori} is the equivalent transformation strain that can be obtained from uniaxial tensile experiment (see Figure 1.3).

In ZM model the forward phase transformation (from austenite to martensite)

occurs when the transformation function F_ζ [2] is equal to zero. In proportional loading, it is assumed that the martensite variants are already oriented. In other words at the corresponding temperature orientation finish stress is lower than the critical stress for forward phase change and therefore austenite crystals are transformed into single variant martensite that are oriented parallel to loading direction. By assuming that the material is already oriented, the direction of orientation strain is parallel to the stress deviator since the Lagrange multiplier μ is zero [2].

In SMAs, an equivalent transformation strain, ε_0^{ori} can be defined as:

$$\sqrt{\frac{2}{3}\varepsilon_{ij}^{ori}\varepsilon_{ij}^{ori}} = \varepsilon_0^{ori}, \tag{1.30}$$

ε_{ori} can be calculated as follows, [125]:

$$\varepsilon_{ij}^{ori} = \frac{3}{2}\varepsilon_0^{ori}\frac{S_{ij}}{\sigma_e} \quad \text{when} \quad \sigma_e \neq 0. \tag{1.31}$$

1.4. Industrial Applications of Shape Memory Alloys

The discovery of SMAs having high transformation temperatures (e.g. TiPd, TiPt and TiAu), improved fatigue life and damping behavior [126], high strain recovery and corrosion resistance (e.g. NiTi and NiTiCu), and ferromagnetic characteristics (e.g. Ni–Mn–Ga) widened the use of these materials in the various fields of industry. Their remarkable properties make them attractive for engineers, scientists, and designers who have been attempting to utilize them in the applications where the smart material behavior is required.

In the early years of their discovery, SMAs are mostly used in aerospace and medical applications. One of the first industrial applications was pipe coupling in military aircraft [127]. In aerospace industry, SMAs are generally used where there is a need for dynamic property optimization of aircraft structural panels. This optimisation is accomplished through changing elastic stiffness via phase transformation. In addition,

active flexible smart wings and solar panels are designed using SMAs as well. Coupling devices and fasteners are one of the most common industrial applications that use shape memory properties SMAs. SME is used for example in pipe fitting: the expanded coupling is shrunk by cooling for easy insertion at the joint location in the pipe assembly. As it heats to service temperature, the SMA coupling expands and joins the pipes.

Among all the medical applications that SMAs are used for, including self-expanding Nitinol stents, implant material in orthopedics, active endoscope heads [128], guide wires, root canal surgery drills, aterial septal occlusion devices, artificial bone implants, spinal vertebrae spacers, steerable catheters, blood filters, Nitinol is more commonly used in orthodontic braces. Unlike more conventional metals, retensioning is not needed for Nitinol wires that are used as dental braces. The ability of superelastic NiTi to deform in large amounts without any plastic deformation is a great potential for them to be utilized in critical medical applications. The self-expanding stents are used for revascularization of occluded blood vessels, they are manufactured slightly larger than the vessel, compressed and placed inside a tube, then released in the vessel at the problematic site. NiTi stents expand over twice of their compressed diameter. After their self expansion they apply a low outward force to the wall of the vessel. Moreover, NiTi stents are corrosion resistant and biocompatible.

In advanced industry, SMAs are utilized in areas such as energy production, electronic devices, automotive engineering, safety products design, and robotics. Their popularity is growing nowadays especially due to the improvements in mobile and wearable technologies. In the last few years, there has been a growing interest in their usage in civil structures. The unique properties of SMAs enable them to be used as actuators, passive energy dissipators and dampers to control civil structures [129]. In civil engineering, they are used in the design of seismic protection devices [130]. Besides their usage in critical applications, they are also used in everyday products such as eyeglass frames, golf clubs, rice cookers, safety devices and sensors, mobile phone parts, automobile parts, coffee machines and headphones [131]. To improve the service life of parts made of SMAs, it is required to optimize their material parameters.

The importance of optimization of their material parameters is increasing in parallel to the spread of their use in different fields of the industry.

Due to their superior characteristics, the application field of SMAs are growing very rapidly in areas where the there is a need of large elastic deformations, high temperature changes and combination of thermomechanical and magnetic forces. Therefore many researches are interested in analyzing the fatigue and fracture behavior of SMAs

1.5. Research Objectives

SMAs are used in safety-critical applications, promoting the need for better understanding of their failure mechanism. Despite significant advancement in experimental, analytical and numerical techniques used in characterizing and simulating the behavior of SMAs, there are several issues on fracture properties to be clarified. One question still unanswered is whether the phase transformation increases toughness of SMAs or not. Majority of the researchers saying that phase transformation increases toughness of SMAs and reduces crack tip SIF, on the contrary some researches claims that SIF decreases due to negative volume change during phase transformation Besides that, still the fracture parameters measured experimentally are not correlated adequately with the analytical and numerical models to show clearly the effect of phase transformation on fracture parameters of superelastic SMAs.

To investigate the fracture of SMAs, the questions listed above, which outline the research objectives of this thesis, are discussed in a certain order to ensure the integrity of this study.

(i) How to determine the transformation region around the crack tip in SMA in agreement with the experimental measurements available in the literature?
(ii) What is the effect of phase transformation on toughness? How to calculate SIF and other fracture mechanics parameters of SMAs accurately?
(iii) What is the effect of phase transformation and orientation of martensite during steady-state crack growth? How to evaluate phase transformation region using

stationary movement method?

(iv) What is the effect of the thermomechanical coupling which is due to the latent heat release in an SMA plate under Mode III loading?

1.6. Outline of the Thesis

In the introduction chapter, a detailed literature survey about the studies on fracture mechanics parameters and fracture toughness of SMAs are summarized in a chronological order. The reasons behind the necessity to investigate the fracture mechanics parameters of SMAs are discussed. The main problem statements that underlines the objective of this dissertation are represented. The remainder of the thesis is organized in four main chapters.

In Chapter II, the size of the martensitic region surrounding the tip of an edge-crack in a SMA plate is calculated analytically using the transformation function proposed by [2] together with crack tip asymptotic stress equations. The transformation region is also calculated with FE by implementing ZM model in Abaqus through UMAT. Transformation regions calculated analytically and computationally are compared to experimental results available in the literature [35].

The next chapter is devoted to evaluation of fracture parameters like SIFs, J-integrals, energy release rates, CTODs and T-stresses. The objective is to understand the effect of phase transformation on fracture behavior of an edge-cracked Nitinol plate under Mode I loading. In the FE analysis of the edge-cracked plate under mode I loading, Abaqus is used with both ZM model, written through UMAT and built-in SMA model based on Auricchio's model. J-integrals are found to be contour dependent as a result of non-homogeneity around crack tip, therefore SIFs are directly calculated from strain energy release rate and compared to the SIFs calculated using asymptotic near-tip opening displacement field equation.

In Chapter IV, steady-state crack growth in an SMA plate is analyzed. In this chapter, Mode I steady-state crack growth in an edge-cracked Nitinol plate is modeled

using a non-local stationary method. The model is implemented in Abaqus using ZM model by means of UMAT to determine transformation zones around the crack tip. steady-state crack growth is first simulated without considering reverse transformation to calculate the effect of transformation on stress distribution in the wake region, then reverse transformation is taken into account. The effect of reorientation of martensite near the crack tip as a result of non-proportional loading is also studied. The stress distribution and the phase transformation region are compared to results obtained for the case of a static crack.

Chapter V, concerns the calculation of the phase transformation region analytically around the tip of an SMA specimen under Mode III loading; at first the analytical method represented by Moumni [117] in which the material model is built based on the framework of standard materials with internal constraints [132, 133], is revisited. Using the hodograph method, the non-linear PDE problem is transformed to a linear boundary value problem in hodograph plane and phase transformation around the tip of a crack under Mode III loading is calculated analytically. In this chapter, the thermomechanical coupling is added to the solution of the Mode III problem proposed by Moumni [117]. As a result of the analysis, fully coupled phase transformation region and the temperature increase due to the latent heat generation is calculated numerically around the crack tip. Finally, the last chapter summarizes the results of this work from a more general perspective and draws a detailed conclusion on the results obtained.

2. EVALUATION OF TRANSFORMATION REGION AROUND CRACK TIP IN SHAPE MEMORY ALLOYS

A crack in a NiTi plate acts as a stress raiser and leads to phase transformation from austenite to martensite around crack tip from the very beginning of loading and it gets larger as the load increases. In this chapter, the size of the martensitic region surrounding the tip of an edge-crack in a SMA plate is calculated analytically using a transformation function that governs forward phase transformation together with crack tip asymptotic stress equations. The transformation region is also calculated with finite elements using user defined constitutive models. Transformation regions calculated analytically and computationally are compared to experimental results available in the literature.

2.1. Introduction

In a solid having a crack, the modes of fracture are classified as: opening mode (Mode I), inplane sliding mode (Mode II), and anti-plane sliding mode (Mode III). In Mode I, crack opens by a normal tensile stress perpendicular to the crack plane. In Mode II inplane shear normal to the crack front and in Mode III anti-plane shear parallel to the crack are applied. In plane stress, the stress field around the tip of a linear elastic isotropic material can be calculated using the formulation:

$$\sigma_{ij} = \frac{K}{\sqrt{2\pi r}} f_{ij}(\theta) \tag{2.1}$$

For elastic-plastic materials the size of the crack plastic region is estimated using different approaches. Irwin's method and Dugdale [53] and Barenblatt's [135] strip yield model are two commonly used approaches. According to Irwin, stresses calculated using asymptotic equations should be redistributed around the crack tip to satisfy the equilibrium conditions, therefore the plastic zone size must increase. In Irwin's method

the extent of plastic region is calculated using:

$$r_p = \frac{1}{\pi}\left(\frac{K}{\sigma_y}\right)^2 \tag{2.2}$$

where r_p is the extent of the plastic region, K is the stress intensity factor and σ_y is the yield stress. The strip yield model assumes that the plastic region zone concentrates in a strip starting from the tip. In this model the superposition of the stresses due to applied load and crack closure stresses are used to approximate the extent of plastic region. According to strip yield model in plane stress, r_p can be calculated using:

$$r_p = \frac{\pi}{8}\left(\frac{K}{\sigma_y}\right)^2 \tag{2.3}$$

Most of the studies in the literature used these two approaches to estimate the extent of phase transformation region around the crack tip.

In previous work to investigate the effect of the crack in an edge-cracked Nitinol plate, FE analysis is used and a few experiments are performed. In recent years, although studies on the extent of martensite region around crack tip have been presented, accurate comparisons to experimental results are limited. In the following section the previous work on evaluation of transformation region around crack tip is summarized.

Bulbich [136] determined the nucleation of stress-induced phase transformation at the crack tip analytically using phase diagram approach and he stated that nucleation is only possible for slowly propagating cracks. Birman [18] is the first to calculate the phase transformation region around a center-crack in a SMA plate as a function of external loading using martensite fraction equation of Tanaka and Sato [40];

$$\zeta = 1 - \exp\left[b_M\left(M_S^0 - T\right) + \left(b_M/d_M\right)\sigma_{eff}\right], \tag{2.4}$$

where b_M is a material constant defined as:

$$b_M = \frac{\ln 0.01}{(M_s^0 - M_f^0)} \quad . \tag{2.5}$$

M_s^0 and M_f^0 are martensite start and finish temperatures at zero stress, d_m is the slope of the stress-temperature curves, $\sigma_{crit}^{SIM} = d_m(T - M_s^0)$, and σ_{eff} is the von Mises stress. He used crack tip asymptotic stress equations together with Equation 2.4 to calculate the extent of transformation region as given below:

$$r_M = K_I^2 / \left\{ 2\pi d_M^2 \left(\ln 0.01 / b_M + T - M_S^0 \right)^2 \right\}, \tag{2.6}$$

$$r_A = K_I^2 / \left\{ 2\pi \left[d_M \left(T - M_S^0 \right) \right]^2 \right\}. \tag{2.7}$$

Xiong and Liu [39] extended the work of Birman [18] by considering stress redistribution as a result of phase transformation using Irwin's plasticity corrected formula, and calculated the extend of transformation region analytically. They obtained the following equations to calculate fully martensite region as:

$$r_m = \frac{1}{2} \left(\frac{\sigma_y}{\sigma_{crit}^{SIM}} \right)^2 \left(\frac{T - M_s^0}{T - M_f^0} \right)^2 r_p + \frac{1}{2} r_p, \tag{2.8}$$

and for transformation region they found:

$$r_{tr} = \frac{1}{2} \left(\frac{1}{\sigma_{crit}^{SIM}} + \frac{1}{\sigma_y^2} \right) \sigma_0^2 a \tag{2.9}$$

therefore the size of the transformation region when the fully martensitic region is subtracted can be written as:

$$r_{tr} - r_m = \frac{1}{2} \frac{\sigma_0^2}{d_m^2} \left\{ \frac{1}{(T - M_s^0)^2} - \frac{1}{(T - M_f^0)^2} \right\} a, \tag{2.10}$$

where a is the crack length and σ_0 is the external tensile stress. Using a similar ap-

proach, Yi and Gao [22] used a phase transformation function given by Sun and Hwang [15, 16], which they called yield condition of SMAs, to calculate transformation region around the tip of an edge-crack. They derived the following equation to determine phase transformation boundaries:

$$\sqrt{r\left(\theta\right)} = \frac{1}{\sqrt{2\pi}} \left[\frac{K}{\sigma_e^c\left(T,\zeta\right)}\right] \cos\frac{\theta}{2}\left(1+3\sin^2\frac{\theta}{2}\right)^{\frac{1}{2}}, \tag{2.11}$$

where g is the equivalent transformation strain, and $\sigma_e^c\left(T,\zeta\right)$ is defined as:

$$\sigma_e^c\left(T,\zeta\right) = \frac{\sqrt{3}}{g}\left[\left(a+b\zeta\right)\left(T-M_S\right)\right]. \tag{2.12}$$

According to their results the shape of phase transformation start ($\zeta = 0^+$) and fully martensite region ($\zeta = 1$) are similar with different radii.

Lexcellent and Blanc [45] presented a yield criterion for Nitinol as:

$$g(\sigma_{ij}) = \sigma_{vm}\left(\cos\left(\frac{\arccos\left(1-a\left(1-y\right)\right)}{3}\right)\right) - \sigma_0 \tag{2.13}$$

where y is $y = \frac{27}{2}\frac{\det\left(\sigma^d\right)}{\left(\sigma_{VM}\right)^3}$, a is a lattice parameter, r is ratio of the average stress of each grain, σ_0, over average transformation stress. They calculated analytically the extent of phase transformation zone using the yield function given in Equation 2.13; which, however turned out to give a zone roughly six times larger according to a later study by Robertson *et al.* [35].

Wang *et al.* [137] used FE to investigate stress-induced martensite transformation near the crack tip of a CT NiTi specimen. They found out that fully martensite region size enlarges and extent of transformation region increases when the tip is transforming from a mild notch to a sharp crack. They concluded that the shape of the transformation region in front of the crack tip is similar to the plastic region around the crack tip of an elastic–plastic material. Wang [29] defined NiTi as an elastic-plastic material, used uniaxial tensile stress-strain data in Abaqus to determine phase transformation

and plastically deformed region boundaries under Mode I loading. To find the martensite volume fraction contours, they used a simple relation, $\zeta = K\epsilon_{peq}$, where K is a proportionality constant between 1 and 27.4, and ϵ_{peq} is between 0 and 0.0365. The results of their study showed that with increasing notch acuity from blunt to acute notch, the sizes of the "fracture process zone" decrease, and the crack propagation changes from unstable to stable state.

Freed and Banks-Sills [41] used the transformation surface equation proposed by Panoskaltsis *et al.* [42], which was like a von Mises type surface, given as $F_{A_f}(\sigma, T) = \sqrt{3J_2} - C_A\,(T - A_f)$, where σ is the Cauchy stress tensor, J_2 is the second invariant of the stress deviator tensor and C_A is a material property. Using the transformation function and crack tip asymptotic stress equations they calculated the transformation region around crack tip of an edge-crack under Mode I loading. They concluded that shape of the region that they obtained under Mode I loading resembles to the shape of the plastic zone in plastically deformed materials, where the size of the transformation regions are governed by a thermally dependent variable like in plasticity.

Robertson *et al.* [35] used X-ray diffraction to obtain local strain maps around the crack tip of an edge-cracked thin Nitinol specimen. They reported a detailed strain map showing transformed martensite regions and concluded that the transformation zone shape was consistent with the shape predicted by LEFM.

Daly *et al.* [36] used DIC on an edge-cracked thin sheet of NiTi under Mode I loading to obtain strain field around crack tip. They determined the extent of the transformation along a line ahead of crack tip. Using ϵ_{22}, they obtained an empirical expression between the extent of transformation region and the applied load. Using the same approach [138] found an empirical relation between loading parameters and the extent of phase transformation zones as, $r_{trans} = 0.136\frac{K_I^2}{2\pi\sigma_0^2}$. Daly [138] used Abaqus to calculate the phase transformation region around the crack tip under Mode I loading. She studied the effect of material properties like plateau stress and transformation strain on phase transformation size. Her results showed that when the plateau stresses increases the extent of region increases but the fully martensite region becomes rela-

tively smaller, and if the transformation strain increases the same trend is observed.

Gollerthan *et al.* [37] conducted experiments on a CT specimen under Mode I loading and observed the deformed region around the crack tip. They adopted the formulation proposed by Irwin to estimate the length of the phase transformation region ahead of crack under Mode I loading. They claimed that phase transformation length they calculated is in agreement qualitatively with their experimental observation, although this claim was difficult to follow. In a latter study, Gollerthan *et al.* [50] obtained phase transformation zone around the crack tip of an edge-cracked NiTi specimen using in-situ synchrotron measurements. They observed stress-induced martensite (up to a volume fraction of 0.4) around the tip with a small plastic region.

Lexcellent and Thiebaud [43] used the yield criterion of Lexcellent and Blanc [45] together with asymptotic crack tip stress equations to determine the transformation region around the crack tip under Mode I loading for both plane stress and plane strain. They determined the shape of the martensite region using the following function:

$$r_f = \frac{1}{4\pi}\left[\frac{K_I}{b\left(T - M_f^0\right)}\right]^2 R(\theta) f^2\left(y_\sigma\left(\theta\right)\right) \tag{2.14}$$

where $R(\theta)$ and $y_\sigma(\theta)$ are:

$$R(\theta) = \beta^2\left(1 + \cos\theta\right) + \frac{3}{2}\sin^2\theta, \tag{2.15}$$

$$y_\sigma(\theta) = 2\sqrt{2}\beta\cos^3\frac{\theta}{2}\frac{\left(9\sin^2\frac{\theta}{2} - \beta^2\right)}{\left(\beta^2\left(1 + \cos\theta\right) + \frac{3}{2}\sin^2\theta\right)^{\frac{3}{2}}}. \tag{2.16}$$

In the equations above Equations 2.15 and Equation 2.16 $\beta = 1$ for plane stress and $\beta = (1 - 2\mu)$ for plane strain. $y_\sigma(\theta) \in [-1, 1]$ when $0 < \theta < 2\pi$. Their results show a considerable difference with the experimental results of Robertson *et al.* [35]. In a following study Lexcellent *et al.* [139] extended the study of Lexcellent and Thiebaud [43] and determined the transformation region around the crack tip under Mode II,

Mode III and mixed-Mode following a similar formulation. Taillebot, Lexcellent, and Vacher [140] predicted the size of the transformation region around the crack tip of an edge-cracked NiTi specimen using strain field obtained from DIC. Their experimental results showed that, the height of the transformation region is almost one third of the height they calculated using the formulation given by Lexcellent *et al.* [139].

Falvo *et al.* [46] used both $\sigma_y = K_I/\sqrt{2\pi r}$ and $\sigma_y = K_{Ieff}/\sqrt{2\pi(r-r_y)}$ to predict the extent of transformation line along crack in a NiTi-based SMA under plane stress. They compared their prediction to results they obtained using MARC and showed that improved results are obtained when Irwin's plasticity corrected formula is used. In a very similar way to their previous work [46], Maletta and Furgiuele [48] used bilinear stress-strain relation together with Irwin's plasticity corrected equation to calculate the extent of martensitic region. The limitation of this model is assuming a constant stress during transformation. The equations they used to calculate the extent of martensite and austenite regions are given above (see Equations 2.17 and 2.18).

$$r_A = 2r^* - \frac{1}{\pi}\left(\frac{K_I}{\sigma_0^{tr} + b_M\left(T - T_0\right)}\right)^2 \frac{2(1-\nu)^2}{\left(2\left(1-\nu\right) + \left(\alpha^{-1} - 1\right)\right)\left(2\left(1-\nu\right) + \frac{\epsilon_L E_A}{(\sigma_o^{tr} + b_M(T-T_0))}\right)}, \tag{2.17}$$

$$r_M = \frac{1}{2\pi}\left(\frac{2\left(1-\nu\right)K_I}{2\left(1-\nu\right)\left(\sigma_o^{tr} + b_M\left(T-T_0\right)\right) + \epsilon_L E_A)}\right)^2 \tag{2.18}$$

where r^* is the extent of the region obtained from asymptotic near-tip stress equation, σ_0^{tr} is plateau stress, b_M is a material constant. They showed that their analytical calculations are in agreement with FE results (MSC MARC). Maletta and Young [49] extended the model of Maletta and Furgiuele [48], which was limited to plane stress to determine the length of the phase transformation region along the crack line under plane strain. The region they calculated for plane strain was smaller than that of plane stress. They compared their results to experimental results of Gollerthan *et al.* [50] and observed that experimentally calculated phase transformation length was between the length they calculated for plane stress and the one for plane strain.

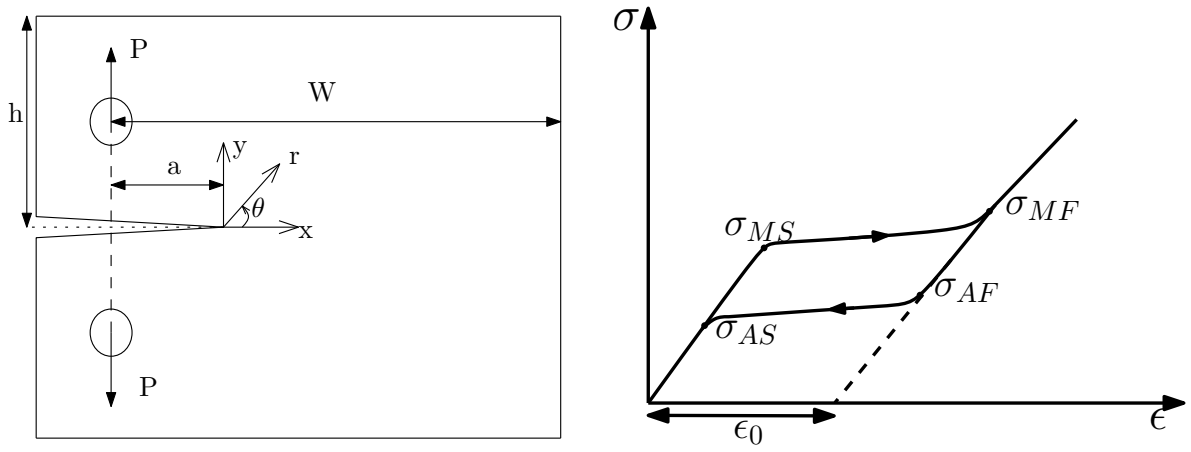
Baxevanis *et al.* [55] implemented the constitutive model of Lagoudas *et al.* [56] into Abaqus to determine the size and the shape of the phase transformation region. They normalized the length parameters using $R_\xi = \frac{1}{3\pi}\frac{K_I^2+\frac{25}{4}K_{II}^2}{(\sigma_{Ms})^2}$. They also estimated the size of the transformation region modifying Irwin's formulation for Mode II [141], compared the two set of results and claimed that the formulation could be used to approximate the transformation zone. Their results showed that the effect of transformation hardening on the transformation region shape is similar to the effect of the hardening on the shape of the plastic region [142], and when the temperature increases, transformation zone size decreases.

Using a NiTi specimen under mode I loading, Young *et al.* [143] measured strain field using synchrotron X-ray diffraction and determined phase transformation region around crack tip under Mode I loading as was done previously by Gollerthan *et al.* [50]. They stated that the extent of the transformation zone calculated using equations presented by Gollerthan *et al.* [37] was in agreement with the result of their experiments.

As summarized above, although there are attempts on calculations and measurements of transformation regions around crack tip, accurate and simple calculations that compare well with experiments are lacking. In this paper, the boundary of martensitic region around a crack tip is calculated analytically using the transformation function proposed by Zaki and Moumni [2] together with asymptotic stress equations and also using finite elements. Then the analytical and computational results obtained are compared to experimental results presented by Robertson *et al.* [35].

2.2. Problem Statement and Formulation

The geometry of the edge-cracked thin SMA plate used in this study is shown in Figure 2.1a. The plate is loaded in y direction and a superelastic phase transformation occurs around the crack tip. Forward phase transformation is governed by the following transformation function, F_ζ:



a b

Figure 2.1. (a) Edge cracked SMA CT specimen $B = 0.4$ mm (thickness), $W = 10.8$ mm, $a = 5.4$ mm, $h = 6.4$ mm. (b) Uniaxial stress-strain behavior of superelastic Nitinol.

$$F_\zeta = \left\{ E' \frac{\sigma_e^2}{3} + \frac{1}{2}\left(\frac{1}{3}E' + \nu'\right)\sigma_{ii}^2 - C(T) \right\} + \sigma_{ij}\varepsilon_{ij}^{ori} - (\Gamma + b)\zeta - a(1-\zeta) - \left[(\alpha - \beta)\zeta + \frac{\beta}{2}\right]\left(\frac{2}{3}\varepsilon_{ij}^{ori}\varepsilon_{ij}^{ori}\right), \tag{2.19}$$

when $F_\zeta = 0$, transformation from austenite to martensite occurs. In Equation 2.19 σ_e is the von Mises stress, $\sigma_e = \sqrt{\frac{3}{2}S_{ij}S_{ij}}$, σ_{ij} is the Cauchy stress tensor, and S_{ij} is the deviatoric part of σ_{ij}. $E^{'}$ and $\nu^{'}$ are given below:

$$E' = \frac{(1+\nu)(E_A - E_M)}{E_A E_M} \quad , \quad \nu' = \frac{\nu(E_M - E_A)}{E_M E_A}, \tag{2.20}$$

where E_M and E_A are the elastic moduli of austenite and martensite; ν is Poisson's ratio of the material ($\nu_A = \nu_M = \nu$), and a and b are defined as

$$a = \frac{1}{2}\left[\left(\frac{1}{E_M} - \frac{1}{E_A}\right)\frac{\sigma_{Ms}^2 - \sigma_{Af}^2}{2} + (\sigma_{Ms} - \sigma_{Af})\varepsilon_0\right], \tag{2.21}$$

$$b = \frac{1}{2}\left[\left(\frac{1}{E_M} - \frac{1}{E_A}\right)\frac{\sigma_{Mf}^2 - \sigma_{As}^2}{2} + (\sigma_{Mf} - \sigma_{As})\varepsilon_0\right], \tag{2.22}$$

σ_{Ms}, σ_{Mf}, σ_{As} and σ_{Af} are martensite start, martensite finish, austenite start and austenite finish stresses respectively; ε_0 is the equivalent transformation strain as shown in Figure 2.1b. $C(T)$ is phase change heat density, a detailed discussion of which is given in Zaki and Moumni [2]. α controls the slope of the stress-strain curve corresponding to martensite orientation through relation $(\sigma_{rf} - \sigma_{rs})/(\varepsilon_0)$, where σ_{rf} and σ_{rs} are orientation start and orientation finish stresses. β controls the level of orientation of martensite variants and is defined as $\sigma_{rf}/\varepsilon_0$. ε_{ori} the strain as a result of orientation of martensite variants, can be defined as follows [125]:

$$\varepsilon_{ij}^{ori} = \frac{3}{2}\varepsilon_o\frac{S_{ij}}{\sigma_e}. \tag{2.23}$$

Stresses σ_{ij} that are needed in the evaluation of transformation function, are calculated using asymptotic stress equations given below [144]:

$$\sigma_{xx} = \frac{K_I}{\sqrt{2\pi r}}\cos\frac{\theta}{2}\left[1 - \sin\frac{\theta}{2}\sin\frac{3\theta}{2}\right] + ..., \tag{2.24}$$

$$\sigma_{yy} = \frac{K_I}{\sqrt{2\pi r}}\cos\frac{\theta}{2}\left[1 + \sin\frac{\theta}{2}\sin\frac{3\theta}{2}\right] + ..., \tag{2.25}$$

$$\tau_{xy} = \frac{K_I}{\sqrt{2\pi r}}\cos\frac{\theta}{2}\sin\frac{\theta}{2}\cos\frac{3\theta}{2} + ... \tag{2.26}$$

where K_I is the Mode I SIF.

2.3. Evaluation of Stress Intensity Factor

SIFs that are needed in Equations 2.24, 2.25 and 2.26 are calculated using asymptotic near-tip opening displacement, U_y, and fitting to the equation the full displace-

ment field obtained from finite elements [145]:

$$\begin{aligned} U_y =& \frac{K_I}{2\mu_{tip}}\Big(\frac{r}{2\pi}\Big)^{\frac{1}{2}} \sin\frac{\theta}{2}\left(\frac{3-\nu}{1+\nu} - \cos\theta\right) \\ & - \frac{T\nu}{2\mu_{tip}(1+\nu)} r sin\theta + \frac{K_{II}}{4\mu_{tip}}\Big(\frac{r}{2\pi}\Big)^{\frac{1}{2}} \\ & \left(\frac{5\nu-3}{1+\nu}\cos\frac{\theta}{2} - cos\frac{3\theta}{2}\right) + A_1 r\cos\theta + u_{0y}, \end{aligned} \tag{2.27}$$

where T is T-stress, A_1 and u_{oy} are rigid body rotation and displacement, ν is Poisson's ratio, μ_{tip} is shear modulus of the crack tip. Using Abaqus, the edge-cracked problem shown in Figure 2.1a is solved for $P = 32$ N (to compare to results of Robertson *et al.* [35]). Assuming symmetry, only the upper half of the plate is modeled with eight-node biquadratic plane stress quadrilateral elements with reduced integration points (CPS8R). In the analysis, properties of Nitinol-SE508 from Nitinol Devices and Components Company (NDC) with austenite finish temperature (A_f) of 15^{o}C are used; missing parameters are derived from experimental data provided by the study of Pelton *et al.* [146].

All three values of K_I, K_{II}, and T with A_1 and u_{0y}, are obtained simultaneously through a least squares fit. K_{II} is calculated to be 0.03 MPa $\sqrt{m}$ which is small compared to $K_1 = 7.3$ MPa $\sqrt{m}$. If asymptotic equations with K_I alone are used neglecting K_{II}; K_I is obtained to be $7.35MPa\sqrt{m}$. Because K_{II} is small in this study the rest of the calculations are carried out using K_I only. Figure 2.2 shows displacement contour plots around crack tip that are obtained by least squares fit of FE data to Equation 2.27 and full field displacement contour plots obtained directly from FE.

The stress intensity factor is also calculated using the following equation [147]:

$$K = \frac{P}{B\sqrt{W}} f(\frac{a}{W}), \tag{2.28}$$

where $f(\frac{a}{W})$ is a geometric factor [38] with $P = 32N$ again. K_I is obtained to be $K_I = 7.5\ MPa\sqrt{m}$. As expected K_I calculated using Equation 2.28, where phase

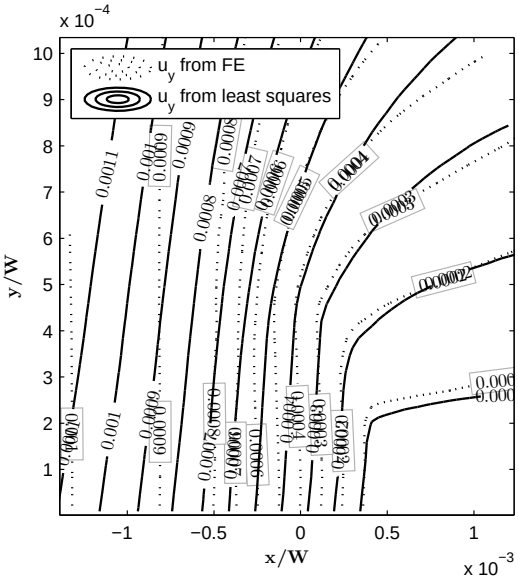


Figure 2.2. Contours of u_y.The crack tip is located at the origin and the coordinates x and y are normalized by W Dashed lines with values in boxes are FE results, solid lines are from least squares fit of Equation 2.27 to FE results.

transformation is not taken into account, is higher than the K_I determined using FE. As a result in subsequent calculations $K_I = 7.35\ MPa\sqrt{m}$ is used in asymptotic equations to calculate stresses and K_{II} which is very small compared to K_I is neglected.

In Figure 2.3 contours of σ_{yy} obtained using Equation 2.25 and contours obtained from Abaqus are plotted together. Around crack tip, the difference in σ_{yy} appears to be acceptable as shown in detail in Figure 2.3b.

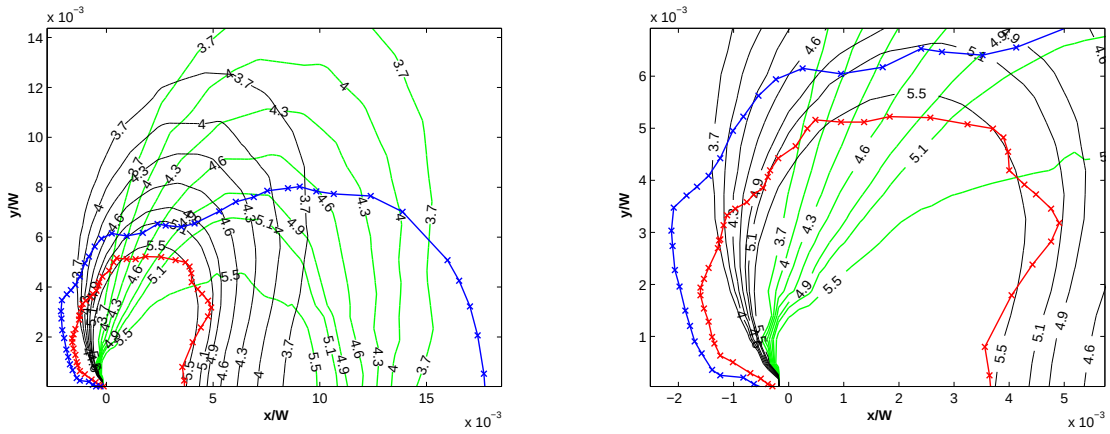
2.4. Evaluation of Transformation Region

Using asymptotic equations for σ_{ij}, σ_e is obtained as follows:

$$\sigma_e = \frac{K_I}{2\sqrt{\pi r}} \left[1 + \cos\theta + \frac{3}{2}\sin^2\theta \right]^{1/2}, \tag{2.29}$$

similarly,

$$\sigma_{ii} = \frac{K_I}{2\sqrt{\pi r}} \left[1 + \cos\theta \right]^{1/2}, \tag{2.30}$$



a b

Figure 2.3. (a) Contour plot of normalized opening stress, $\frac{\sigma_{yy}}{\sigma_0}$ (σ_0, far field applied stress), green lines: full field finite element solution, black lines: asymptotic field. Red line $\zeta = 1$, and the region between red and blue lines, $0 < \zeta < 1$. Crack tip is located at the origin. (b) close up view of $\frac{\sigma_{yy}}{\sigma_0}$ near the crack tip.

$$\varepsilon_{ij}^{ori}\sigma_{ij} = \varepsilon_o \frac{K_I}{2\sqrt{\pi r}} \sqrt{\left[1 + \cos\theta + \frac{3}{2}\sin^2\theta\right]}. \tag{2.31}$$

If Equations 2.29, 2.30 and 2.31 are inserted into Equation 2.19, with martensite volume fraction, $\zeta = 1$, and the result is equated to zero, the following equation will be obtained:

$$\begin{aligned} & E' \frac{K_I^2}{12\pi r_M} \left[1 + \cos\theta + \frac{3}{2}\sin^2\theta\right] \\ & + \frac{1}{2}\left(\frac{1}{3}E' + \nu'\right) \frac{{K_I}^2}{4\pi r_M} \left[1 + cos\theta\right] \\ & - C(T) + \varepsilon_o \frac{K_I}{2\sqrt{\pi r_M}} \sqrt{\left[1 + \cos\theta + \frac{3}{2}\sin^2\theta\right]} \\ & - (\Gamma + b) - \left(\alpha - \frac{\beta}{2}\right)\varepsilon_o^2 = 0. \end{aligned} \tag{2.32}$$

Equation 2.32 can then be solved for r_M, to obtain the extent of martensitic region around crack tip. Figure 2.4 shows martensitic transformation region obtained together with experimental measurements of Robertson *et al.* [35].

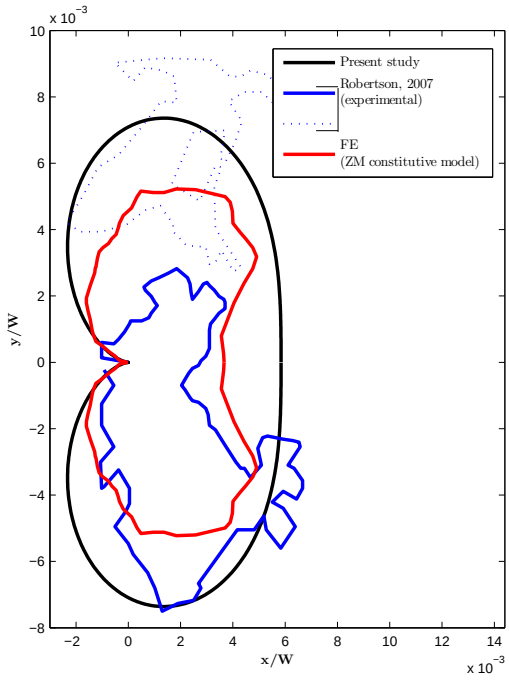


Figure 2.4. Martensitic region around crack tip.

In Figure 2.5, transformation function F_ζ used in this study is plotted using material properties of NiTi (SE-508) and an average plateau stress (σ_{ave}) of 370 MPa. As shown in Figure 2.5 the shape of the transformation function is similar to the von Mises yield function drawn with respect to principal stresses (σ_1 and σ_2). When $F_{\zeta=0}$ and $F_{\zeta=1}$ are compared it is observed that the difference between these curves are smaller on the sides (when $\sigma_1 \approx 0$), than the difference on the upper and lower regions.

2.5. Results and Conclusions

As it can be seen from Figure 2.4, the size and the shape of the martensitic region plotted using F_ζ are similar to those presented by Robertson *et al.* [35]. The yield criterion for Nitinol used by Lexcellent and Blanc [45] however predicts a transformation zone roughly six times larger than the experimental results of Robertson *et al.* [35].

According to Robertson *et al.* [35] some of the austenite grains may resist transformation as a result of grain orientation (local texture). Figure 2.4, dashed blue line represents the region of untransformed austenite grains surrounded by martensite as

a result of a local texture. If that region is included as well, results presented in this paper match even better with the experimental results of Robertson *et al.* [35].

Because the Equation 2.32 is given in closed form, the size and the shape of the transformation region around the crack tip can be evaluated for a given loading and material properties once the stress intensity factor is calculated properly. To show the effect of the SIF on the transformation region, change in the size of the region with increasing SIF is given in Figure 2.6.

This chapter began by a literature review about the studies estimating the phase transformation region around the crack tip; and followed by describing the method used to calculate the transformation region around the crack under Mode I loading. Finally, a good correlation between analytical calculations and experimental measurements is represented. In the next chapter, numerical calculations using ZM model to find the effect of phase transformation on fracture toughness of SMAs is presented.

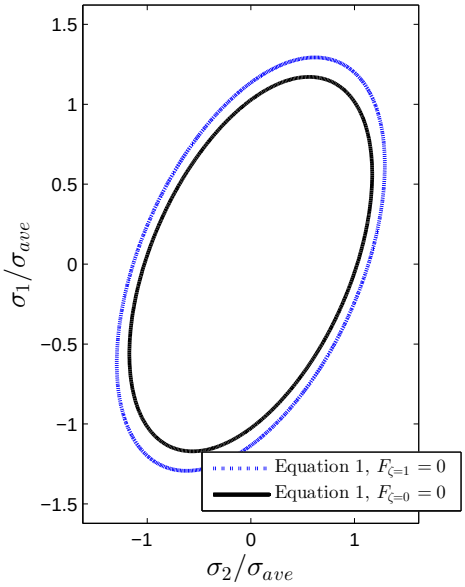


Figure 2.5. Transformation function, $F_\zeta = 0$, vs principle stresses.

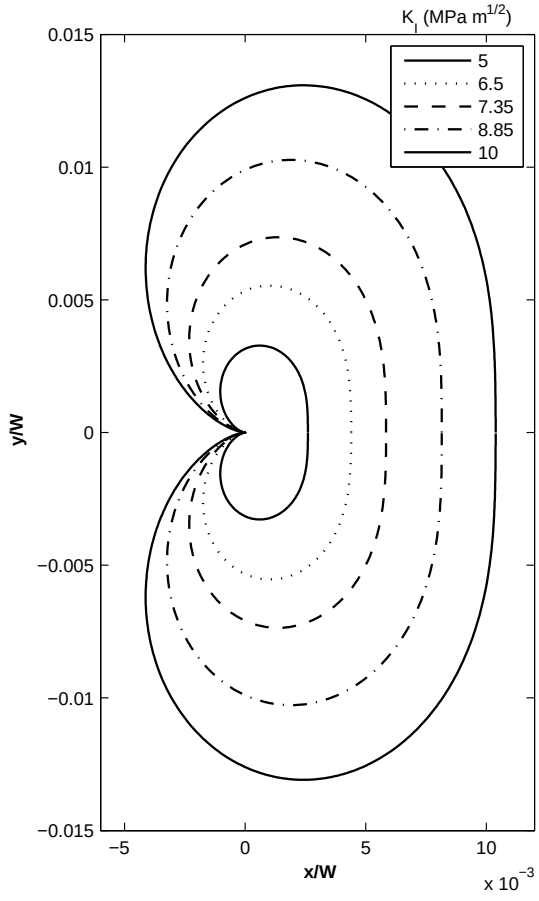


Figure 2.6. Effect of SIF on transformation region.

3. INVESTIGATION OF FRACTURE PARAMETERS OF SHAPE MEMORY ALLOYS UNDER MODE I LOADING

When a cracked NiTi specimen is loaded, stress increases around crack tip, and phase transformation occurs immediately. Exact closed form calculations of the stress field around the crack tip and fracture parameters are almost impossible due to the phase transformation around the crack tip and the non-homogeneous region that is created.

The objective of this chapter is to analyse the effect of phase transformation on fracture parameters of an edge-cracked NiTi plate. For this purpose, Abaqus is used with both ZM model and built-in Auricchio's SMA model. Under plane stress conditions and Mode I loading, SIFs, J-integrals, energy release rates, crack tip opening displacements, and T-stresses are calculated numerically. The results show that, J-integrals are contour dependent as a result of non-homogeneous region surrounding the crack tip. Therefore, energy release rate, G, cannot be calculated directly by equating J to G. Instead, strain energy output is directly used to calculate stress intensity factors. SIFs are also calculated through a least squares fit of displacements obtained from FE to asymptotic near-tip displacement field equation. Fracture toughness is discussed by studying the phase transformation region and the fracture parameters determined using ZM model and Auricchio's model.

3.1. Introduction

In SMAs, crack tip stresses induce phase transformation from austenite to martensite that affects fracture behavior of the material. Although many researchers dealt with the constitutive modeling of SMAs to understand their mechanical behavior and remarkable capabilities, there is still room for discussion of fracture parameters, such as SIFs, J-integrals, energy release rates, CTOD, and fracture toughness.

One of the first studies determining SIF changes at crack tip in materials un-

dergoing martensitic transformation was done by McMeeking and Evans [12]. They combined Eshelby's technique [13] with weight functions given by Paris *et al.* [148] and calculated the magnitude of the SIF change around the crack tip using, $\Delta K_I = -0.22 e^T V_f \sqrt{w(\bar{R})}/(1-\nu)$, where e^T is the transformation strain, V_f is the volume fraction of martensite, $\bar{R}$ is the average radius of the particles undergoing phase transformation, and $w(\bar{R})$ is the transformation zone width depending on $\bar{R}$. They concluded that phase transformation creates a residual strain field around the crack tip that limits crack opening and therefore increases toughness. In addition to this, they showed that SIF does not change at the initial transformation zone prior to crack growth, it reduces when the transformation zone extends towards to crack surface and its reduction reaches a maximum level after some crack propagation.

Birman [18] investigated the effect of phase transformation on stress intensity factor in a center-cracked SMA plate under Mode I loading using the transformation equation of Tanaka and Sato [40] in combination with crack tip asymptotic stress equations. He claimed that the effect of phase transformation on SIF was relatively small and that SIF could be calculated using the properties of austenite when the external stresses are lower than the yield stress of martensite. He concluded that, extensive experimental studies are needed to estimate the effect of phase transformation on the fracture toughness of SMAs.

Simha [21] calculated the transformation toughening for a stationary crack under Mode I loading in Zirconia–Toughened Ceramics (ZTC). He obtained a relation for toughening in super critical ZTC by using, $J_{far} - J_T = 2h\sigma_1\theta_t$, where $h = \frac{(1+\nu)}{4\pi\sqrt{3}}\left(\frac{K}{\sigma_1}\right)^2$ and $K = \sqrt{\frac{JE}{(1-\nu^2)}}$. His results showed that, the toughness increases due to the energy stored in the wake region and the energy that goes to phase transformation. ZTC undergoes a martensitic transformation similar to SMAs, and the developed model can be used to investigate pseudo-elastic crack propagation in polycrystalline SMAs.

Yi and Gao [22] used the phase transformation function given by Sun and Hwang [15, 16] together with the asymptotic stress equations of LEMF to estimate the transformation region under Mode I loading. They calculated the SIF around the crack tip

using Eshelby's technique [13] and weight functions given by McMeeking and Evans [12]. They determined the reduction of SIF using; $\Delta K^{tip} = \frac{E}{1-2\nu} \int_A (\varepsilon^t h) dA$, where A is the transformation area, ε^t is the transformation strain, h is the shape function given by McMeeking and Evans [12]. When the crack advances, the shape of the transformation zone changes into a new shape with a long transformed wake. Their results showed that, crack tip SIF decreases drastically when the temperature increases. In addition to that, they also found out that phase transformation reduces crack tip SIF, increases toughness, and when the ratio of austenite to martensite Young 's moduli increases, toughness increases. In a following study, Yi *et al.* [149] extended their previous work [22] to mixed mode loading and they arrived to the same conclusion as McMeeking and Evans [12] that the phase transformation reduces energy release rate and increases toughness in SMAs.

Wang [29] investigated the effect of notch geometry on phase transformation and fracture toughness using NiTi compact tension specimens with different notch geometries under Mode I loading. He defined NiTi's behaviour as an elastic–plastic material by digitizing stress–strain data in Abaqus, and showed that unlike the traditional metals changing the notch shape from blunt to acute changes the fracture behavior from brittle to ductile. Using the same approach, Wang [30] studied the effects of phase transformation on fracture toughness in an SMA CT specimen under Mode I loading, and stated that the notch tip is blunted by transformation strain that results in the release of notch tip stresses and increases fracture toughness.

Experimental methods used to measure fracture parameters of standard materials are implemented to SMAs to understand the change in fracture toughness due to phase transformation. Using X-ray diffraction, Robertson *et al.* [35] obtained the strain field around the tip of an edge-cracked thin NiTi specimen under Mode I loading. Their results showed that, the redistribution of stress field as a result of phase transformation reduces stresses near the crack tip and increases the fracture resistance. Daly *et al.* [36] used DIC to calculate strain fields in an edge-cracked thin NiTi sheet under Mode I loading. They calculated SIF using LEFM and obtained an empirical expression between the extent of transformation region and K_I. As a result, they cal-

culated a relatively high value of fracture toughness, K_C, for NiTi, which indicates contribution of phase transformation for the toughening of the alloy. Gollerthan *et al.* [37] performed displacement controlled experiments using NiTi CT specimen, measured applied far field load P and calculated the critical stress intensity factor using the relation, $K_C = \frac{P}{B\sqrt{W}} f(a/W)$, where B, W and $f(a/W)$ are given in the standards [38]. They used K_C and Irwin's plasticity corrected equation to estimate the length of the phase transformation zone. Their results confirmed that, the calculated phase transformation length qualitatively agrees with their experimental observation.

Studies conducted till date showed that, to be able to discuss fracture parameters phase transformation region around the crack tip has to be determined accurately. Lexcellent and Thiebaud [43] presented an analytical approach using the constitutive model of Raniecki and Lexcellent [44], also used in Lexcellent and Blanc's [45] paper, together with asymptotic crack tip stress equations to determine the transformation region around the crack tip under Mode I loading. They used an average value of SIF as it is also proposed by Freed and Banks-Sills [41]; $(K_I^{app} + K_I^{tip})/2$, where K_I^{app} is the applied SIF and K_I^{tip} is the SIF governing the region near crack tip. Their results showed a big difference with the experimental results of Robertson *et al.* [35]. Falvo and Furgiuele et al. [46] used both, $\sigma_y = K_I/\sqrt{2\pi r}$ and Irwin's plasticity corrected formula to predict the extent of the stress-induced martensitic transformation. They compared their analytical results with FEA results, and showed that using Irwin's correction yields results closer to FEA results. A different approach to get an analytical solution to define phase transformation region is proposed by Ma [47]. He used Green's function to find the effect of martensitic and ferro–elastic transformation on fracture toughness in a semi-infinite crack under plane stress. His formulation, indicating the changes in stress intensity factor because of phase transformation, was in agreement with the result obtained by McMeeking and Evans [12]. Maletta and Furgiuele [48] proposed an analytical method, which is in agreement with the performed FEA to predict the extent of phase transformation region using Irwin's corrected formulation in combination with $K_I = \sigma^{\infty}\sqrt{\pi\alpha}$ in an infinite NiTi plate having a central crack under Mode I loading. In the following study, Maletta and Young [49] extended the previous work [48] to plane strain conditions and compared their results to experimental results of Gollerthan *et al.*

[50]. They observed that, experimentally calculated phase transformation length was in between the lengths they calculated for plane stress and plane strain. In a later study, Maletta and Furgiuele [51] calculated the extent of phase transformation region using their previous approach [48] and two different SIFs: one for austenitic region and another one for the transformed martensitic region near the crack tip. Their results showed that, martensitic or crack tip SIF was smaller than the LEMF predictions and the mismatch between austenite and martensite elastic moduli causes toughening at the crack tip.

Using Dugdale's method [53], Baxevanis and Lagoudas [52] calculated J-integral, CTODs, and size of the martensite transformation region around the tip of a center-cracked infinite SMA plate under Mode I loading. They found that, when the stress level is above yield stress, phase transformation region size increases with increasing maximum transformation strain, and the existence of phase transformation region decreases the size of the plastic zone. In a following work, Baxevanis *et al.* [55] calculated the size and shape of the martensitic transformation region and J-integral near an edge-crack using the constitutive model of Lagoudas *et al.* [56]. Their numerical simulation showed that, around the crack tip, J-integral is path dependent and the difference between the crack tip, J_{tip}, and far field applied J-integral, J_{∞}, is smaller than that difference obtained in elastic–plastic materials.

Main objective of this chapter is to understand the effect of phase transformation on fracture behavior of a superelastic NiTi. In this chapter, different methods estimate SIF when compared to other studies. Using finite elements, transformation region around the crack tip is studied, strain energy is calculated and fracture mechanics properties, such as J-integrals, energy release rates, stress intensity factors, crack face opening displacements (CFODs), and CTODs, are discussed to understand the effect of phase transformation on fracture behavior in a superelastic NiTi plate. In the first section, problem geometry and constitutive model used in FE analysis is presented, then phase transformation regions and J-integrals are calculated around the crack tip using two different material models. In the next part, the results of fracture parameter analyses are presented. Finally fracture toughness is discussed, and results

are tabulated.

3.2. Problem Statement and FEA

A rectangular plate with an edge crack situated along its x-axis is subjected to Mode I loading as shown in Figure 3.1a. Finite element is used to solve the problem. Using symmetry, only the upper half of the plate is modeled with reduced integration plane stress elements (CPS8R) (see Figure 3.1b). Because the non-linear material response requires very fine meshes, model is divided into regions with different mesh sizes (see Figure 3.1c). As shown in Figure 3.1d, around the crack tip a circular finer mesh is used and the mesh density increased towards the crack tip. At the crack tip one side of the eight noded CPS8R element collapses to a node at the tip and midside nodes are located to 1/4 of the element edge length away from the tip.

In the finite element analyses, the ZM [2], and built–in Auricchio–Taylor–Lubliner models [3] are used through user defined material subroutine (UMAT) in Abaqus. The stress-strain and stress-temperature curves of superelastic Nitinol indicating the material parameters used in Auricchio's model are plotted in Figure 3.2 and material properties are given in Table 3.2; where E_A is elastic modulus and ν_A is Poisson's ratio of austenite, E_M is elastic modulus and ν_M is Poisson's ratio of martensite, ε_0 is transformation strain, $\left(\frac{\delta\sigma}{\delta T}\right)_L$is rate of change of stress with respect to temperature during loading, σ_L^S is the starting stress and σ_L^E is the ending stress of forward transformation, T_0 is the reference temperature, $\left(\frac{\delta\sigma}{\delta T}\right)_U$is the rate of change of stress with respect to temperature during unloading, σ_U^S is the starting stress and σ_U^E is the ending stress of reverse transformation. The stress–strain curves of a NiTi specimen under uniaxial loading obtained using ZM and Auricchio's model with the the material properties given in Tables 3.2 and 3.1, are plotted in Figure 3.3. The conversion of material parameters from ZM to Auricchio's model is done with the help of the parameter identification section represented by Zaki and Moumni [2].

A displacement of $u = 0.1\ mm$, is applied to the edge-cracked rectangular plate shown in Figure 3.2. The phase transformation regions calculated using the two mate-

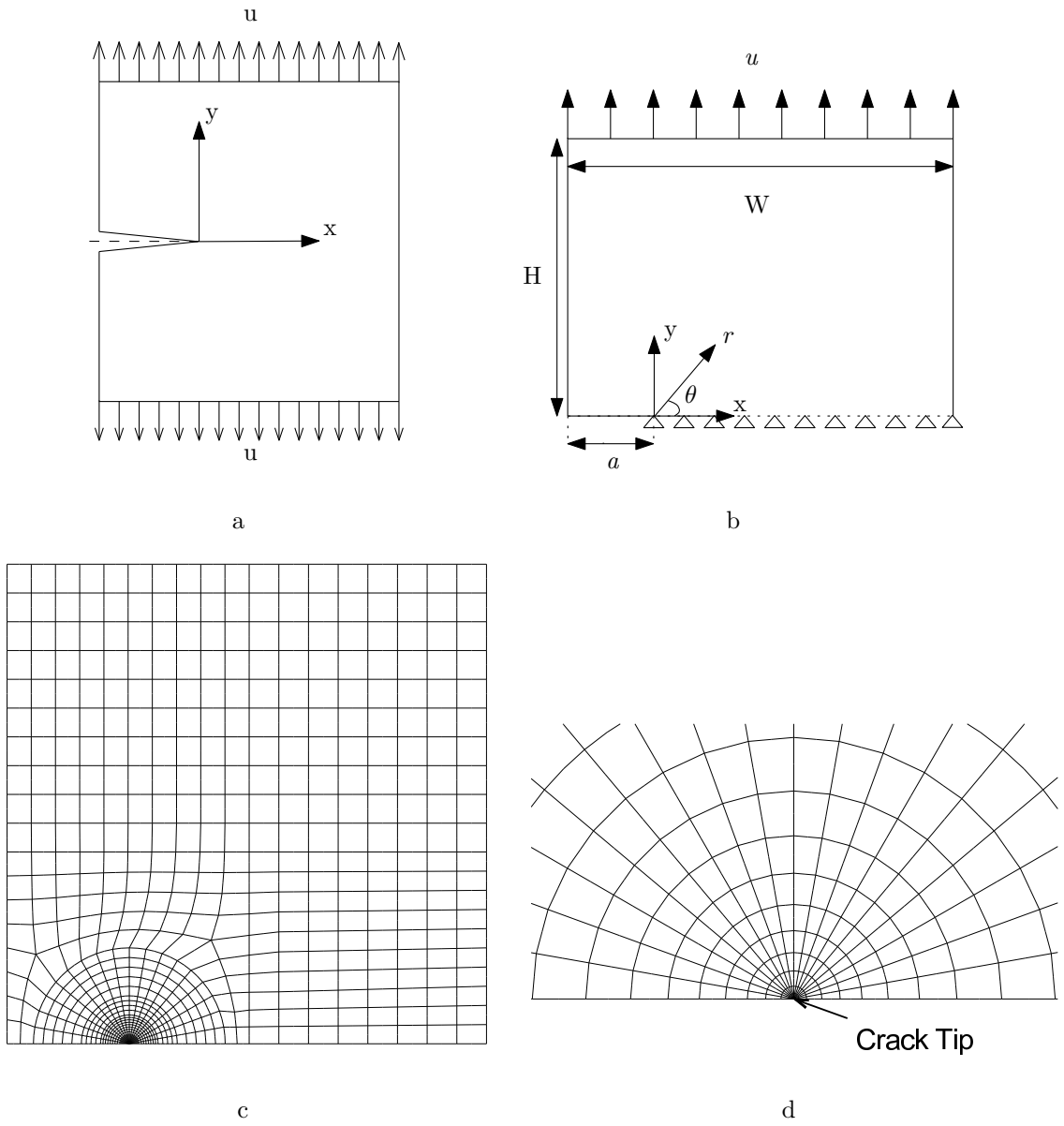


Figure 3.1. (a) Edge-cracked thin SMA plate, (b) Geometry of the 2-D edge-cracked specimen, (c) Mesh of 2-D edge-cracked specimen, (d) Mesh configuration close to the crack tip ($H = 100\ mm$, $W = 100\ mm$ and $a = 20\ mm$).

rial models are compared in Figures 3.4 and 3.5. The comparison of the results shows that the phase transformation start regions ($\zeta = 0^+$) are close, on the other hand, the martensite region ($\zeta = 1$), calculated using ZM model, is smaller.

When the crack length is increased, stresses around the crack tip increases and transformation region around the tip enlarges in the direction of crack growth. In

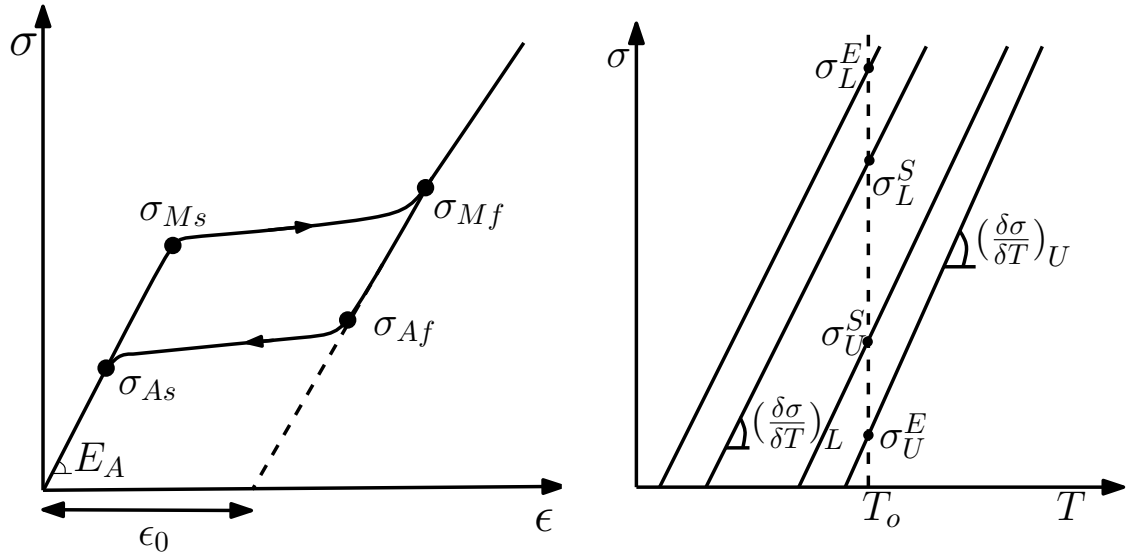


Figure 3.2. (a) Stress-strain graph, (b) stress-temperature graph of Nitinol [1].

Table 3.1. Material parameters used in ZM model [2].

E_A	61500 MPa
E_M	24000 MPa
a	6.8920 MPa
b	6.9091 MPa
Γ	4.6556 MPa
α	2750 MPa
β	5500 MPa
Y	110 MPa
$C(T)$	15.634 MPa
ε_0	4 %
ν	0.3

Figure 3.6, ζ values along the crack growth direction, starting from the crack tip are plotted using two different crack lengths ($a/W = 0.2$ and $a/W = 0.4$), and it is observed that Auricchio's model calculates higher ζ at any distance away from the crack tip. Figure 3.6 shows that, when the crack length is increased, stresses around the crack tip increase and transformation region around the tip enlarges in the direction of crack

Table 3.2. Material parameters used in Auricchio's model [3].

E_A	61500 MPa
E_M	24000 MPa
$\nu_A = \nu_M$	0.3
$\left(\frac{\delta\sigma}{\delta T}\right)_L = \left(\frac{\delta\sigma}{\delta T}\right)_U$	5.71 MPa/K
σ_L^S	570 MPa
σ_L^E	575 MPa
σ_U^S	305 MPa
σ_U^E	300 MPa
ε_0	4 %
T_0	70 C

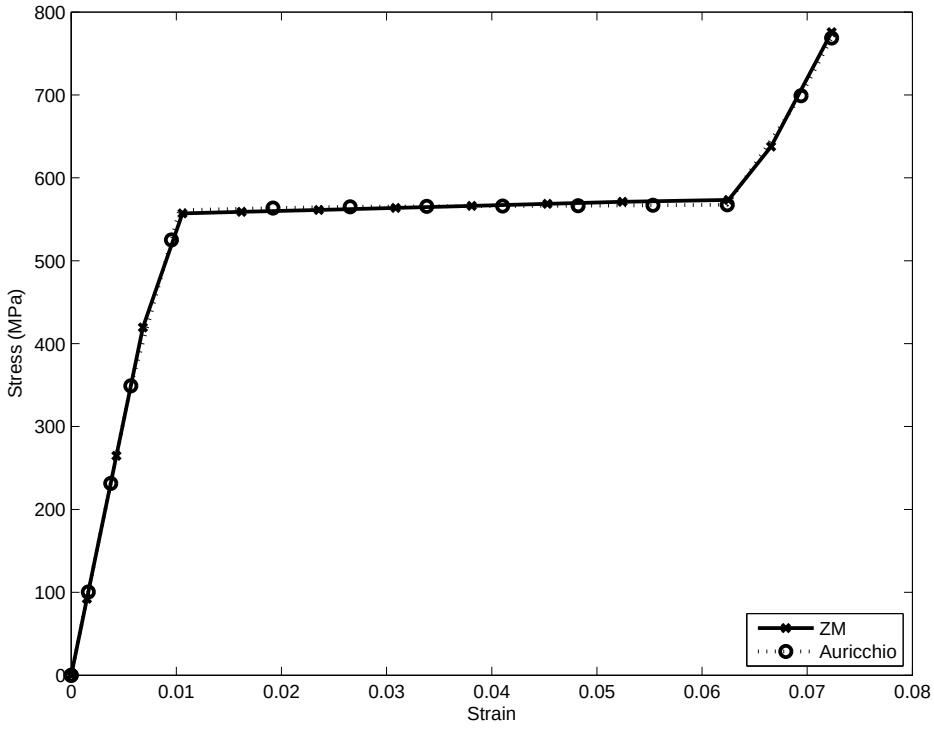
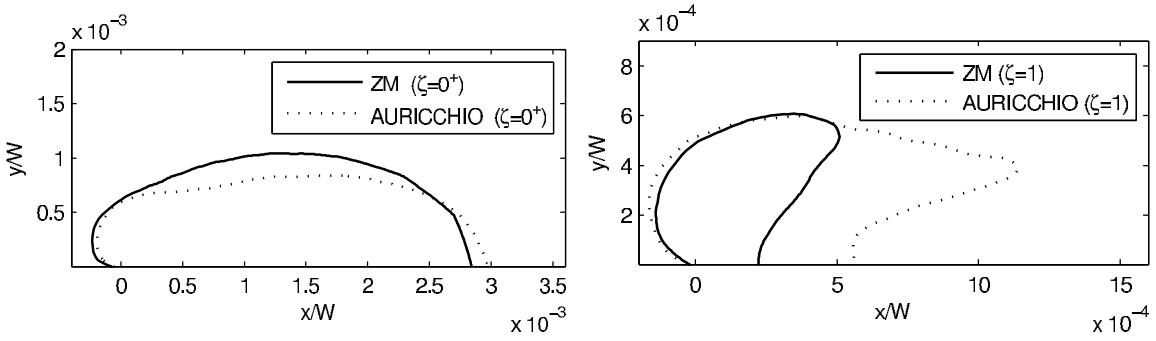


Figure 3.3. Stress-strain relation simulated in Abaqus using both ZM and Auricchio Models.

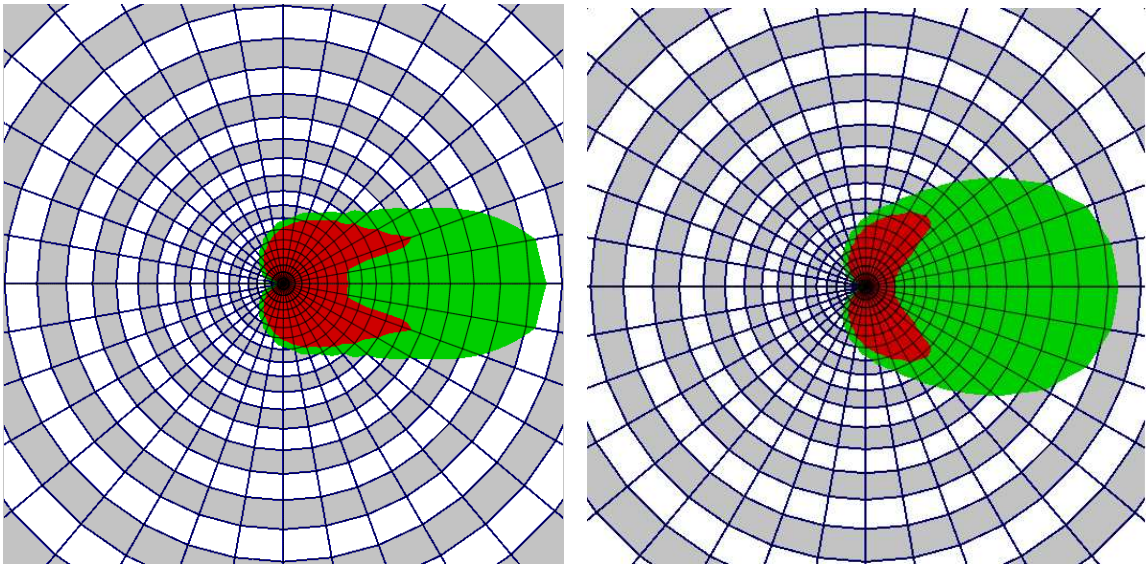
growth with an increase in ζ.

In Figure 3.7 σ_{yy} contours calculated around the crack tip are compared. Higher



a b

Figure 3.4. (a) Phase transformation regions, $\zeta = 0^+$, (b) Full martensite region, $\zeta = 1$, $(a/W = 0.40)$.



a Auricchio's model b ZM model

Figure 3.5. Transformation region, red $(\zeta = 1)$, green $(0 < \zeta < 1)$ and J-Integral contours (white and gray), $(a/W = 0.40)$.

stresses are obtained when ZM model is used, which predicts a smaller martensite region. In Figure 3.8, σ_{yy}/σ_T curves calculated along a radial path in the transformation region using ZM model and Auricchio's model are plotted and compared to those of a linear elastic homogeneous material having properties identical to austenitic phase of NiTi. This comparison shows that, phase transformation lowers stresses around the crack tip. Figure 3.8 also shows that, the shape of the σ_{yy} curve plotted for NiTi is similar to that calculated by Carka and Landis [142] for an elastic–perfectly plastic material.

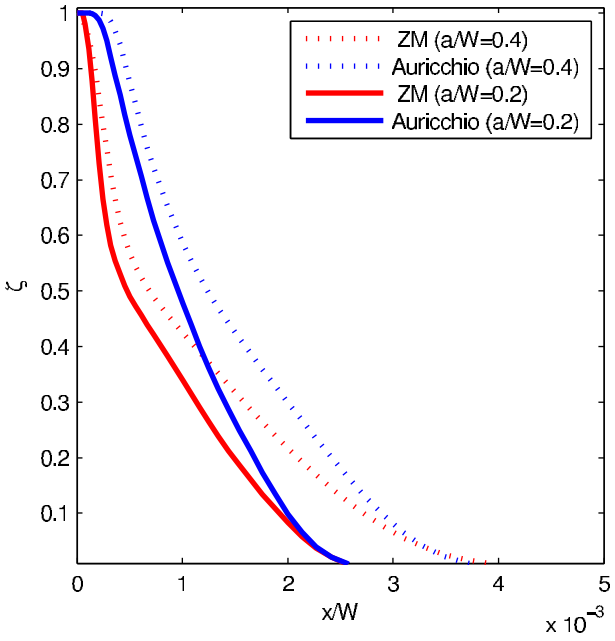


Figure 3.6. Martensite fraction, ζ along the crack tip in positive x direction as shown in Figure 3.2, u=0.1 mm.

3.3. Fracture Parameters

3.3.1. J-Integral

The J-integral, developed by Rice [150], is a widely used fracture parameter to calculate the strain energy release rate for linear elastic materials. In linearly elastic homogeneous materials with a uniform temperature distribution, J-integral is contour independent and equal to G. Therefore, the energy release rate, G, can be used to determine the stress field. Rice and Rosengren [151] showed that for non-linear materials (e.g. power- law hardening materials) J-integral can be used to define stress field close to the crack tip.

In Abaqus the J-integral is calculated by evaluating the following relation computationally:

$$J = \int_{\Gamma} w dy - \int_{\Gamma} T_i \frac{\partial u_i}{\partial x} ds, \tag{3.1}$$

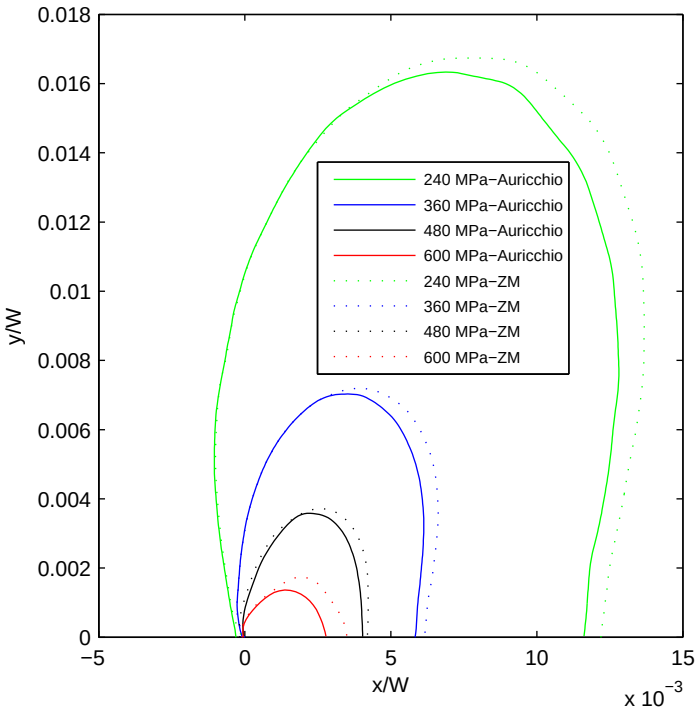


Figure 3.7. Comparison of σ_{yy} contours.

where w is the strain energy density, T_i is the traction vector, ds is the length increment along the path Γ. In this study, J-integrals are calculated along circular paths using ZM and Auricchio's models and results are plotted in Figure 3.9. Results of J-integral calculation show that the non-homogeneous material zone near the crack tip yields a contour dependent J-integral that converges to a far field value away from the tip, that is called J_∞ here.

As shown in Figure 3.9, J-integral values decrease and reach a minimum value; then, the central angle of the J-integral calculation paths passing through full martensite region gets smaller and J-integral starts to increase until the end of transformation region and converges to a constant value denoted as J_∞. The shape of the J-integral curve represented in Figure 3.9 is in agreement with the J-integral results obtained by Baxevanis *et al.* [55] for SMA. In Figures 3.10 and 3.11 J-integrals calculated for different crack lengths normalized by J_∞ is shown. When the crack length increases, the stresses increase and transformation regions enlarge. As a result, as it can be seen from Figures 3.10 and 3.11, J–integral curves shifts right upon increasing crack length.

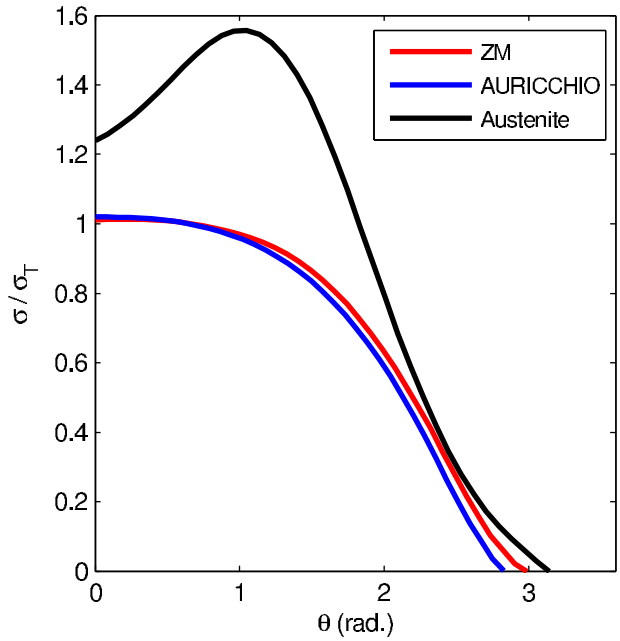


Figure 3.8. Angular variation of the $\frac{\sigma_{yy}}{\sigma_T}$ where σ_T is the average transformation stress along a radial path ($r = 0.18mm$). The crack tip is located at the origin. ($a/W = 0.40$ and $u = 0.1\ mm$).

3.3.2. Discussion on Strain Energy Stored

When there is no dissipated energy in the form of heat, the external work done on an elastic body is stored in the form of strain energy. The total strain energy balance can be written as:

$$E = U^e + U^p + U^{tr}, \tag{3.2}$$

where U^e is elastic strain energy, U^p is the energy dissipated through plastic deformation and U^{tr} is the energy dissipated in phase transformation. In this study it is assumed that there is no plastic deformation, i.e., $U^p = 0$.

Abaqus outputs energy terms through following commands; ALLSE gives the total elastic strain energy; ALLPD is the transformation strain energy; ALLIE is the total strain energy and $ALLIE = ALLSE + ALLPD$; ALLKE is the kinetic energy; ALLWK is the external work; and ETOTAL represents the total energy for the whole model, $ETOTAL = ALLKE + ALLIE - ALLWK$. ELSE and ELPD represents

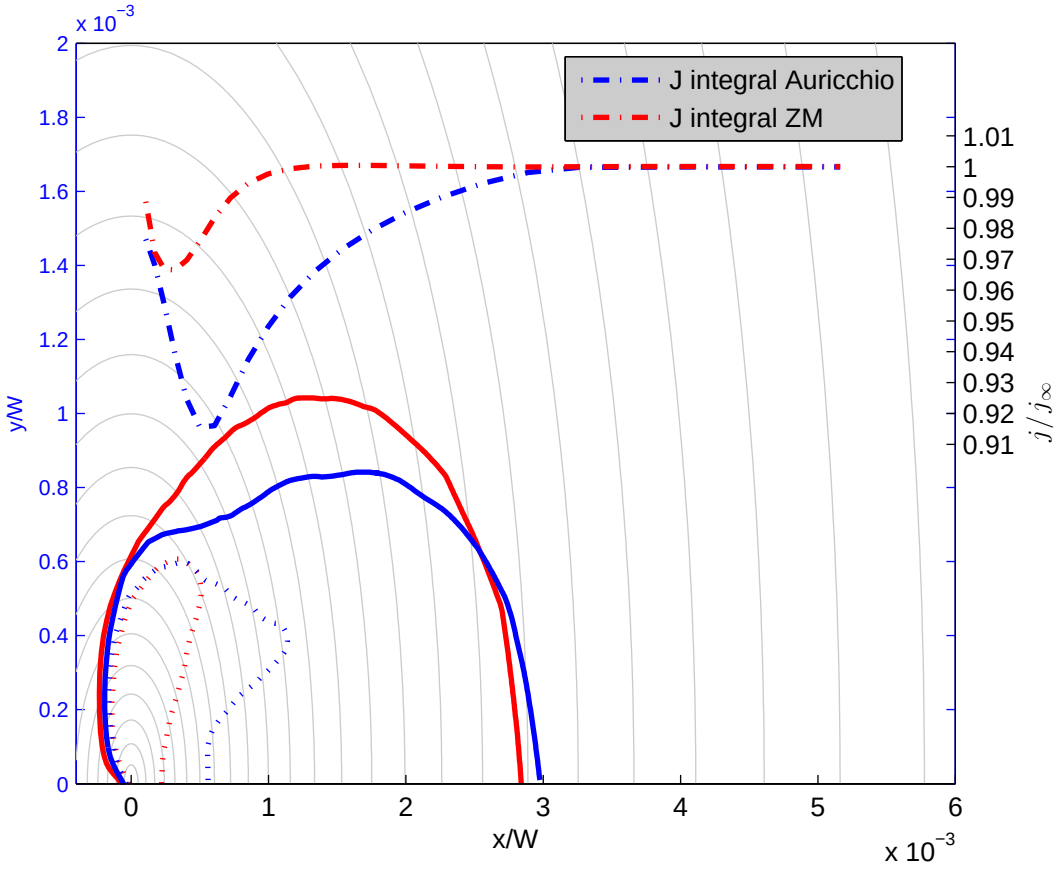


Figure 3.9. Solid lines are the phase transformation start boundary ($\zeta = 0^+$), dotted lines represents full martensite region ($\zeta = 1$), dashed lines are J-integral curves, circular gray curves are J-integral calculation contours ($a/W = 0.40$ and $u = 0.1\ mm$).

elastic and transformation strain energies respectively, for a single element.

As shown in Figure 3.12, the elastic strain energy is increasing during loading, whereas the transformation strain energy remains zero until the phase transformation starts. There is a small-scale phase transformation at the crack tip; as a result the transformation energy is very small compared to elastic strain energy and ALLSE/ALLWK is very close to 1 (ALLKE=0). ELPD curve remains zero up to, $u/u_T = 0.4$, where $u_T = 1\ mm$ represents the displacement at the end of the increment, over this point ELPD starts to increase together with the start of phase transformation, and finally it becomes constant when material point is fully transformed into martensite.

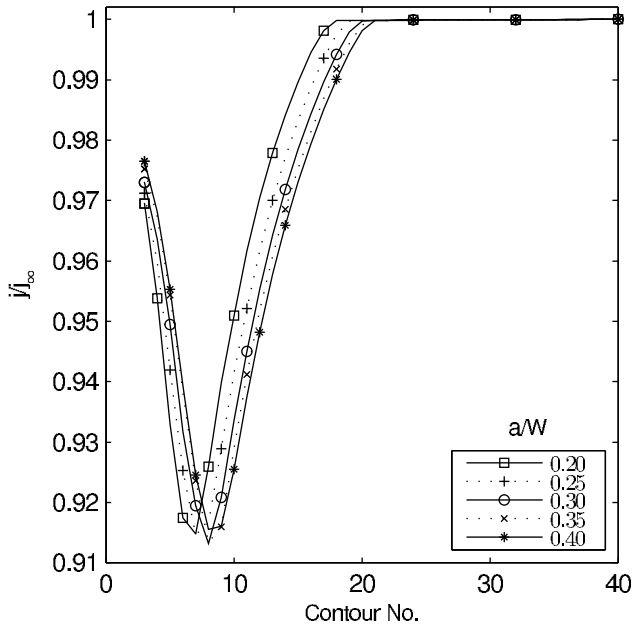


Figure 3.10. J-integrals calculated using Auricchio's model for different a/W ratios, u=0.1mm.

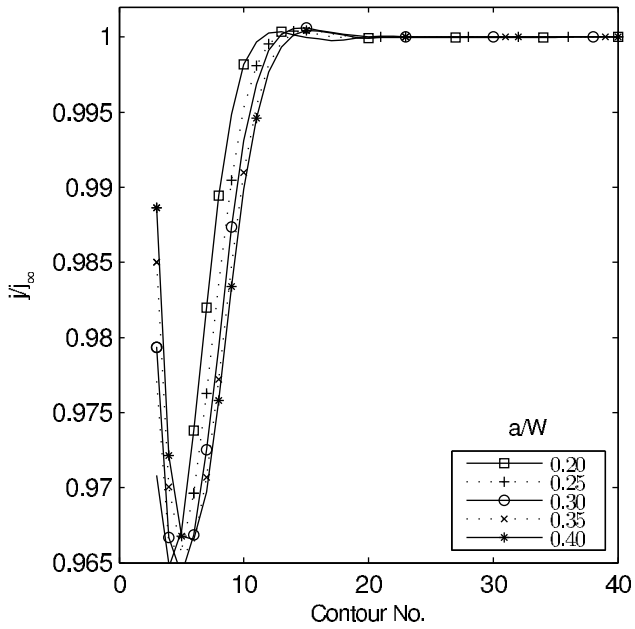


Figure 3.11. J-integrals calculated using ZM model for different a/W ratios, u=0.1mm.

3.3.3. Stress Intensity Factor Calculations Using Strain Energy Release Rate

As shown in Figure 3.9, J-integral is contour dependent, hence it cannot be used directly in SIF calculations by simply equating J to G. In this section, the energy

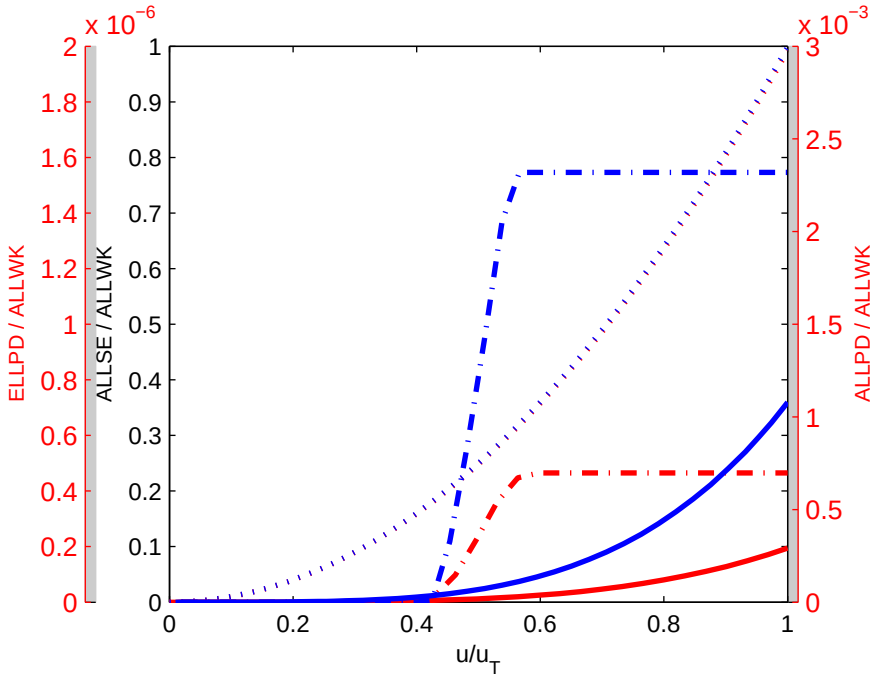


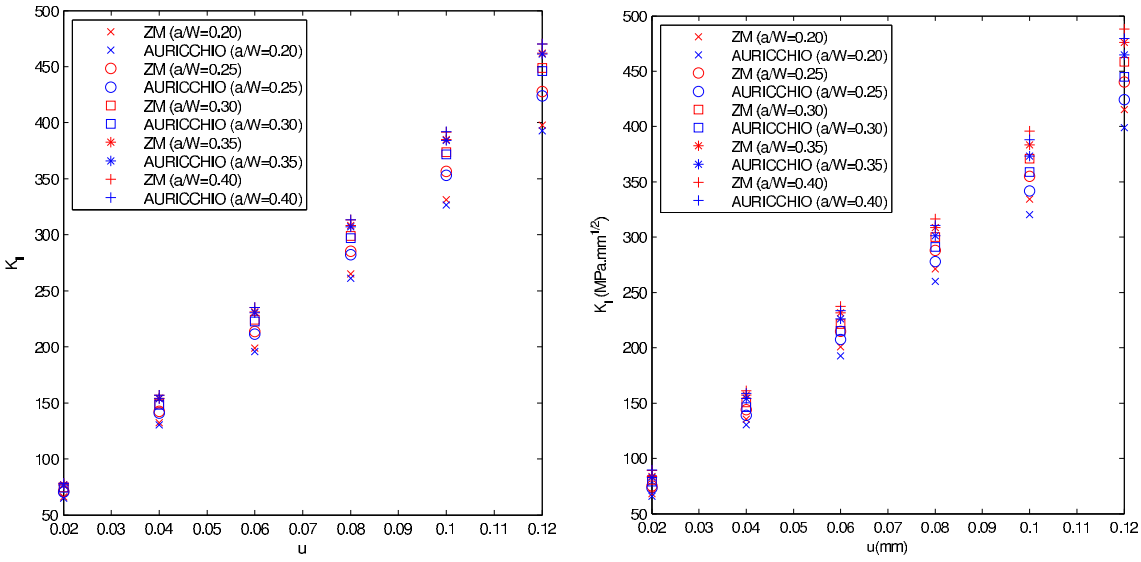
Figure 3.12. Change of ALLSE (dotted line), ALLPD (solid line) and ELPD (dash line) during loading, ($u_T = 0.10\ mm$, $a/W = 0.40$).

release rate G is calculated directly from the strain energy output of Abaqus using $\frac{\Delta U}{\Delta A}$, and SIFs, are estimated through equation, $G = {(K_I^G)^2}/{E_{Tip}}$. The results are plotted in Figure 3.13a. Crack tip becomes martensite at early stages of loading and while calculating G, E_{Tip} is set to elastic modulus of martensite, E_M. A similar method is used by Jin and Batra [152] and Anlas *et al.* [153] for functionally graded materials.

3.3.4. Stress Intensity Factor Calculations Using Full Displacement Field and Asymptotic Equations

SIFs are also calculated by fitting the full displacement field obtained from finite elements to the asymptotic displacement field equation, U_y, given below [145]:

$$U_y = \frac{K_I}{2\mu}\left(\frac{r}{2\pi}\right)^{\frac{1}{2}} sin\frac{\theta}{2}\left(\frac{3-\nu}{1+\nu} - cos\theta\right) - \frac{T\nu}{2\mu(1+\nu)} r sin\theta$$
$$+\frac{K_{II}}{4\mu}\left(\frac{r}{2\pi}\right)^{\frac{1}{2}}\left(\frac{5\nu-3}{1+\nu}cos\frac{\theta}{2} - cos\frac{3\theta}{2}\right) + A_1 r cos\theta + u_{0y}, \qquad (3.3)$$



a b

Figure 3.13. (a) SIF calculated using G vs. u (b) SIF calculated using full field displacement equation vs. u.

in the equation above, T is T-stress, A_1 and u_{oy} are rigid body rotation and displacement respectively, ν is the Poisson's ratio, μ is the shear modulus of martensite at the tip, r and θ are the polar coordinates with the origin centred at the crack tip. Least squares fit of displacement values obtained from finite elements to Equation 3.3 around the crack tip is shown in Figure 3.14. SIFs (K_I^{disp}) estimated through least squares fit are represented in Figure 3.13b. As shown in Figure 3.15, SIFs calculated using ZM constitutive model are higher than those obtained using Auricchio's model. This result is in agreement with the previous findings, and implies that when the ZM model is used, less energy is dissipated through phase transformation compared to that of Auricchio's model. Figure 3.15 shows that, although K_I^{disp} and K_I^G calculated using the two material models are not the same, they are close to each other. In Table 3.3 SIFs K_I^G, K_I^{disp} and K_I^∞ calculated using J_∞ are tabulated. The difference between K_I^{disp} and K_I^G given in Table 3.3 show that, when ZM model is used, SIFs predicted using both methods are close to each other.

The region of asymptotic dominance close to the crack tip stress is quantified by

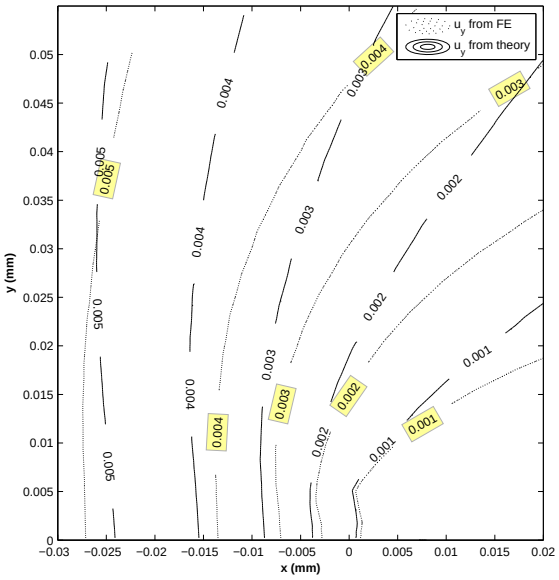


Figure 3.14. Displacement field around the crack tip calculated using ZM model, a/W =0.40.

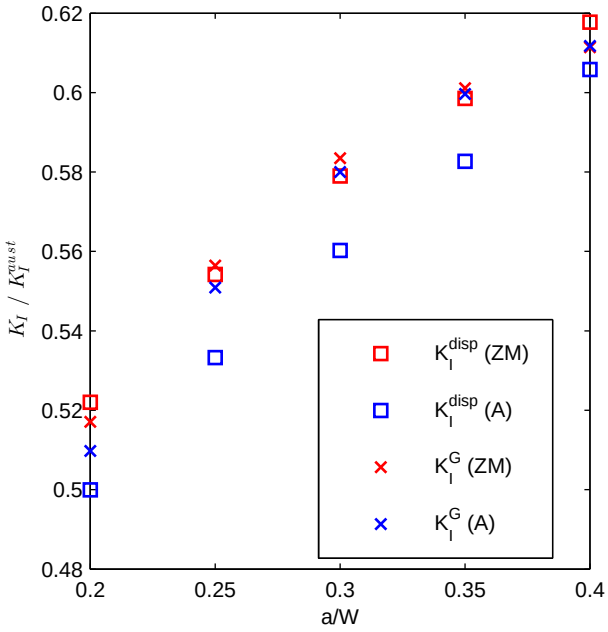


Figure 3.15. Comparison of stress intensity factors normalized by K_I^{aus}, which is the SIF calculated for a linear elastic material with material properties identical to NiTi in the austenitic phase. (ZM: Zaki–Moumni model A: Auricchio's Model).

the following error e:

$$e = \frac{\|\sigma_{ij}^{FE} - \sigma_{ij}^{A}\|}{\|\sigma_{ij}^{A}\|}, \tag{3.4}$$

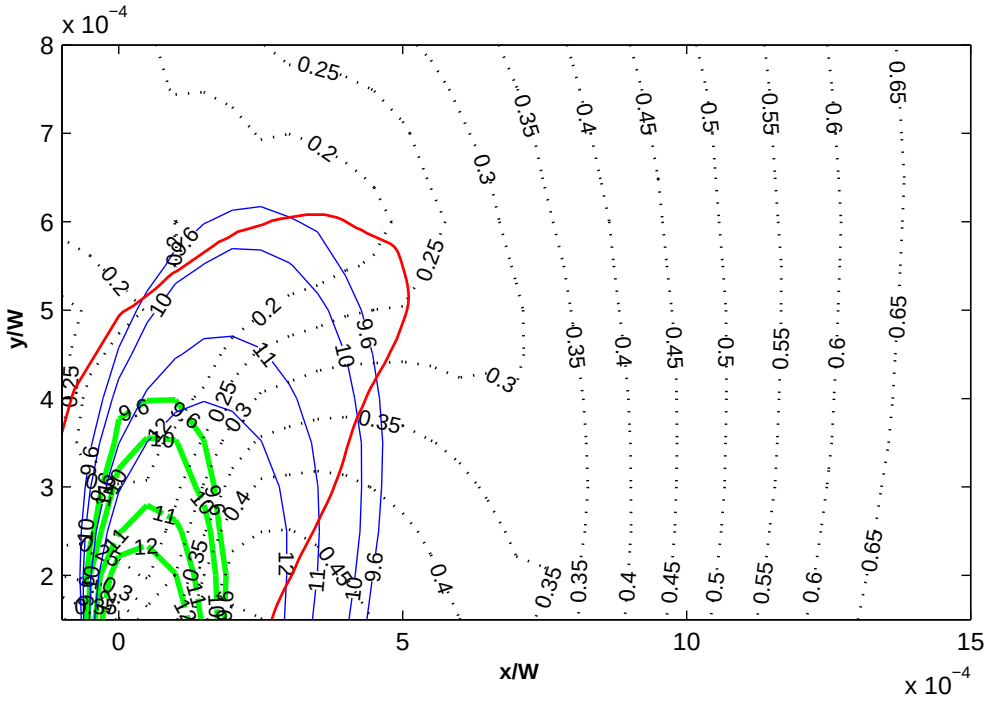


Figure 3.16. Red line represents the fully martensite region, blue and green lines are contour plots of $\sigma_{ij}^{A}/\sigma_{app}$ and $\sigma_{ij}^{FE}/\sigma_{app}$ respectively, and dashes black lines are e contours (a/W =0.40, $u = 0.1\ mm$,σ_{app} is the applied load).

where σ_{ij}^{FE} are stresses obtained from finite elements analysis using ZM model and σ_{ij}^{A} are stresses obtained from asymptotic equations. Figure 3.16 represents the contour plots of e, shows that the stress deviation decreases towards the crack tip and an error of 25% is maintained in the martensite region.

3.3.5. Calculating the Extent of Transformation Region Using T-Stresses

In this section, least squares fit of displacement field equation (Equation 3.3) to FEA results is used to calculate T-stresses. When θ=0, the equivalent stress derived using asymptotic stress equation considering T-stresses is given by:

$$\sigma_{VM}^{2} = T^{2} + T\frac{K}{\sqrt{\pi r_T}} + \frac{K^{2}}{\pi r_T}, \tag{3.5}$$

Table 3.3. Comparison of SIFs.(Units: K $(MPa.mm^{1/2})$, $G \approx \frac{\Delta U}{\Delta A}$ and J $(\frac{mJ}{mm^2})$, A : Auricchio Model, ZM: Zaki Moumni model.

a/W	J_∞	K_I^∞	$G \approx {}^{\Delta U}/_{\Delta A}$	K_I^G	K_I^{disp}	K_I^G-K_I^{disp})/K_I^G
0.20-A	4,383	324,327	4,445	326,626	320,330	192.8 %
0.20-ZM	4,533	329,838	4,574	331,333	334,477	25.8 %
0.25-A	5,138	351,165	5,192	352,987	341,684	320.2 %
0.25-ZM	5,265	355,481	5,297	356,534	355,108	40.0 %
0.30-A	5,713	370,297	5,755	371,633	358,972	340.6 %
0.30-ZM	5,801	373,136	5,823	373,848	370,984	76.6 %
0.35-A	6,120	383,264	6,152	384,236	373,337	283.7 %
0.35-ZM	6,164	384,621	6,181	385,152	383,507	42.7 %
0.40-A	6,383	391,408	6,394	391,745	388,176	91.1 %
0.40-ZM	6,386	391,487	6,402	391,981	395,806	-97.6 %

where r_T is calculated using the following relation:

$$r_T = r_{vm}\left[1 - \frac{1}{2}\left(\frac{T}{\sigma_T}\right)^2 \pm \frac{T}{\sigma_T}\sqrt{1 - \frac{3}{4}\left(\frac{T}{\sigma_T}\right)^2}\right]. \tag{3.6}$$

K_I^{disp} is used to calculate the extent of transformation through the following approaches: von Mises equivalent $r_{vm} = \frac{1}{2\pi}\left(\frac{K}{\sigma_y}\right)^2$, Irwin's method $r_{irwin} = \frac{1}{\pi}\left(\frac{K}{\sigma_y}\right)^2$, Dugdale's method $r_{dugdale} = \frac{1}{8}\left(\frac{K}{\sigma_y}\right)^2$, and considering T-stresses in the equivalent stress equation as it is given in Equation 3.6. Figure 3.17 shows that as the displacement load increases r_T curve yields results closer to results of FEA performed using ZM model, r_{FE}.

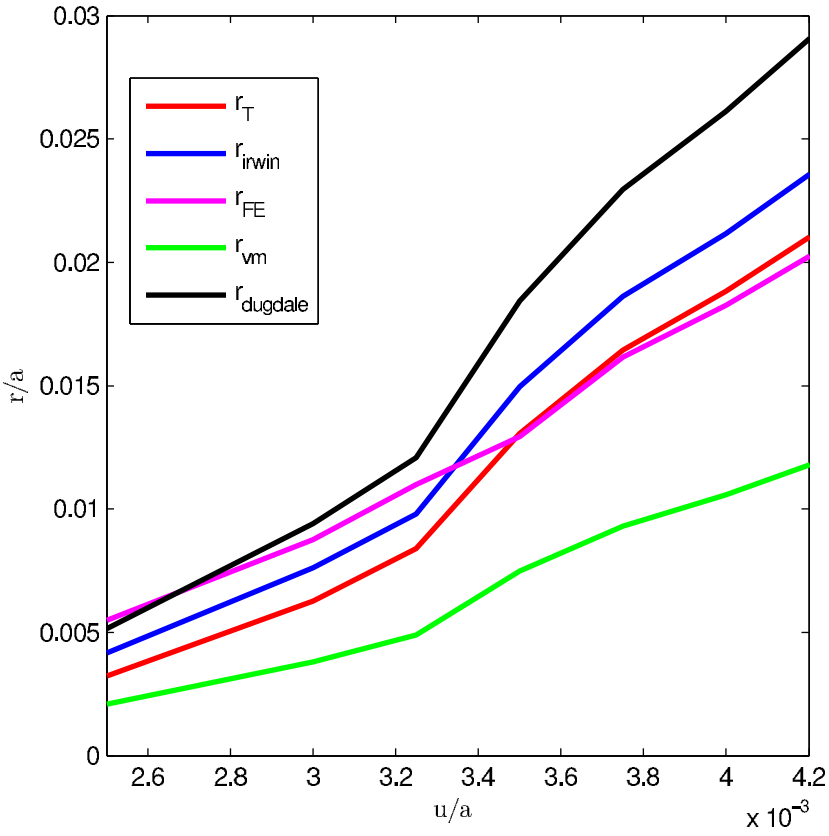


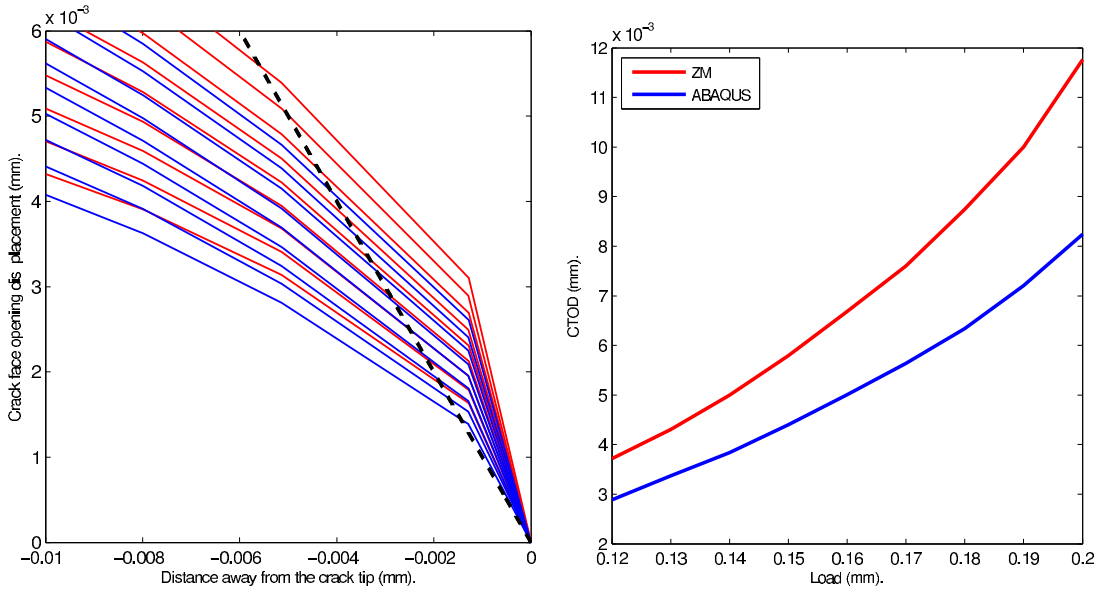
Figure 3.17. Comparison of the extent of transformation region r ($\theta = 0$) normalized by crack length a calculated using different methods.

3.3.6. Crack Tip Opening Displacement

For an elastic-plastic material the relationship between the crack tip opening displacement δ and J-integral has been formulated as [154]:

$$\delta = d_n \frac{J}{\sigma_o}, \tag{3.7}$$

where d_n is a material specific parameter independent of crack configuration, σ_o is taken as the average transformation stress. As it is represented in Figure 3.18, d_n is calculated using CTODs measured at the intersection of the 45^0 line drawn from the crack tip as it is defined by Shih [154], and crack tip J-integrals obtained from FE. Figure 3.19 shows that d_n converges to a constant value when the load increases which is also observed in the case of elastic–plastic materials [154–156].



a b

Figure 3.18. (a) Crack face opening profiles for increasing u. Half of the CTOD is measured from the intercept of 45^o line (dashed line starting from the crack tip) and the crack profile (b) CTOD values.

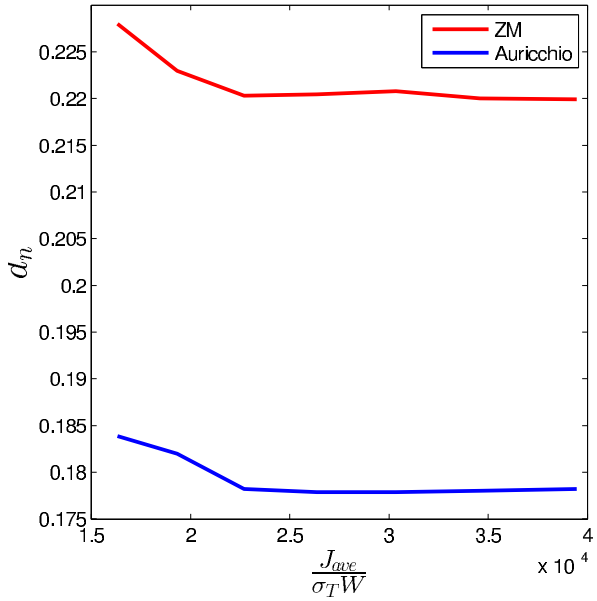


Figure 3.19. d_n values.

3.4. Crack Initiation and Stability of Crack Growth

In a cracked NiTi specimen the crack initiation will occur and propagation starts when the energy release rate, G, is equal to the fracture resistance, G_R at the crack tip. At this point crack propagates in stable or unstable manner depending on material

properties, loading, and testing conditions. In a stable crack growth the energy release rate is constant after it reaches G_R, G=G_R. In this study under the displacement load of $u = 0.1$ crack is assumed to be at the critical state to start to propagate.

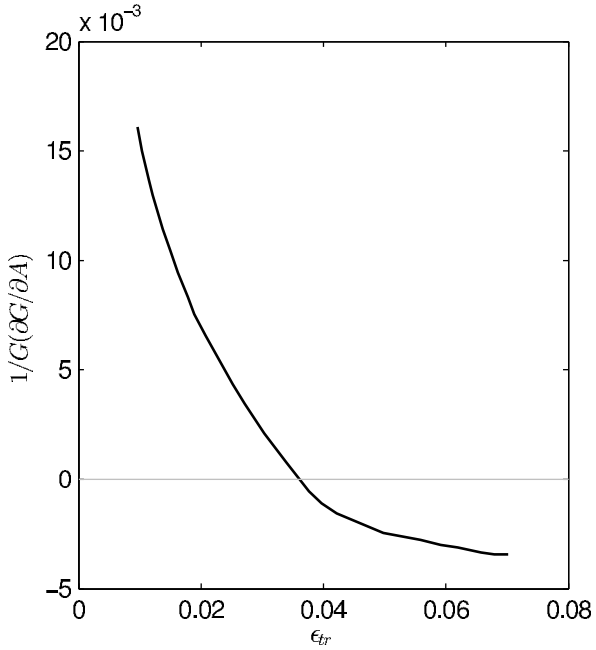


Figure 3.20. Effect or transformation strain on crack growth stability.

To check the crack stability and the parameters effecting the stability of crack growth the criterion, proposed by Woo and Chow [157] is used. Woo and Chow's criterion uses the virtual crack extension (VCE) technique presented by Parks [158] and Hellen [159]. In this method, under fixed displacement, the crack is allowed to grow by an infinitesimally small amount in two steps. In the first increment the energy release rate and in the second one the change of energy release rate with respect to incremental crack length is calculated [157].

$$\frac{1}{G_R}\frac{dG_R}{dA} \geq \frac{1}{G}(\frac{\partial G}{\partial A})_V. \tag{3.8}$$

In Equation 3.8 given above, G_R is the critical energy release rate value, in a stable crack growth is constant during crack growth. Therefore the negativity of the term, $(\frac{\partial G}{\partial A})_V$ which is the change of energy release rate under constant displacement, ensures the stability of the crack growth.

Figure 3.20, represents the change of the stability criterion with respect to the change of transformation strain, ϵ_{tr}. When $u = 0.1\ mm$ and $\epsilon_{tr} = 0.04$ $(\frac{\partial G}{\partial A})_V$ is negative, the dissipation of energy during phase transformation provides a stable crack growth. As shown in Figure 3.20, when $\epsilon_{tr} > 0.038$ and $u = 0.1\ mm$, it is possible to observe a stable crack growth.

3.5. Fracture Toughness

Most of the studies in literature note that phase transformation reduces crack tip SIF and increases toughness [14, 22, 30, 36, 41, 51, 160–163]. The increase in toughness is estimated from crack tip SIF change induced by phase transformation. According to McMeeking and Evans [12], if a particle undergoes a stress- induced martensitic transformation, then the enhanced toughness is due to residual strain field that restricts crack opening.

In contrast to these studies, some researchers [28, 164, 165] claim that phase transformation leads to volume contraction at the crack tip and thus SIF increases and toughness decreases. Xiong and Liu [39] studied thermally induced fracture in Ni–Mn–Ga, NiTi, and Cu–Al–Ni and found out that stress redistribution occurs around the crack tip, which leads to an increase in crack tip SIF and a decrease in fracture toughness. In addition to these, FE analysis of Yan *et al.* [24] on quasi-static crack growth in SMAs showed that volume contraction as a result of phase transformation reduces the toughness.

In literature authors published different volume contraction values for SMAs; Holtz *et al.* [166] measured -0.39% and Jackson [167] reported -0.54%. Robertson [168] calculated -0.39% change in volume contraction using synchrotron diffraction data given by Mehta *et al.* [165]. In Auricchio's model, the parameter ε_V, represents the volumetric strain. In this section to study the effects of change in volumetric strain, using the model represented in 3.2 and the material properties given in Table 3.2, the volumetric transformation strain is set to -2% and 2% respectively and SIFs calculated are tabulated in Table 3.4. The results in Table 3.4 show that, in this finite element

calculation the volumetric transformation strain has a little effect on results in SIF. There is a tendency of SIF to increase when the volumetric transformation strain is negative and a tendency to decrease if it is positive. But still the effect of volumetric strain is not very clear because the differences between SIF values are very small.

Table 3.4. K_I^G, determined Effect of volumetric strain on toughness.

a/W	$\varepsilon_V = 0$ %	$\varepsilon_V = 2$ %	$\varepsilon_V = -2$ %
0.20	326,626	325.891	327.316
0.25	352,987	350.135	353.949
0.30	371,633	370.966	373.400
0.35	384,236	382.125	385.497
0.40	391,745	389.918	393.141

Under Mode I loading, Wang [31] calculated stress distribution around the tip of an edge-cracked NiTi plate and in a similar linear elastic material with material properties identical to NiTi in the martensitic phase. He showed that martensite transformation suspends crack nucleation and propagation at the tip, and increases toughness. In this section, an edge-cracked NiTi plate and a linear elastic material with material properties identical to NiTi in the austenitic phase is compared under Mode I loading using material properties tabulated in Table 3.1. The geometry and boundary conditions of the plate are given in Figure 3.2 and approximate energy release rates are calculated using $\frac{\Delta U}{\Delta A}$ for different crack lengths. SIFs that were calculated for NiTi previously (K_G and K_{disp}) are normalized with SIFs of austenite plate (K_{aus}) and plotted in Figure 3.15. The SIFs are also tabulated in Table 3.5. The results show that K_{aus} is higher than K_G and K_{disp}. These results provide support for the claim that phase transformation decreases SIF and therefore increases fracture toughness.

T-stress values are also calculated upon increasing the displacement and plotted in Figure 3.21. It is known that negative T-stresses increases fracture toughness in elastic–plastic materials [169, 170], and Equation 3.6 showed that negative value of T-stresses increases phase transformation region and therefore this possibly results in

Table 3.5. Comparison of SIFs calculated using Auricchio and ZM models to the SIFs of homogeneous plate.

a/W	**Auricchio's model**		**ZM Model**		**Austenite**	
	K_I^{disp}	K_I^G	K_I^{disp}	K_I^G	K_I^{disp}	K_I^G
0.20	326,626	320,330	331,333	334,477	521,016	543,742
0.25	352,987	341,684	356,534	355,108	563,371	589,415
0.30	358.972	371.633	370.984	373.848	598.584	616.010
0.35	384,236	373,337	385,152	383,507	614,106	632,732
0.40	391,745	388,176	391,981	395,806	626,868	640,744

an increase in toughness.

The crack stability analysis showed us that increasing the transformation strain, increases the stability of the crack growth, and that can be used as parameter to control the fracture toughness.

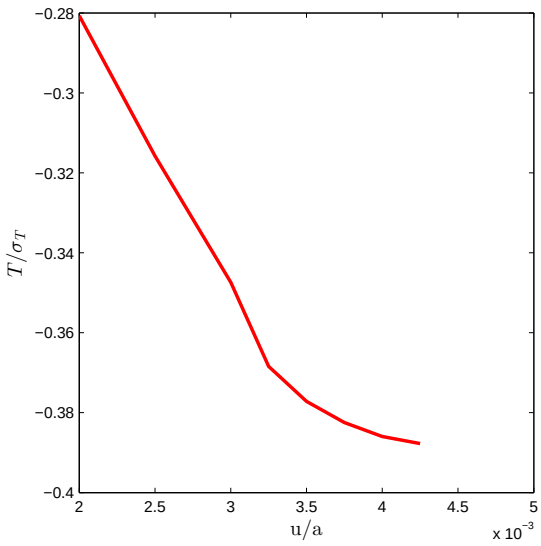


Figure 3.21. T-stresses normalized with the average transformation stress (σ_T) vs. applied displacement u/a (a/W =0.40).

Experimentally, it is easier to measure CTODs than J-integrals, especially when the crack grows [156]. Hellmann and Schwalbe [171] stated that resistance curve based

on CTOD gives a better estimate of the critical crack length compared to J-integral resistance curves. Therefore, for shape memory alloys, it is worth to investigate the relation between J-integral and CTOD. The crack face opening displacements calculated using ZM model is compared with that calculated using Auricchio's model and plotted in Figure 3.22. As presented in Figure 3.22, CFODs calculated using ZM model are higher. This result is in agreement with the previous finding given in Figure 3.12, which shows that less energy is dissipated through phase transformation when the ZM model is used in the analysis, implying that fracture toughness increases as a result of phase transformation.

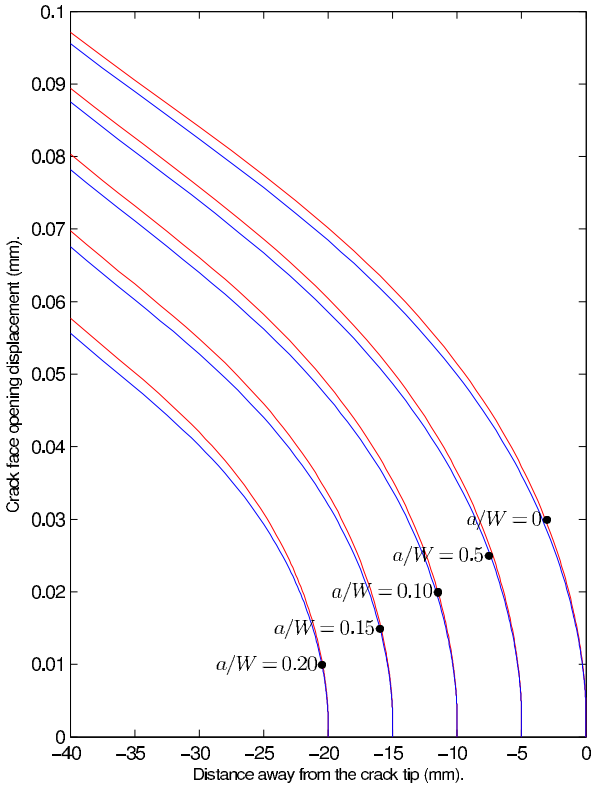


Figure 3.22. Crack face opening profiles for different a/W, $u = 0.10\ mm$. Red curves represents ZM model and the blue curves are those out of Auricchio's model.

3.6. Summary and Conclusions

In this chapter, to understand the effect of phase transformation on fracture behavior of NiTi, fracture mechanics properties such as J-integrals, energy release rates, stress intensity factors, crack opening displacements, and change in fracture toughness due to phase transformation are discussed. As it was stated in the previous studies

[48, 50, 52, 163], in SMAs, fraction of plastic dissipation around crack tip is very small compared to the energy dissipated through phase transformation. For this reason in this study, small-scale phase transformation without plastic deformation is taken into account around the crack tip.

The FE analysis reveals that the extent of the full martensite region calculated using ZM model is closer to region measured experimentally by Robertson *et al.* [35]. Auricchio's model predicts a larger, kidney–shaped full martensite region compared to ZM model as shown in Figure 3.9.

When ZM model is used in FE analyses, lower phase transformation energy and smaller phase transformation region are calculated than those of Auricchio's model. Energy release rates obtained using Auricchio's model are lower than those calculated using ZM model and as a result smaller SIFs are calculated using Auricchio's model. Using the SIFs obtained from energy calculations, the size of the martensite zone is calculated analytically employing square root singular stress equations in the K dominant zone. SIFs calculated using energy release rates give close results to those calculated from asymptotic near-tip opening displacement field equations. Therefore in SMAs, which undergo small-scale transformation around the tip, $\frac{\Delta U}{\Delta A}$ can be used to predict SIFs and thus energy release rate can be used as a parameter to interpret the fracture toughness change in SMAs. The defined stress deviation decreases in the fully transformed martensitic region, which shows the validity of asymptotic stress equations in that region. SIFs are calculated using superelastic SMA plate is lower than that for fully austenite homogeneous plate and this implies that toughness increases via phase transformation. Comparison of K_G and K_{disp} values showed that ZM model yields closer SIF compared to Auricchio's model.

It is found that negative T-stresses around the crack tip increase the extent of plastic region that is evaluated using equivalent stress and this gives results closer to FE results. Figure 3.17 shows that T-stresses should be included in the equations to determine the extent of phase transformation region accurately.

In this study, a linear relation is used between CTOD and J-integral similar to the case of elastic-plastic materials represented by Shih [154]. In addition to this, different d_n values calculated using ZM and Auricchio's models showed that d_n is a specific material parameter for SMAs and depends on the amount of phase transformation.

When the effect of volumetric transformation strain on toughness was considered, to get net conclusion was not possible because the FE results obtained indicated that the volume contraction had a little effect on SIF.

Summing up, comparison of CFOD, CTODs, SIFs, and dissipated energies using ZM and Auricchio's models show that SIF decreases due to phase transformation and increases resistance to crack propagation in SMAs. SIFs can more easily be predicted using $^{\Delta U}/_{\Delta A}$ for G. K dominance study showed that least squares fit of asymptotic equations gives reasonable prediction of SIFs. But the results of the extent of transformation region showed that the effect of T-stress should be taken into account in fracture parameters calculations. Different d_n values calculated using the two material models showed that an accurate determination of phase transformation region around the crack tip is necessary to obtain a correct relation between CTOD and J-integral. A good agreement of transformation regions calculated using ZM model and measured experimentally by Robertson *et al.* [35] is obtained in chapter 2. Future studies should involve experiments to verify the methods proposed in this work to find CTOD, SIFs, and phase transformation region around crack tip in SMAs.

4. MODELING OF STEADY-STATE CRACK GROWTH IN SHAPE MEMORY ALLOYS USING A STATIONARY METHOD

The detailed discussion about the fracture mechanics parameters in shape memory alloys represented in previous chapter has demonstrated the importance of the accurate determination of the phase transformation region around the tips of a static crack in SMAs. When the crack advances, martensite transformation occurs at the tip and the energy that goes into this transformation results in stable crack growth like in the case of plastic deformation.

Among the published studies on fracture mechanics properties of ductile materials and materials undergoing phase transformation, steady-state crack growth is one of the very frequently investigated subjects. Most of the studies related to crack growth deal with steady- state growth of a crack in perfectly plastic materials and quasi-static crack growth in materials undergoing phase transformation. None of these studies uses non-local stationary methods and they do not take into account reorientation of martensite phase to analyze steady-state growth of a crack in SMAs.

In literature, steady-state crack growth in elasto-plastic materials with small-scale yielding at the crack tip has been successfully modeled using stationary methods. In this work, Mode I steady-state crack growth in an edge-cracked Nitinol plate is modeled using a non-local stationary method [117]. The Zaki-Moumni constitutive model is utilized for this purpose. The model is implemented in Abaqus by means of a user-defined material subroutine to determine transformation zones around the crack tip. Steady-state crack growth is first simulated without considering reverse transformation to calculate the effect of transformation on stress distribution in the wake region, then reverse transformation is taken into account. The effect of reorientation of martensite near the crack tip as a result of non-proportional loading is also studied. The stress distribution and the phase transformation region are compared to results obtained for

the case of a static crack.

4.1. Introduction

In this work, a stationary method is used to analyze steady-state crack growth in an infinitely long edge-cracked thin plate to see the effect of transformation and martensite reorientation, considering a non-proportional loading history around crack tip. In literature, there are studies on steady-state crack growth in elasto-plastic materials that use non-local stationary methods. One of the first methods developed to analyze steady-state crack growth is presented by Dean and Hutchinson [172]. They integrated space-discrete elastic-plastic constitutive equation along the streamlines parallel to the crack plane in the plastic zone near crack tip, to calculate stresses during steady-state growth of a crack under Mode I and Mode III loading. They compared their numerical results to analytical results obtained by Rice *et al.* [173] and showed that they were in good agreement. Stahle [174] wrote a UMAT subroutine based on the algorithm given by Dean and Hutchinson [172] and used Abaqus to analyze Mode I steady-state crack growth in elasto-plastic materials. He computed the plastic zone around the crack tip and compared his results to results of a quasi-static crack growth. He found that steady-state method is advantageous from a computational point of view over quasi-static crack growth models that use a node release technique. The method developed by Dean and Hutchinson [172] was used by researchers studying steady-state crack growth in elastic-plastic materials joined by a laser weld [175], ferroelastic materials [176], ferroelectric materials [177, 178], adhesively bonded layers [179, 180] and rate sensitive materials [181, 182]. Sobotka and Dodds [183] extended the work of Dean and Hutchinson [172] and implemented the same technique to 3D to study steady crack growth in a thin elasto-plastic plate with small-scale yielding around the crack tip. Recently Baxevanis *et al.* [184] used the method of Dean and Hutchinson [172] to calculate crack tip energy release rate, G_{tip}, for a crack growing in steady-state in a pseudo-elastic SMA specimen under Mode I loading. They found that reverse phase transformation in the wake region of a growing crack increases toughness.

Nguyen and Rahimian [185] proposed a steady-state (stationary) method to compute stress and strain distribution around the tip of a steady-state growing crack in an elastic-perfectly plastic infinite strip under Mode I loading and they stated that using stationary method gives theoretically more satisfying results when compared to node release technique. In the study of Nguyen and Rahimian [185], dissipative variables are updated everywhere in the model without the need to predict the size of inelastic region. On the other hand, to use the methodology proposed by Dean and Hutchinson [172] in an inelastic medium, one has to calculate inelastic zone height to construct streamlines for integration. For this reason method used by Nguyen and Rahimian [185] is more general and not limited only to solve steady-state crack growth problems but also can be used for elastic-plastic analysis of structures subjected to repeated loads moving in steady-state [186, 187] where it is difficult to predict the size of inelastic zone. Lê Minh *et al.* [188] extended the stationary method proposed by Nguyen and Rahimian [185] to analyse fatigue crack propagation and plasticity induced crack closure in a stainless steel specimen. For shape memory alloys however, except Moumni [117] who modeled stationary growth in a material undergoing phase transformation without considering reverse transformation, most studies assume quasi-static growth.

In the wake region of a steadily growing crack reverse transformation occurs and that may affect toughening due to phase transformation around the crack tip. Stam and van der Giessen [14] studied the effect of partial or full reversibility of stress-induced phase transformation around the crack tip on toughness assuming quasi-static crack growth in SMAs and zirconia ceramics using finite elements with the constitutive model of Sun *et al.* [189]. They concluded that phase transformation leads to toughening of the SMA and if the material is showing a superelastic behavior where reverse transformation occurs upon unloading, the toughness enhancement as a result of phase transformation is less. Yan *et al.* [24] studied a quasi-statically growing crack using finite elements to see the effect of stress-induced martensite transformation on fracture behavior of superelastic SMAs and compared their results to those obtained in the case of phase transformation in zirconia ceramics. They assumed a partial reverse transformation in the wake region and stated that the effect of reverse transformation in the wake region is negligible. Freed and Banks-Sills [41] presented a finite element study

on transformation toughening behavior of a slowly propagating crack using a cohesive zone model in an SMA under Mode I loading and plane strain conditions assuming small-scale transformation zone around crack tip. They found that reversible phase transformation reduces the amount of toughening in the alloy. Gollerthan *et al.* [190] made measurements during loading and unloading of a NiTi compact tension specimen under Mode I loading using infrared thermography and showed that martensite transformation occurs around crack tip during crack growth and reverse transformation occurs in crack wake region. Baxevanis *et al.* [163] studied Mode I quasi-static crack growth in SMAs under plane strain condition using finite elements considering only forward transformation and they calculated energy release rate using virtual crack closure technique. They found out that plastic dissipation is small compared to energy dissipated due to phase transformation therefore plastic deformation can be neglected during steady-state crack growth analysis in SMAs. Even though numerical simulations in the study of Stam and van der Giessen [14], Yi and Gao [22], Yan *et al.* [24], Freed and Banks-Sills [41] and Baxevanis *et al.* [163] predict the presence of residual martensite in the crack wake region, experimental work of Gollerthan *et al.* [190] and Robertson *et al.* [35] shows that as the crack grows, the martensite that has formed around the tip transforms back to austenite.

When loaded superelastically above orientation finish stress σ^f, martensite that forms will be fully oriented. If loading is then increased proportionally, orientation of martensite will not change. On the other hand, non-proportional loading leads to the formation of different martensite variants, resulting in a change in the orientation strain. Some experimental studies show that martensite reorientation is intimately related to non-proportional loading [191, 192]. To be able to simulate problems involving non-proportional loading accurately, reorientation of martensite variants is considered in latest SMA models [e.g. 2, 83, 102, 118–121, 193–198]. Zaki [199, 200] proposed an efficient numerical method to calculate evolution of orientation strain by introducing two different set of yield functions and validated his results with experimental data. In recent studies, micro-level modelling and different phase field theories are used to investigate reorientation of martensite, variant and dislocation formation in SMAs [201–204].

In fracture mechanics it is known that a material point close to crack tip experiences non-proportional loading during crack growth [172, 205, 206]. Yi and Gao [22] investigated fracture toughening of shape memory alloys using the constitutive model of Sun and Hwang [15], considering non-proportional loading for forward and reverse transformation. They obtained an analytical solution for the determination of the transformation region around cracks advancing in steady-state. In the wake region they assumed that there was no reverse transformation and they stated that when the crack advances, the shape of the transformation zone changes with a long transformed wake. Landis [176] investigated strain reorientation near a propagating crack tip in ferroelastic materials that occurs due to non-proportional loading. He stated that when the crack propagates, the crack tip loads and unloads non-proportionally causing reorientation of transformation strain and resulting in increase of external energy necessary for the crack to grow. Results of X-ray diffraction experiments done by Young *et al.* [143] to identify transformation regions, textures and lattice strains in front of a crack tip show that during crack growth martensite phase with different orientations are observed in the transformation region near the crack tip. The experimental analysis done by McKelvey and Ritchie[207] revealed that phase transformation was suppressed during fatigue crack growth by the hydrostatic state of stress ahead of the crack tip for plane strain conditions. Whereas, in the case of plane stress, it is observed from the transmission electron microscopy images taken from the crack tip that pseudo-elastic martensitic transformation takes place. The main reason of this behavior is stated as the lack of hydrostatic stress state at crack tip for plane stress condition under fatigue crack growth.

None of the work above uses a complete non-local stationary method and none of them considers orientation of martensite variants around the crack tip. In this work, the dissipative variables are updated everywhere in the model using space-discrete consistency conditions, and the incremental consistency equations are written in terms of finite differences as presented by Nguyen and Rahimian [185].

The aim of this work is to study the effect of reorientation on phase transformation during steady-state crack growth. Crack growing without reverse transformation and

static crack are also studied for comparison purposes to see the effect of steady-state crack growth and reverse transformation on stress distribution and phase transformation. In the first part of the paper the evolution of transformation and the effect of reorientation is addressed. In the next part the solution methodology using stationary approach is represented and phase transformation regions, stresses around the crack tip, crack face opening displacements and J-integrals are calculated. Finally discussion on the results comparing four different cases simulated under plane stress and plane strain conditions is made.

4.2. Problem Statement

Consider a crack in an infinitely long, thin SMA plate of fixed height $2h$. The crack is located at equal distance from the upper and lower borders and is assumed to grow in steady-state with a speed l along the x-axis as shown in Figure 4.1. The plate is subjected to loading in the vertical direction along the upper and lower borders. The applied load is assumed to move with the same velocity as the crack tip in the x direction such that the load is constantly 0 for $x < -c$ and non-zero for $x \geq -c$, where c is some constant finite length. For simplicity, the analytical derivations and subsequent numerical results are obtained under the assumption of small strains. The case of finite strain is briefly discussed in the conclusion as a prospect of the present work.

Because of the applied load, phase transformation from austenite to martensite occurs at the crack tip. The evolution of the martensite transformation at a material point can be written as follows:

$$\frac{D\zeta}{Dt} = \frac{\partial \zeta}{\partial t} + \boldsymbol{v} \cdot \nabla \zeta, \tag{4.1}$$

where ζ is martensite volume fraction and $\boldsymbol{v}$ is the velocity of the material point with respect to coordinate frame attached to crack tip (see Figure 4.1).

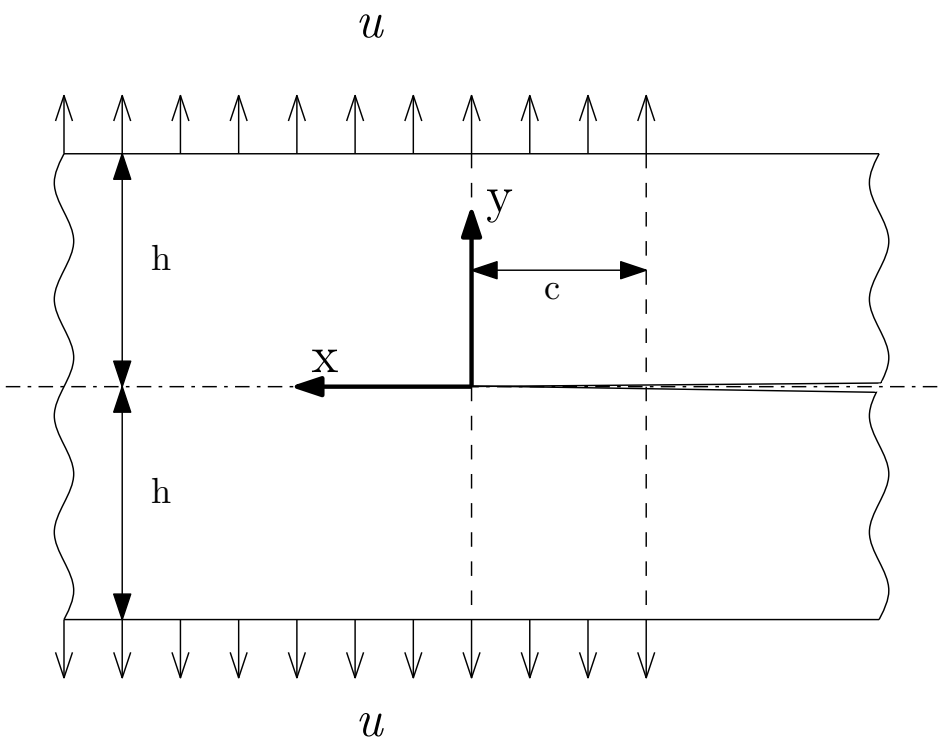


Figure 4.1. Crack growth in an infinitely long plate.

Under steady-state conditions, equation Equation 4.1 simplifies to:

$$\dot{\zeta} = -l\zeta_{,x}. \tag{4.2}$$

where ‘,x ’ represents the partial derivative with respect to x. Similarly, the steady-state evolution of the stress, strain and orientation strain can be written as shown below:

$$\dot{\sigma}_{ij} = -l\sigma_{ij,x}, \tag{4.3}$$

$$\dot{\varepsilon}_{ij} = -l\varepsilon_{ij,x}, \tag{4.4}$$

$$\dot{\varepsilon}^{ori}_{ij} = -l\varepsilon^{ori}_{ij,x}, \tag{4.5}$$

ε_{ij} can be written as the sum of two individual phase strains as follows :

$$\varepsilon_{ij} = (1-\zeta)\varepsilon_{ij}^{A} + \zeta\varepsilon_{ij}^{M}, \tag{4.6}$$

where ε_{ij}^{A} and ε_{ij}^{M} are the local strains of austenite and martensite respectively. Moreover, assuming additive decomposition of the total strain ε_{ij} into an elastic strain ε_{ij}^{el} and a transformation strain ε_{ij}^{tr},

$$\varepsilon_{ij} = \varepsilon_{ij}^{el} + \varepsilon_{ij}^{tr}. \tag{4.7}$$

Following Zaki and Moumni [2], the transformation strain is written as:

$$\varepsilon_{ij}^{tr} = \zeta\varepsilon_{ij}^{ori}. \tag{4.8}$$

When the martensite transformation start stress σ^{ms} is higher than the orientation finish stress σ^{f}, $\sigma^{ms} > \sigma^{f}$, austenite transforms directly into oriented martensite [208], and the stress-strain relation is defined as [2]:

$$\sigma_{ij} = E_{ijkl}\left(\varepsilon_{kl} - \zeta\varepsilon_{kl}^{ori}\right). \tag{4.9}$$

By evaluating the material derivative of Equation 4.9, one gets:

$$\dot{\sigma}_{ij} = E_{ijkl}\left(\dot{\varepsilon}_{kl} - \dot{S}_{mnkl}\sigma_{mn} - \dot{\zeta}\varepsilon_{kl}^{ori} - \zeta\dot{\varepsilon}_{kl}^{ori}\right) \tag{4.10}$$

where S_{ijkl} is the compliance tensor given by:

$$S_{ijkl} = (1-\zeta)S_{ijkl}^{\mathrm{A}} + \zeta S_{ijkl}^{\mathrm{M}} \quad , \tag{4.11}$$

S_{ijkl}^{A} and S_{ijkl}^{M} are the compliance tensors for austenite and martensite respectively.

Equations (4.2),(4.3),(4.4) and (4.5) can be substituted into equation Equation 4.10 to get the change of stress along x:

$$\sigma_{ij,x} = E_{ijkl}\left(\varepsilon_{kl,x} - \left[(S^{\mathrm{M}}_{mnkl} - S^{\mathrm{A}}_{mnkl})\zeta_{,x}\right]\sigma_{mn} - \zeta_{,x}\varepsilon^{ori}_{kl} - \zeta\varepsilon^{ori}_{kl,x}\right). \tag{4.12}$$

The evolution of ζ is obtained by enforcing consistency with the phase transformation conditions governed by the following loading functions:

$$\begin{aligned} F_{\zeta 1} = &\left\{\frac{1}{3}El_{\mathrm{MA}}\sigma^2_{\mathrm{VM}} + \frac{1}{2}\left(\frac{1}{3}El_{\mathrm{MA}} + P_{\mathrm{MA}}\right){\sigma_{ii}}^2 - C(T)\right\} \\ &+ \sigma_{ij}\varepsilon^{ori}_{ij} - (G+b)\zeta - a(1-\zeta) - \left[(\alpha-\beta)\zeta + \frac{\beta}{2}\right]\left(\frac{2}{3}\varepsilon^{ori}_{ij}\varepsilon^{ori}_{ij}\right), \end{aligned} \tag{4.13}$$

for forward transformation, and

$$\begin{aligned} F_{\zeta 2} = &-\left\{\frac{1}{3}El_{\mathrm{MA}}\sigma^2_{\mathrm{VM}} + \frac{1}{2}\left(\frac{1}{3}El_{\mathrm{MA}} + P_{\mathrm{MA}}\right){\sigma_{ii}}^2 - C(T)\right\} \\ &- \sigma_{ij}\varepsilon^{ori}_{ij} + (G-b)\zeta - a(1-\zeta) + \left[(\alpha-\beta)\zeta + \frac{\beta}{2}\right]\left(\frac{2}{3}\varepsilon^{ori}_{ij}\varepsilon^{ori}_{ij}\right), \end{aligned} \tag{4.14}$$

for reverse transformation where σ_{VM} is the von Mises stress and

$$El_{MA} = \frac{1+\nu}{E_M} - \frac{1+\nu}{E_A} \quad , \quad P_{MA} = \frac{\nu}{E_A} - \frac{\nu}{E_M}, \tag{4.15}$$

ν being Poisson's coefficient for the material.

In the equations above, β influences martensite orientation during phase change, G is responsible for orientation-independent interaction between martensite variants, α controls the slope of the stress-strain curve corresponding to martensite orientation, a and b control the width of the hysteresis of stress-strain curve during transformation and $C(T)$ is an energy density that depends on temperature [2]. If $F_{\zeta 1} < 0$ and $F_{\zeta 2} < 0$, no phase change occurs. In the case of forward transformation, $F_{\zeta 1} = 0$ and $\dot{F}_{\zeta 1} = 0$, whereas for reverse transformation $F_{\zeta 2} = 0$ and $\dot{F}_{\zeta 2} = 0$.

Reorientation is governed by the function:

$$F_{ori} = X_{VM} - \zeta Y, \tag{4.16}$$

where X_{VM} is the von Mises equivalent of the thermodynamic force X_{ij} defined as:

$$X_{ij} = \sigma^d_{ij} - \frac{2}{3(\varepsilon_0)^2}\sigma^d_{kl}\varepsilon^{ori}_{kl}\varepsilon^{ori}_{ij}, \tag{4.17}$$

where

$$\varepsilon_0 = \sqrt{\frac{2}{3}\varepsilon^{ori}_{ij}\varepsilon^{ori}_{ij}} \tag{4.18}$$

and σ^d_{ij} is the stress deviator. Y is the stress threshold that corresponds to transformation from self-accommodated martensite to oriented martensite at the beginning of orientation. When there is no orientation of martensite, $F_{ori} < 0$ whereas in the case of orientation, $F_{ori} = 0$.

ε^{ori}_{ij} evolves in a direction normal to the tangent to the loading surface defined by $F_{ori} = 0$. The normality rule is written as:

$$\dot{\varepsilon}^{ori}_{ij} = \frac{3}{2}\dot{\eta}\frac{X_{ij}}{X_{VM}}, \tag{4.19}$$

where $\dot{\eta} \geq 0$, $F_{ori} \leq 0$ and $\dot{\eta}F_{ori} = 0$.

At the very early stages of transformation, at a material point near the crack tip, $\zeta = 0^+$ and $F_{ori} = 0$ therefore Equation 4.16 requires $X_{VM} = 0$. From Equation 4.17, the orientation of the transformation strain tensor has to be equal to the orientation of the deviatoric stress tensor. When loading around the crack tip is assumed to be proportional during phase transformation, the orientation of martensite does not change ($\dot{\eta} = 0$). For proportional loading, the orientation strain tensor can therefore

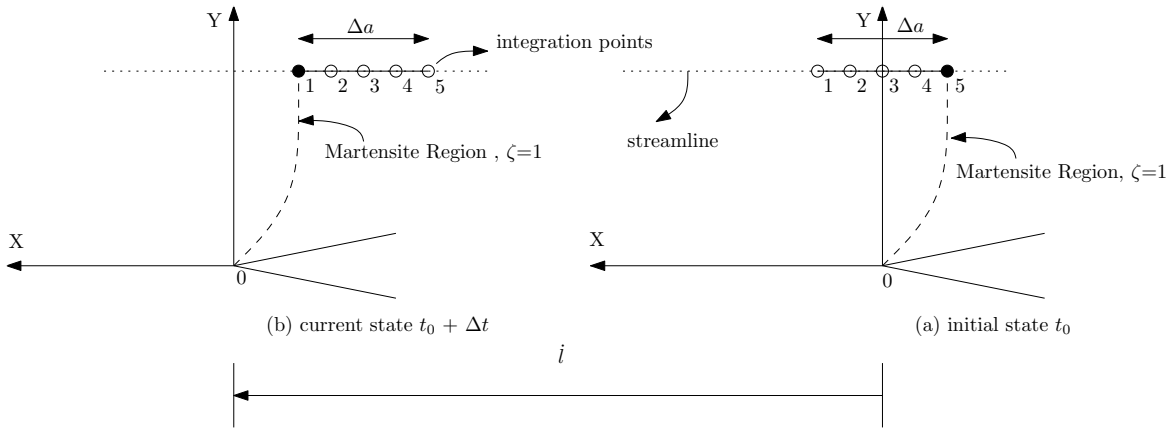


Figure 4.2. Schematical representation of solution methodology.

be written as:

$$\varepsilon_{ij}^{ori} = \frac{3}{2}\varepsilon_o \frac{\sigma_{ij}^d}{\sigma_{VM}}. \tag{4.20}$$

4.3. Solution Methodology

In this work to obtain transformation region and stresses around the tip of the steadily growing crack represented in Figure 4.1, permanent movement method proposed by Nguyen and Rahimian [185] is employed using FE. In this method, according to an observer attached to the tip of a crack growing with a constant speed l, martensite phase contours at time t_0 and $t_0 + \Delta t$ in the neighborhood of the crack tip are the same and mesh moves in the direction opposite to the crack growth as it is represented schematically in Figure 4.2. In this study, $u = 0.055\ mm$ is taken at the boundary for which full martensitic transformation occurs at the crack tip, and convergence of the solution algorithm is ensured. The problem is then solved assuming a stable crack growth. In the works of Yan *et al.* [24], Budiansky *et al.* [209] and Nguyen and Rahimian [185], similarly a stable crack growth assumption is used without checking any specific K_C value.

A finite element model is created as shown in Figure 4.3, where only the upper half of the plate is meshed using symmetry. A rectangular mesh with second order plane

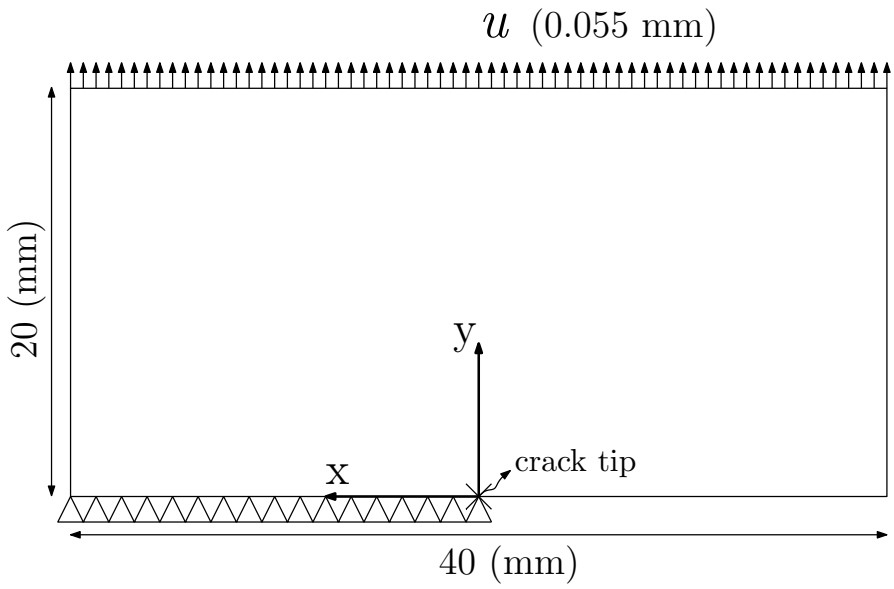


Figure 4.3. Finite element model.

stress elements and reduced integration points (CPS8R) is used (Figure 4.4). Since the mesh is rectangular, streamlines parallel to x-axis connecting the integration points are drawn along which gradients are calculated. Figure 4.5 shows the numbering of the integration points, which increases from left to right and bottom to top. In the UMAT subroutine written in Fortran a data structure is used to store the data processed at an integration point.

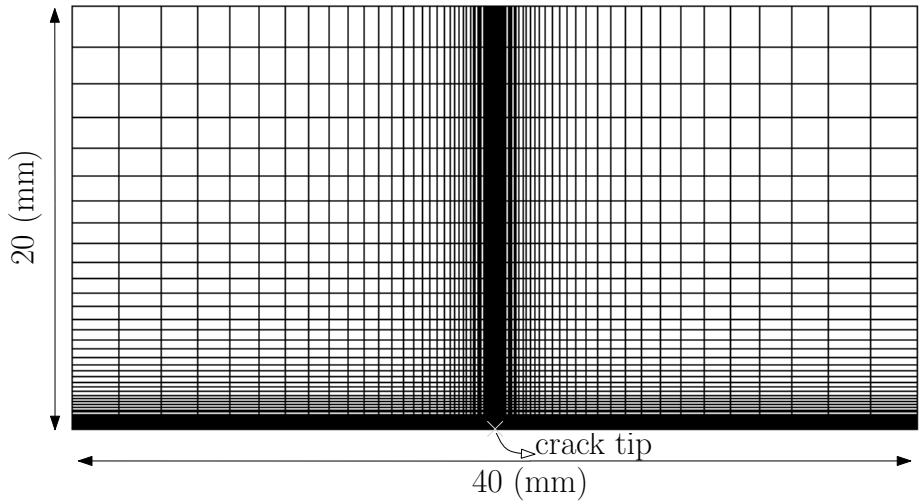


Figure 4.4. Finite element mesh.

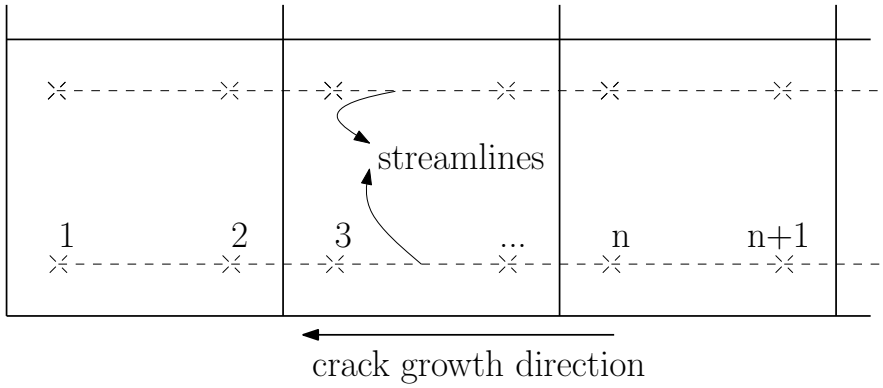


Figure 4.5. Integration point numbering.

The gradient used in Equation 4.2 is evaluated at integration point $n+1$ as:

$$\zeta_{,x} \approx \frac{\Delta\zeta}{\Delta x} = \frac{[\zeta]_{n+1} - [\zeta]_n}{[x]_{n+1} - [x]_n}, \tag{4.21}$$

where n is the number of the previous integration point. Similarly,

$$\sigma_{ij,x} \approx \frac{\Delta\sigma_{ij}}{\Delta x} = \frac{[\sigma_{ij}]_{n+1} - [\sigma_{ij}]_n}{[x]_{n+1} - [x]_n}, \tag{4.22}$$

$$\varepsilon_{ij,x} \approx \frac{\Delta\varepsilon_{ij}}{\Delta x} = \frac{[\varepsilon_{ij}]_{n+1} - [\varepsilon_{ij}]_n}{[x]_{n+1} - [x]_n}, \tag{4.23}$$

$$\varepsilon^{tr}_{ij,x} \approx \frac{\Delta\varepsilon^{tr}_{ij}}{\Delta x} = \frac{[\varepsilon^{tr}_{ij}]_{n+1} - [\varepsilon^{tr}_{ij}]_n}{[x]_{n+1} - [x]_n}. \tag{4.24}$$

Along a streamline, between integration points n and $n+1$, change in the stress σ_{ij}, can be evaluated as follows:

$$[\Delta\sigma_{ij}]^k = [E_{ijkl}]^{k-1}_{n+1}\{[\Delta\varepsilon_{ij}]^k - ([\Delta S_{ijkl}]^k[\sigma_{ij}]^{k-1}_{n+1} + [\Delta\zeta]^k[\varepsilon^{ori}_{ij}]^{k-1}_{n+1} + [\zeta]^{k-1}_{n+1}[\Delta\varepsilon^{ori}_{ij}]^k)\}, \tag{4.25}$$

where

$$[\Delta S_{ijkl}]^k = (S^{\mathrm{M}}_{ijkl} - S^{\mathrm{A}}_{ijkl})[\Delta\zeta]^k, \tag{4.26}$$

and k is the consistency iteration number.

The increments $\Delta\zeta$ and $\Delta\varepsilon^{ori}_{ij}$ satisfy the consistency conditions. They are determined by expanding and solving the equations $[F_\zeta]^k = 0$ and $[F_{ori}]^k = 0$ at integration point $n+1$ as follows:

$$\begin{aligned}[F_\zeta]^{k-1}_{n+1} + [F_{\zeta,\sigma_{ij}}]^{k-1}_{n+1} : [\Delta\sigma_{ij}]^k + [F_{\zeta,\zeta}]^{k-1}_{n+1}[\Delta\zeta]^k \\ +[F_{\zeta,\varepsilon^{ori}_{ij}}]^{k-1}_{n+1} : [\Delta\varepsilon^{ori}_{ij}]^k = 0\end{aligned} \tag{4.27}$$

and

$$\begin{aligned}[F_{ori}]^{k-1}_{n+1} + [F_{ori,\sigma_{ij}}]^{k-1}_{n+1} : [\Delta\sigma_{ij}]^k + [F_{ori,\zeta}]^{k-1}_{n+1}[\Delta\zeta]^k \\ +[F_{ori,\varepsilon^{ori}_{ij}}]^{k-1}_{n+1} : [\Delta\varepsilon^{ori}_{ij}]^k = 0.\end{aligned} \tag{4.28}$$

For simplicity, the derivatives of the transformation functions in the above equations are represented as follows:

$$\begin{aligned}\frac{\partial F_\zeta}{\partial\zeta} = F_{\zeta,\zeta}, \quad \frac{\partial F_\zeta}{\partial\sigma_{ij}} = F_{\zeta,\sigma_{ij}}, \quad \frac{\partial F_\zeta}{\partial\varepsilon^{ori}_{ij}} = F_{\zeta,\varepsilon^{ori}_{ij}}, \frac{\partial F_{ori}}{\partial\zeta} = F_{ori,\zeta}, \\ \frac{\partial F_{ori}}{\partial\sigma_{ij}} = F_{ori,\sigma_{ij}}, \frac{\partial F_{ori}}{\partial\varepsilon^{ori}_{ij}} = F_{ori,\varepsilon^{ori}_{ij}}.\end{aligned} \tag{4.29}$$

The normality rule, at integration point $n+1$ can be expressed in incremental form as follows:

$$[\Delta\varepsilon^{ori}_{ij}]^k = [\Delta\eta]^k[N_{ij}]^k_{n+1}, \tag{4.30}$$

where

$$[N_{ij}]^k = \frac{3}{2}\frac{[X_{ij}]^k_{n+1}}{[X_{VM}]^k_{n+1}}. \tag{4.31}$$

$\Delta\eta$ and $\Delta\zeta$ are calculated by solving Equation 4.27 and Equation 4.28 together with Equation 4.25, Equation 4.26 and Equation 4.30 to get:

$$\Delta\eta = \frac{B_\zeta C_\zeta - A_\zeta C_{ori}}{A_\zeta B_{ori} - B_\zeta A_{ori}}, \tag{4.32}$$

$$\Delta\zeta = -\frac{C_\zeta}{A_\zeta} - \frac{A_{ori}}{A_\zeta}\Delta\eta. \tag{4.33}$$

where

$$A_\zeta = [F_{\zeta,\zeta}]^{k-1}_{n+1} - [F_{\zeta,\sigma_{ij}}]^{k-1}_{n+1}[E_{ijkl}]^{k-1}_{n+1}\left\{(S^{\mathrm{M}}_{mnkl} - S^{\mathrm{A}}_{mnkl})[\sigma_{mn}]^{k-1}_{n+1} + [\varepsilon^{ori}_{kl}]^{k-1}_{n+1}\right\}, \tag{4.34}$$

$$A_{ori} = [F_{\zeta,\varepsilon^{ori}_{ij}}]^{k-1}_{n+1}[N_{ij}]^k_{n+1} - [\zeta]^{k-1}_{n+1}[F_{\zeta,\sigma_{ij}}]^{k-1}_{n+1}[E_{ijkl}]^{k-1}_{n+1}[N_{kl}]^k_{n+1}, \tag{4.35}$$

$$B_\zeta = [F_{ori,\zeta}]^{k-1}_{n+1} - [F_{ori,\sigma_{ij}}]^{k-1}_{n+1}[E_{ijkl}]^{k-1}_{n+1}\left\{(S^{\mathrm{M}}_{mnkl} - S^{\mathrm{A}}_{mnkl})[\sigma_{mn}]^{k-1}_{n+1} + [\varepsilon^{ori}_{kl}]^{k-1}_{n+1}\right\}, \tag{4.36}$$

$$B_{ori} = [F_{ori,\varepsilon^{ori}_{ij}}]^{k-1}_{n+1}[N_{ij}]^k_{n+1} - [\zeta]^{k-1}_{n+1}[F_{ori,\sigma_{ij}}]^{k-1}_{n+1}[E_{ijkl}]^{k-1}_{n+1}[N_{kl}]^k_{n+1}, \tag{4.37}$$

$$C_\zeta = [F_\zeta]^{k-1}_{n+1} + [F_{\zeta,\sigma_{ij}}]^{k-1}_{n+1}[E_{ijkl}]^{k-1}_{n+1}[\Delta\varepsilon_{kl}]^k, \tag{4.38}$$

$$C_{ori} = [F_{ori}]^{k-1}_{n+1} + [F_{ori,\sigma_{ij}}]^{k-1}_{n+1}[E_{ijkl}]^{k-1}_{n+1}[\Delta\varepsilon_{kl}]^k. \tag{4.39}$$

Table 4.1. Material model parameters.

Parameter	Value
E_{A}	61500 MPa
E_{M}	24000 MPa
a	6.89 MPa
b	6.91 MPa
G	4.66 MPa
α	2750 MPa
β	5500 MPa
Y	110 MPa
$C(T)$	15.64 MPa
ε_0	4 %
ν	0.3

In the case of proportional loading ($\Delta\eta = 0$), the increment of the martensite volume fraction becomes;

$$\Delta\zeta = -\frac{C_\zeta}{A_\zeta}. \tag{4.40}$$

The solution procedure is summarized as follows:

(i) Calculation starts from the first integration point, n=1 shown in Figure 4.5, where $\zeta = 0$ and $\eta = 0$.

(ii) The strain increment is taken from Abaqus and stresses are calculated at $n = 1$ using Equation 4.9.

(iii) The trial stress is calculated at the next integration point, $n = 2$, from Equation 4.9 assuming ζ and η are still equal to zero.

(iv) The transformation functions are checked from Equation 4.13, Equation 4.14 and Equation 4.16. If $F_{\zeta 1} > 0$ and $\zeta < 1$, forward transformation; $F_{\zeta 2} > 0$

and $\zeta > 0$, reverse transformation and $F_{ori} > 0$ orientation occurs. During phase transformation $\Delta\zeta$ (from Equation 4.33) and during orientation $\Delta\eta$ (from Equation 4.32) is calculated iteratively until the relevant consistency conditions are satisfied.

(v) Using $\Delta\zeta$ and $\Delta\eta$, ζ and ε_{ij}^{ori} are calculated from Equation 4.8, Equation 4.21 and Equation 4.24.

(vi) The equivalent elasticity tensor E_{ijkl} is updated and the stresses are calculated again from Equation 4.9 using the updated values of ζ and ε_{ij}^{ori}.

(vii) Calculation passes to the next integration point.

(viii) Abaqus checks the force equilibrium when the calculation is complete at all the integration points.

The above procedure is represented in Algorithm 1. Like in the case of proportional loading, if the orientation of martensite variants does not change ($\Delta\eta = 0$) there is no need to check the orientation function F_{ori}.

The solution methodology represented above is used to solve the steady-state crack growth problem represented in Figure 4.3. The half-plate is 40 mm wide and 20 mm high and the upper boundary is subjected to a uniform vertical displacement $u = 0.055$ mm in the positive y direction. The material parameters used for the simulations are listed in Table 4.1. Four different cases under Mode I loading are studied: (i) Reverse transformation from martensite to austenite is not allowed, (ii) Reverse transformation with reorientation is allowed, (iii) Reverse transformation is allowed without martensite reorientation (proportional loading), (iv) Static crack. The simulation in case IV does not use a stationary method, but rather a conventional time discrete incremental approach where the vertical displacement is increased incrementally from 0 to 0.055 mm and the state of the material is updated accordingly considering reverse transformation without reorientation. For steady-state growth in case II, the evolution of ε_{ij}^{ori} is formulated considering non-proportional loading near crack tip.

As a result of the analysis martensite region, stresses around the crack tip and crack face opening displacements are calculated using four different cases under plane

Initial Conditions $\zeta(+\infty) = 0$, $\varepsilon^{ori}(+\infty) = 0$.

(i) **Trial stress**

Set : $k = 0$, $\quad \zeta^0_{n+1} = \zeta^0_n$, $\quad [\varepsilon^{ori}_{ij}]^0_{n+1}$=$[\varepsilon^{ori}_{ij}]^0_n$

Calculate trial stress $[\sigma_{ij}]^0_{n+1}$=$[E_{ijkl}]^0_{n+1}$($[\varepsilon_{ijkl}]^0_{n+1}$-$[\zeta]^0_{n+1}[\varepsilon^{ori}_{ij}]^0_{n+1}$)

(ii) **Check transformation functions :** $F_{\zeta 1}$, $F_{\zeta 2}$, F_{ori}

if $F_{\zeta 1} > 0$ and $1 - \zeta > 0$ **then**
  Forward Transformation

if $F_{\zeta 2} > 0$ and $\zeta > 0$ **then**
  Reverse Transformation

if $F_{ori} > 0$ **then**
  Orientation

if Forward Transformation only **then**
  $[F_{\zeta 1}]^k_{n+1} = 0$ gives $\Delta\zeta$.

else if Forward Transformation and Orientation **then**
  $[F_{\zeta 1}]^k_{n+1} = 0$ and $[F_{ori}]^k_{n+1} = 0$ give $\Delta\zeta$ and $\Delta\eta$.

else if Reverse Transformation only **then**
  $[F_{\zeta 2}]^k_{n+1} = 0$ gives $\Delta\zeta$.

else if Reverse Transformation and Orientation **then**
  $[F_{\zeta 2}]^k_{n+1} = 0$ and $[F_{ori}]^k_{n+1} = 0$ give $\Delta\zeta$ and $\Delta\eta$.

else if Orientation only **then**
  $[F_{ori}]^k_{n+1} = 0$ gives $\Delta\eta$.

else
  Exit and go to step 6.

(iii) Update $[\zeta]^k_{n+1}$,$[\varepsilon^{ori}_{ij}]^k_{n+1}$ and $[E_{ijkl}]^k_{n+1}$.

(iv) Calculate stress using :

$[\sigma_{ij}]^k_{n+1}$=$[E_{ijkl}]^k_{n+1}$($[\varepsilon_{ijkl}]^k_{n+1}$-$[\zeta]^k_{n+1}[\varepsilon^{ori}_{ij}]^k_{n+1}$)

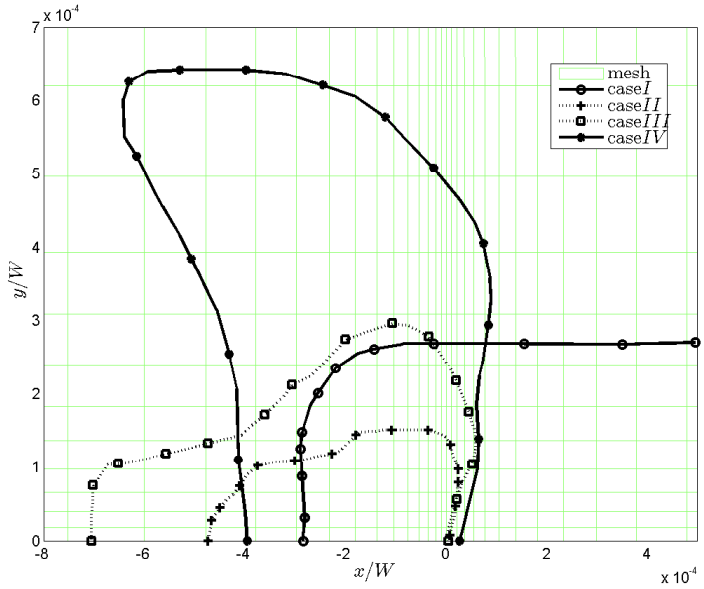
(v) Set k=k+1 and go to step (ii).

(vi) Set $n = n + 1$ and go to step (i).

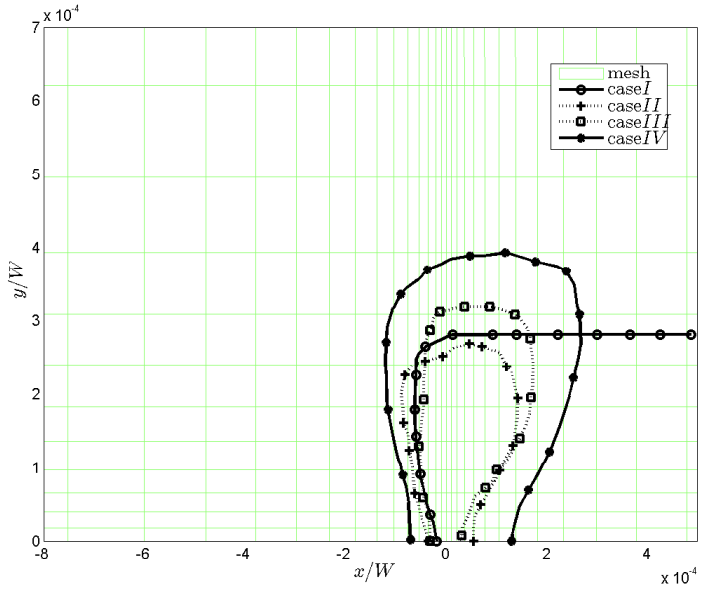
(vii) When the calculation finishes at all the integration points Abaqus checks the force equilibrium.

Algorithm 1: UMAT subroutine.

stress and plane strain conditions and shown in Figures 4.6, 4.7 and 4.8.



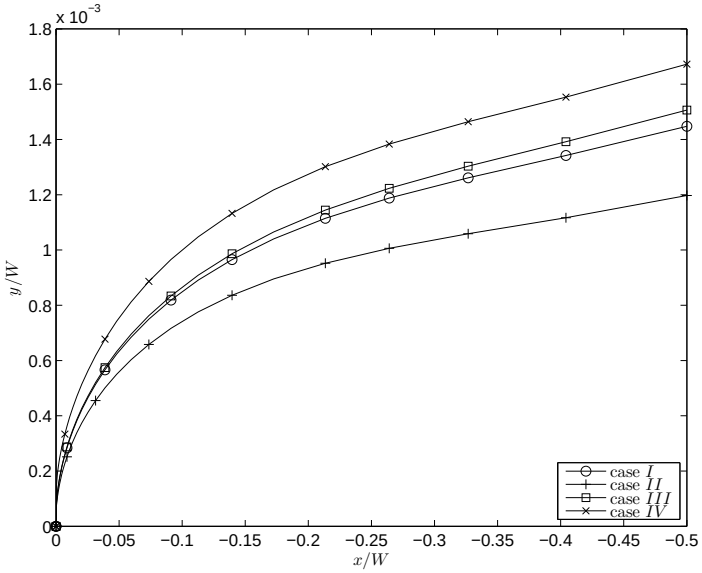
a



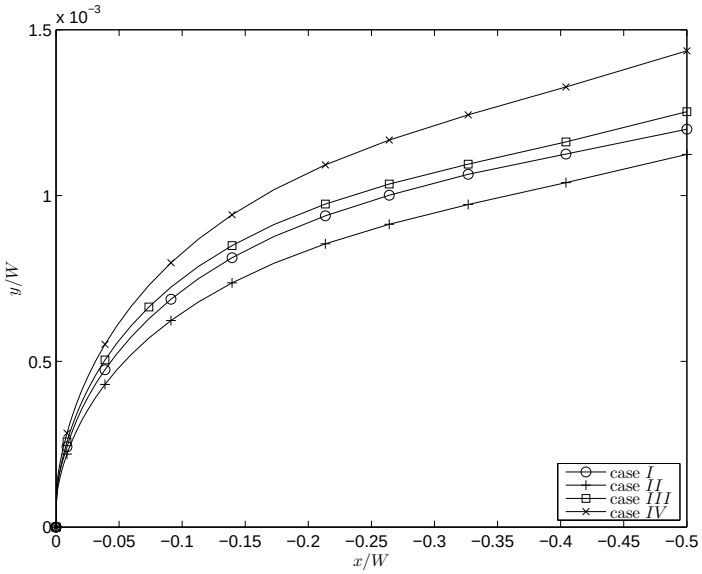
b

Figure 4.6. Effect of reorientation and reversible transformation on transformation region. (a) plane stress (b) plane strain.

In this study to calculate J-integrals a similar approach represented by [185] is used. J-integrals are calculated for cases II and III along the paths starting from the crack tip enlarging to untransformed region and plotted in Figure 4.9.



a

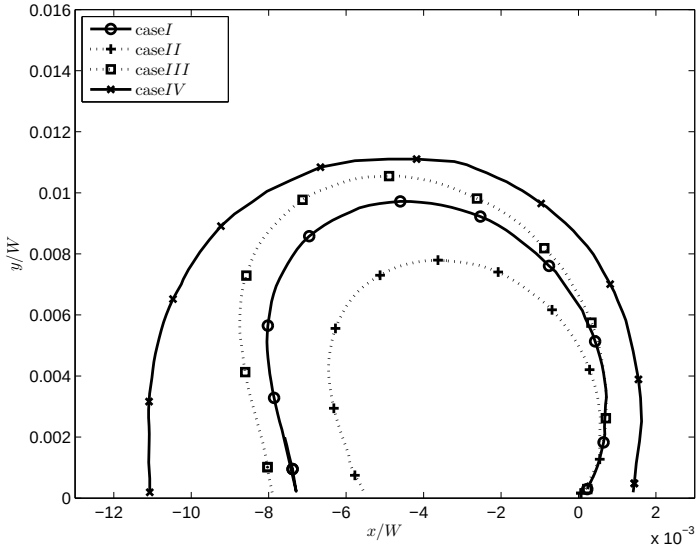


b

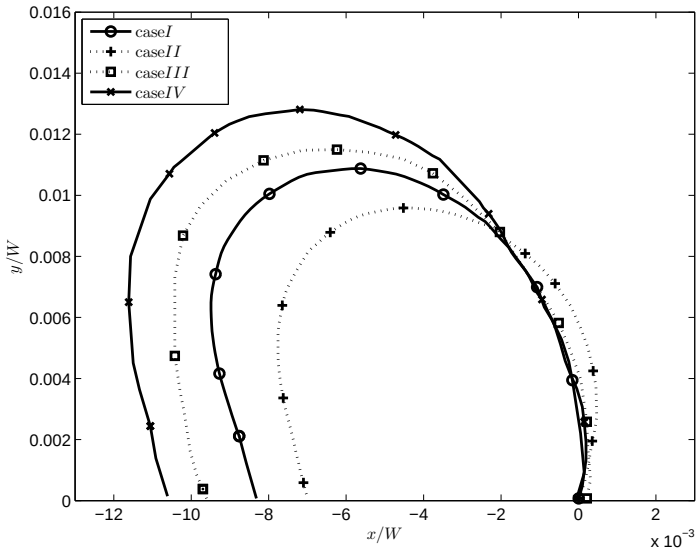
Figure 4.7. Effect of reorientation and crack growth on CFOD. (a) plane stress (b) plane strain.

4.4. Results and Conclusions

As shown in Figure 4.6 under plane stress and plane strain conditions martensite transformation regions around crack tip in cases I, II and III are smaller than the phase transformation region obtained in case IV, the static case. In addition, martensite regions obtained under plane strain conditions are smaller than those calculated under plane stress condition, which is consistent with earlier work by Lexcellent *et al.* [139].



a



b

Figure 4.8. σ_{yy} ($\sigma_{yy} = 580MPa$ is the average transformation plateau stress), contour plots under (a) plane stress (b) plane strain.

As described by McKelvey and Ritchie [207], phase transformation is inhibited in plane strain by the hydrostatic stress state ahead of a growing crack.

Also in case I and II, the height of martensite contours are close near the tip. This agrees with Yan *et al.* [24] who note that the reverse transformation in the wake region has negligible effect on transformation-induced stress intensity factor. In the case where reverse transformation is not allowed, martensite volume fraction contours in the wake region are very similar to the case of dilatant martensitic transformation which is also

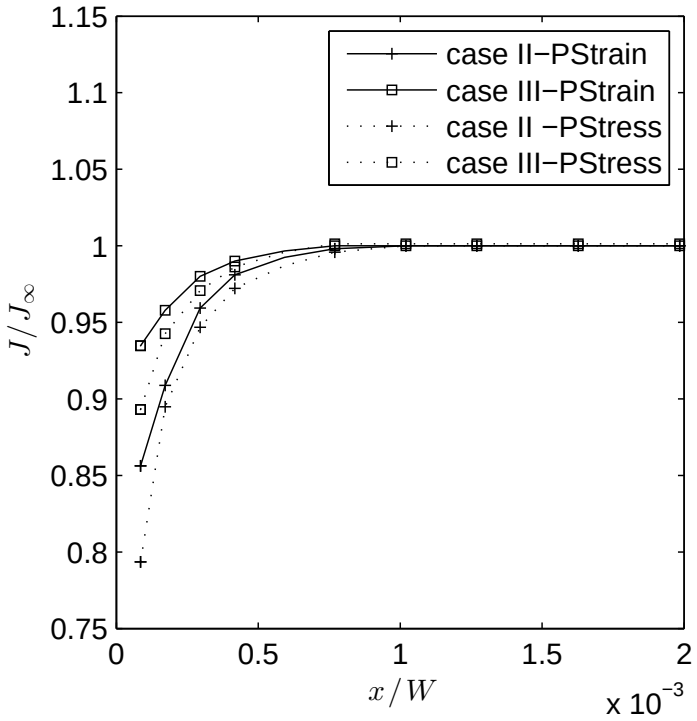


Figure 4.9. J-integrals calculated for cases II and III under plane stress and plane strain conditions. J_∞ is the J integral far from the crack tip where the material is in austenite phase.

pointed out by Budiansky *et al.* [209]; this is different than steady-state growth with reversible transformation. In case III, the size of the martensite transformation region around the crack tip is larger than cases II as a result of the dissipated energy that goes into the orientation of martensite variants.

CFODs plotted in Figure 4.7 shows that static crack opens more under plane stress and strain conditions. For case III since the transformation region is larger than cases I and II, the crack opening is higher. As shown in Figure 4.7 under plane strain conditions CFOD is less compared to plane stress condition which is similar to the result of Nguyen and Rahimian [185] comparing crack openings for plane stress and plane strain conditions in an elastic-plastic material.

When stresses around the crack tip are computed, in all the cases it is observed that the static crack yields higher stresses as shown in Figure 4.8; the reason for this is the energy that goes into steady-state crack growth in cases I, II and III. The stresses

obtained in the cases I and II are close, therefore the effect of reverse transformation on stress distribution around the crack is less than the effect of orientation of strain tensor.

In Figure 4.9, comparison of J-Integrals between cases II and III showed that orientation of martensite, which is a dissipative process itself, increases ΔJ, J_∞-J_{tip}, which is a measure of shielding for a growing crack [210, 211]. Under plane strain, $\Delta\ J/J_\infty$ is less than that of plane stress; a similar result is presented by Nguyen and Rahimian [185] for an elastic-perfectly plastic material.

When stresses around the crack tip, J-integrals and CFODs are considered, it can be concluded that the reorientation of martensite increases fracture toughness in SMAs.

The prospects of the present work include accounting for tensile-compressive asymmetry [122, 212], plastic deformation [123], dynamics [213] and cyclic loading effects [214, 215], as well as the extension to finite strains. The case of large strains and finite rotations can be treated to a first approximation considering a hypoelastic framework. Indeed, if the elastic strains are very small compared to the inelastic strains, the multiplicative decomposition of the deformation gradient into elastic and inelastic parts can be shown to be equivalent to a standard additive decomposition of the strain rate into elastic and inelastic parts. The numerical treatment of the constitutive equations in this case is straightforward and very similar to the case of small strains, with the main difference being the need to account for finite rotations. For UMAT implementation in Abaqus, the finite rotations can be accounted for incrementally by means of a built-in utility subroutine. The details of this procedure can be found in [200].

5. MODELING OF ANTI-PLANE SHEAR CRACK IN SMAS INCLUDING THERMOMECHANICAL COUPLING

The goal of this chapter is to add the effect of thermo-mechanical coupling to the analysis of an edge-cracked SMA under Mode-III loading. At first, the constitutive model represented by Moumni [117] is modified by including latent heat generation and intrinsic dissipation during phase change. Moumni [117] studied the anti-plane shear crack problem using hodograph method together with the asymptothic displacement field equations without considering the effect of latent heat and temperature increase.

Although, the experiments on SMAs showed that the temperature of the alloy changes considerably during phase transformation [216–220], most of the constitutive models available in the literature neglected that change due to latent heat generation. The experiments also showed that, increasing the strain rate increases latent heat generation and temperature. Churchill *et al.* [218] and Zhang *et al.* [219] investigated the effect of load rate on latent heat generation in an SMA wire and their measurements showed that increasing the load rate increases the temperature and phase transformation stresses.

Recently, some constitutive models are developed for SMAs to capture the phenomenon of latent heat generation under mechanical loading. One of the first models that considers latent heat generation during phase transformation is proposed by Entemeyer *et al.* [221]. Later, Auricchio and Sacco [222], Bouvet *et al.* [223] and Müller and Bruhns [224] developed constitutive models for SMAs by taking into account latent heat generation and intrinsic dissipation because of phase transformation.

In a recent work, Morin *et al.* [120] extended the ZM model by considering heat generation due to latent heat generation and intrinsic dissipation during phase change. They performed numerical simulations of thermomechanically coupled equations for a NiTi wire under tension and obtained stress-strain and temperature-strain curves under different load rates. They compared their numerical results to the experimental results

reported by Shaw and Kyriakides [220] and obtained a good agreement for moderate strain rates and a qualitative agreement for higher strain rates. They noted that when the the latent heat effect is not taken into account, the system is nearly isothermal. In other words, temperature variation within the SMA specimen is more significantly influenced by latent heat than intrinsic dissipation.

In this chapter, the approach presented by Morin *et al.* [120] is used together with small strains and small-scale yielding assumptions in the solution of the thermo-mechanically coupled problem. In addition to that, it is assumed that at the far field, where only austenite is present, solution can be predicted using asymptotic stress field equations. The chapter is organized as follows: in the first section, constitutive model presented by Moumni [117] is summarized and the problem is defined. Then, the analytical solution of the Mode-III problem is revisited. In the next part, the constitutive equation proposed by Moumni [117] is modified to capture latent heat generation during phase change. Finally, martensite fraction and temperature contours around the crack tip are obtained using a thermomechanicaly coupled algorithm and the effect of strain rate on the size of the phase transformation region is discussed.

5.1. Modeling of Phase Change

Moumni [117] developed a macroscopic model of solid to solid phase change following the framework of generalized standard materials with internal constraints [132, 133]. According to his model, free energy density function of a material undergoing phase transformation, Ψ, can be defined using state variables $\epsilon_{ij}, \beta, \alpha$ and T, where β and α are reversible and irreversible internal state variables respectively, and T represents the temperature. Using these parameters, the free energy density, Ψ of the material is defined as follows:

$$\Psi = \Psi\left(\epsilon, \beta, \alpha, T\right). \tag{5.1}$$

The state variables defined in the free energy density function Ψ are subjected to the

following internal constraints:

$$g_m(\epsilon_{ij}, \beta, \alpha) = 0, \quad \text{where} \quad m = 1, M, \tag{5.2}$$

$$h_m(\epsilon_{ij}, \beta, \alpha) \geq 0, \quad \text{where} \quad n = 1, N, \tag{5.3}$$

and the potential of internal constraints is:

$$\Psi_c = -\lambda_m g_m - \lambda_n h_n \quad \text{with} \quad \pi_n \geq 0 \quad \pi_n h_n = 0. \tag{5.4}$$

In the equation above λ_m and π_n are the Lagrange multipliers. Therefore, the associated Lagrangian function is $\mathcal{L} = \Psi + \Psi_c$.

The total free energy of a material undergoing phase change is composed of the individual free energy contributions and the energy responsible for the interaction of these phases. In this work the free energy density function of SMAs is defined using, austenite $U(e_{ij})$, and martensite $V(f_{ij})$ free energies, and the interaction energy which is denoted as $I(\zeta)$. The interaction energy is zero except during phase change, $I(0)$=$I(1) = 0$. Strain energies $U(e_{ij})$ and $V(f_{ij})$ are defined as:

$$U(e_{ij}, e_{kk}) = \mu_1 e_{ij} e_{ij} + \frac{1}{2} B \epsilon_{kk}, \tag{5.5}$$

$$V(f_{ij}, f_{kk}) = \mu_2 f_{ij} f_{ij} + \frac{1}{2} B \epsilon_{kk} + l. \tag{5.6}$$

In Equations 5.5 and 5.6, B is the bulk modulus, μ_1 and μ_2 are the shear moduli of austenite and martensite phases, l is the positive constant that represents the free energy level difference between parent and product phases at initial state, ϵ_{ij} is the macroscopic strain, e_{ij} and f_{ij} are the local strains of austenite and martensite phases, and ζ represents the martensite fraction.

The model proposed by Moumni [117] is built using a Reuss-type representation

of the material, and the local strains are expressed using the following equation:

$$(1-\zeta)e_{ij} + \zeta f_{ij} - \epsilon_{ij}^{d} = 0, \quad \zeta > 0, \quad and \quad 1-\zeta > 0, \tag{5.7}$$

where ϵ_{ij}^{d} is the deviatoric strain tensor.

The total free energy density function of the material can therefore be written as follows:

$$\Psi = (1-\zeta)U(e_{ij}) + \zeta V(f_{ij}) + I(\zeta). \tag{5.8}$$

Using Equations 5.4, 5.7 and 5.8, the Lagrangian is constructed as:

$$\mathcal{L} = (1-\zeta)U + \zeta V(f_{ij})I(\zeta) - \lambda_{ij}((1-\zeta)e_{ij} + \zeta f_{ij} - \epsilon_{ij}^{d}) - \lambda_1(1-\zeta) - \lambda_2\zeta. \tag{5.9}$$

State equations derived from the Lagrangian (Equation 5.9) are given below:

$$\mathcal{L}_{,\epsilon_{ij}^{d}} = \lambda_{ij} = \sigma_{ij}^{d}, \tag{5.10}$$

$$\mathcal{L}_{,\epsilon_{kk}} = B\epsilon_{kk} = P, \tag{5.11}$$

$$\mathcal{L}_{,e_{ij}} = (1-\zeta)(U^{'}(e_{ij}) - \lambda_{ij}) = 0, \tag{5.12}$$

$$\mathcal{L}_{,f_{ij}} = (\zeta)(V^{'}(f_{ij}) - \lambda_{ij}) = 0, \tag{5.13}$$

$$\mathcal{L}_{,\zeta} = V - U - \lambda_{ij}(f_{ij} - e_{ij}) + I^{'}(\zeta) + \lambda_1 - \lambda_2 = 0, \tag{5.14}$$

$$\mathcal{L}_{,\lambda_{ij}} = (1-\zeta)e_{ij} + \zeta f_{ij} - \epsilon_{ij}^{d} = 0. \tag{5.15}$$

where σ_{ij}^{d} is the deviatoric stress, $'$ represent the partial derivative, and P is the one third of the trace of the stress tensor, $\sigma_{ii}/3$. The constraints are:

$$\lambda_1 \geq 0 \quad and \quad \lambda_1(1-\zeta) = 0, \tag{5.16}$$

$$\lambda_2 \geq 0 \quad and \quad \lambda_2(\zeta) = 0. \tag{5.17}$$

Equations 5.10 – 5.17 are sufficient to determine the unknowns σ_{ij}, ζ, f_{ij}, e_{ij}, λ_{ij}, λ_1,

and λ_2 in terms of ϵ_{ij}^d.

When $\zeta = 0$ and the interaction energy term is neglected, $I(\zeta) = 0$, and the following equations are obtained:

$$\lambda_{ij} = \sigma_{ij}^d, \tag{5.18}$$

$$\lambda_{ij} = 2\mu\epsilon_{ij}^d, \tag{5.19}$$

$$P = B\epsilon_{kk}, \tag{5.20}$$

$$e_{ij} = \epsilon_{ij}^d, \tag{5.21}$$

$$\lambda_1 = 0, \tag{5.22}$$

$$\lambda_2 = \mu_2 f_{ij} f_{ij} - \mu_1 \epsilon_{ij}^d \epsilon_{ij}^d + l - 2\mu_1 \epsilon_{ij}^d (f_{ij} - \epsilon_{ij}^d). \tag{5.23}$$

As stated by Equations 5.16 and 5.17 the Lagrange multipliers $\lambda_1 \geq 0$ and $\lambda_2 \geq 0$. Because $\lambda_1 = 0$ (see Equation 5.22), only the sign of λ_2 has to be discussed. Equation 5.23 shows that λ_2 depends on the value of f_{ij}. If the minimum of λ_2 with respect to the variable f_{ij} is greater than zero, the positivity of λ_2 is satisfied. When $\lambda_{2,f_{ij}}$ is set to zero:

$$\lambda_{2,f_{ij}} = 2\mu_2 f_{ij} - 2\mu_1 \epsilon_{ij}^d = 0, \tag{5.24}$$

f_{ij}^* at this minimum point is:

$$f_{ij}^* = \eta \epsilon_{ij}^d, \tag{5.25}$$

where $\eta = \frac{\mu_1}{\mu_2}$. From the second derivative, the following condition is obtained:

$$\lambda_{2,ff} = 2\mu_2 > 0. \tag{5.26}$$

$\lambda_{2,ff} > 0$ provided that this is the minimum point. The value of λ_2 at this point is

calculated by inserting Equation 5.25 into Equation 5.23

$$\lambda_2^* = \mu_1(1-\eta)(\epsilon_{ij}^d \epsilon_{ij}^d) + l. \tag{5.27}$$

The positivity of the λ_2^* ensures that the system is physically admissible therefore the condition below has to be satisfied:

$$\epsilon_{ij}^d \epsilon_{ij}^d \leq \frac{l}{\mu_1(\eta-1)} = E^2. \tag{5.28}$$

When the same procedure is applied to the cases when; $\zeta = 1$ and $0 < \zeta < 1$, the following constitutive equations are obtained:

$$|\epsilon_{ij}^d| \leq E \Rightarrow \begin{cases} \zeta = 0, \\ \sigma_{ij}^d = 2\mu_1 \epsilon_{ij}^d, \\ P = B\epsilon_{kk}, \end{cases} \tag{5.29}$$

$$E \leq |\epsilon_{ij}^d| \leq F \Rightarrow \begin{cases} \zeta = \frac{|\epsilon_{ij}^d| - E}{F-E}, \\ \sigma_{ij}^d = \frac{2\mu_1\mu_2\epsilon_{ij}^d}{\mu_1\zeta + (1-\zeta)\mu_2}, \\ P = B\epsilon_{kk}, \end{cases} \tag{5.30}$$

$$|\epsilon_{ij}^d| \geq F \Rightarrow \begin{cases} \zeta = 1, \\ \sigma_{ij}^d = 2\mu_2 \epsilon_{ij}^d, \\ P = B\epsilon_{kk}, \end{cases} \tag{5.31}$$

where $|\epsilon_{ij}^d|$, E and F are:

$$|\epsilon_{ij}^d| = \sqrt{\epsilon_{ij}^d \epsilon_{ij}^d}, \quad E = \sqrt{\frac{l\mu_2}{\mu_1^2 - \mu_1\mu_2}}, \quad F = \sqrt{\frac{l\mu_1}{-\mu_2^2 + \mu_1\mu_2}}. \tag{5.32}$$

5.2. Anti-plane Shear Crack in SMAs

In this section, the phase transformation region around the tip of a crack subjected to anti-plane shear loading is studied using hodograph method. One of the first works that used the hodograph method to study the stresses around the notch tip in a work-hardening elastic-plastic material loaded by longitudinal shear was done by Rice [225]. Later the hodograph method has been used by many researchers [226–235] to investigate the deformation around the tip of a crack in elastic–plastic or hyper–elastic materials under Mode-III loading. Using the hodograph method, Amazigo [236] studied the problem of a semi-infinite body with an edge-crack in an elastic–plastic material subjected to out of plane shear and calculated crack opening displacements and J-integral. Silling [237] presented a numerical analysis to determine stress and strain fields around the crack tip under Mode-III loading in elastic and elastic–plastic materials using hodograph transformation. He claimed that singular stress fields can be calculated easily using the hodograph method in which non-linear PDEs are transferred to linear PDEs. Gao [238] developed a general analytical approach based on Henky's deformation theory and von Mises yield criterion to study anti-plane shear problems and stated that his formulation was more complex compared to the solutions obtained using hodograph transformation. Desindes and Daly [239] calculated the phase transformation around the crack tip under Mode-III loading by extending the work of Rice [54, 225] to SMAs. They compared their analytical calculations to the FE results and concluded that the size of phase transformation region calculated using FE is underestimated by approximately 50% from the analytical solution. In a recent work, Long and Hui [240] used the hodograph transformation to determine stress and displacement fields around tip of a Mode-III crack in a hyper-elastic material.

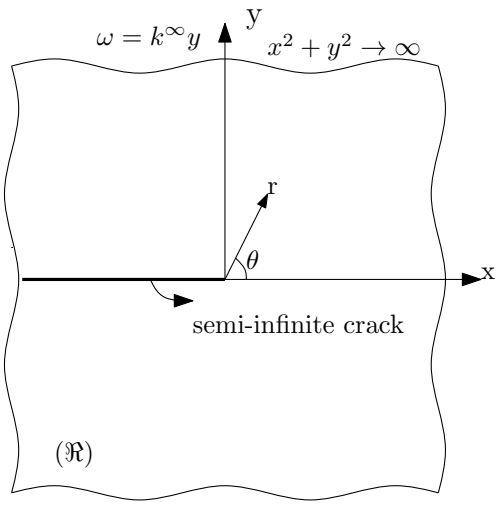


Figure 5.1. Schematic representation of the coordinate system attached to the crack tip.

5.3. Problem Statement

Figure 5.1 shows the cross section $\Re$ in an infinitely long plane, where z axis is perpendicular to $\Re$ plane, semi-infinite crack is located at $y = 0$ and the origin of the reference coordinate system is placed at the crack tip. Under Mode-III loading the displacements are written as:

$$u = 0, \quad v = 0, \quad and \quad \omega = \omega(x, y). \tag{5.33}$$

In anti-plane loading, when the gradient of displacement vector, ∇u_i, is constant the deformation is named as simple shear. The norm of the displacement gradient field, $\mid \nabla u_i \mid$, is the amplitude of simple shear. In this work, the plate shown in Figure 5.1 is subjected to simple shear parallel to the crack front at the far field where the components of the displacement vector satisfy the following conditions:

$$u = 0, \quad v = 0, \quad and \quad \omega = k^{\infty} y, \quad x^2 + y^2 \to \infty. \tag{5.34}$$

The stress tensor components except $\sigma_{xz} = \sigma_{zx}$ and $\sigma_{zy} = \sigma_{yz}$ are all zero:

$$\sigma_{xx} = \sigma_{yy} = \sigma_{zz} = 0, \quad \sigma_{xy} = 0, \quad \sigma_{xz} \neq 0 \quad and \quad \sigma_{yz} \neq 0, \tag{5.35}$$

The shear strains $\gamma_{xz}(=2\epsilon_{xz})$ and $\gamma_{yz}(=2\epsilon_{yz})$ are:

$$\gamma_{xz} = \frac{\partial \omega}{\partial x}, \quad \gamma_{yz} = \frac{\partial \omega}{\partial y}, \tag{5.36}$$

therefore the strain tensor is

$$\epsilon_{ij} = \epsilon_{ij}^{d} = \frac{1}{2}\begin{bmatrix} 0 & 0 & \frac{\partial \omega}{\partial x} \\ 0 & 0 & \frac{\partial \omega}{\partial y} \\ \frac{\partial \omega}{\partial x} & \frac{\partial \omega}{\partial y} & 0 \end{bmatrix}. \tag{5.37}$$

The shear stresses are therefore shown belows:

$$\sigma_{xz} = \mu(\zeta)\gamma_{xz}, \quad \sigma_{yz} = \mu(\zeta)\gamma_{yz}, \tag{5.38}$$

and the stress tensor is

$$\sigma_{ij} = \sigma_{ij}^{d} = \begin{bmatrix} 0 & 0 & \mu(\zeta)\gamma_{xz} \\ 0 & 0 & \mu(\zeta)\gamma_{yz} \\ \mu(\zeta)\gamma_{xz} & \mu(\zeta)\gamma_{yz} & 0 \end{bmatrix}. \tag{5.39}$$

At this point for the sake of simplicity, it is required to define the norms of stress, strain and the displacement gradient ∇u_i as follows:

$$\mid \sigma_{ij} \mid = (\sigma_{xj}\sigma_{xj} + \sigma_{yj}\sigma_{yj} + \sigma_{zj}\sigma_{zj})^{1/2}, \tag{5.40}$$

$$= \sqrt{2}(\sigma_{xz}^2 + \sigma_{yz}^2)^{1/2} = \tau, \tag{5.41}$$

for strain tensor,

$$\mid \epsilon_{ij} \mid = (\epsilon_{xj}\epsilon_{xj} + \epsilon_{yj}\epsilon_{yj} + \epsilon_{zj}\epsilon_{zj})^{1/2} \tag{5.42}$$

$$(2\epsilon_{xz}\epsilon_{xz} + 2\epsilon_{yz}\epsilon_{yz})^{1/2} = \sqrt{2}(\epsilon_{xz}^2 + \epsilon_{yz}^2)^{1/2} = k, \tag{5.43}$$

the magnitude of displacement gradient is equal to:

$$\mid \nabla u_i \mid = \left[\left(\frac{\partial \omega}{\partial x} \right)^2 + \left(\frac{\partial \omega}{\partial y} \right)^2 \right]^{1/2}, \tag{5.44}$$

$$= 2(\epsilon_{xz}^2 + \epsilon_{yz}^2)^{1/2}, \tag{5.45}$$

$$k = \frac{\mid \nabla u_i \mid}{\sqrt{2}}, \tag{5.46}$$

since $\epsilon_{ij} = \epsilon_{ij}^d$ and $\sigma_{ij} = \sigma_{ij}^d$:

$$\mid \epsilon_{ij} \mid = \mid \epsilon_{ij}^d \mid = k, \tag{5.47}$$

$$\mid \sigma_{ij} \mid = \mid \sigma_{ij}^d \mid = \tau. \tag{5.48}$$

Equations 5.47, 5.48, are inserted into Equations 5.29, 5.30, 5.31 and the following constitutive relations are determined:

$$k \leq E \Rightarrow \begin{cases} \zeta = 0, \\ \tau(k) = 2\mu_1 k, \end{cases} \tag{5.49}$$

$$E \leq k \leq F \Rightarrow \begin{cases} \zeta = \frac{|\epsilon_{ij}^d| - E}{F - E}, \\ \tau(k) = \frac{2\mu_1\mu_2 k}{\mu_1\zeta + (1-\zeta)\mu_2}, \\ P = B\epsilon_{kk}, \end{cases} \tag{5.50}$$

$$k \geq F \Rightarrow \begin{cases} \zeta = 1, \\ \tau(k) = 2\mu_2 k, \end{cases} \tag{5.51}$$

where E and F are:

$$E = \sqrt{\frac{l\mu_2}{\mu_1^2 - \mu_1\mu_2}}, \quad F = \sqrt{\frac{l\mu_1}{-\mu_2^2 + \mu_1\mu_2}}. \tag{5.52}$$

In anti-plane loading case, the equilibrium equations are reduced to:

$$\frac{\partial \sigma_{zx}}{\partial z} = 0, \quad \frac{\partial \sigma_{zy}}{\partial z} = 0, \quad \frac{\partial \sigma_{xz}}{\partial x} + \frac{\partial \sigma_{yz}}{\partial y} = 0. \tag{5.53}$$

Using Equation 5.39 and the last of the equilibrium equations can written:

$$\frac{\partial}{\partial x}\left[\mu(\zeta)\frac{\partial \omega}{\partial x}\right] + \frac{\partial}{\partial y}\left[\mu(\zeta)\frac{\partial \omega}{\partial y}\right] = 0. \tag{5.54}$$

and in expanded form:

$$\mu(\zeta)\frac{\partial^2 \omega}{\partial x^2} + \frac{\partial \mu(\zeta)}{\partial x}\frac{\partial \omega}{\partial x} + \mu(\zeta)\frac{\partial^2 \omega}{\partial y^2} + \frac{\partial \mu(\zeta)}{\partial y}\frac{\partial \omega}{\partial y} = 0. \tag{5.55}$$

The boundary conditions represented in Figure 5.1 can be expressed as follows:

$$\frac{\partial \omega}{\partial y}(x, y = \pm 0) = 0 \quad \forall \quad x < 0. \tag{5.56}$$

Away from the crack tip it is assumed that there is no phase transformation and the medium is homogeneously austenite. In that region, the solution is estimated using the Mode III asymptotic near-tip equations. Then, it is assumed that this solution is continuously connected to the solution of the problem in the vicinity of the crack tip. This assumption adds a new condition to the problem through following equations:

$$\omega \approx \frac{K_{III}}{\mu_1}\sqrt{\frac{2r}{\pi}}\sin\left(\frac{\theta}{2}\right), \tag{5.57}$$

$$\omega_{,x} \approx -\frac{K_{III}}{\mu_1\sqrt{2\pi r}}\sin\left(\frac{\theta}{2}\right), \tag{5.58}$$

$$\omega_{,y} \approx \frac{K_{III}}{\mu_1\sqrt{2\pi r}}\cos\left(\frac{\theta}{2}\right). \tag{5.59}$$

where, $K_{III} = \mu_1 k^{\infty}\sqrt{\pi\alpha}$ is the stress intensity factor of a crack with length α where simple shear with a magnitude k^{∞} is applied. All the attempts from this point on is to find w satisfying Equations 5.54, 5.56 and 5.57. For this purpose, the hodograph method is used as represented in the following sections.

5.4. Hodograph Method

The components of displacement gradient $\omega_{,x}$ and $\omega_{,y}$ are defined in terms of new independent variable ξ_i through hodograph transformation as follows:

$$(x, y) \rightarrow (\xi_1,\xi_2) \quad \xi_1 = \omega_{,x}(x, y) \quad \xi_2 = \omega_{,y}(x, y). \tag{5.60}$$

The coordinates of the physical plane $\Re$, x and y, are transformed to hodograph plane $\Re^H$ defined by cartesian coordinates, ξ_1 and ξ_2. Using the hodograph method the non-linear differential equation (Equation 5.55) will be transformed to a linear PDE through Legendre transformation. Legendre transformation of $\omega(x, y)$ to $U(\xi_1, \xi_2)$ will be as shown below:

$$U(\xi_1,\xi_2) = x\omega_{,x}(x, y) + y\omega_{,y}(x, y) - \omega(x, y) \quad \forall(x, y) \in \Re. \tag{5.61}$$

When Equation 5.60 is inserted into Equation 5.61,

$$U(\xi_1,\xi_2) = x\xi_1 + y\xi_2 - \omega(x, y) \quad \forall(x, y) \in \Re. \tag{5.62}$$

The coordinates x and y are then expressed in terms of ξ_1 and ξ_2 using the derivative of U with respect to ξ_i, and Equations 5.62 and 5.60,

$$\frac{\partial U(\xi_1,\xi_2)}{\partial \xi_1} = x, \quad \frac{\partial U(\xi_1,\xi_2)}{\partial \xi_2} = y, \quad on \quad \Re^H. \tag{5.63}$$

Substitute Equation 5.63 in Equation 5.62, $\omega(x, y)$ is written in terms of ξ_1 and ξ_2 as follows:

$$\omega(x, y) = \frac{\partial U(\xi_1, \xi_2)}{\partial \xi_1}\xi_1 + \frac{\partial U(\xi_1, \xi_2)}{\partial \xi_2}\xi_2 - U(\xi_1, \xi_2) \quad \text{on} \quad \Re^H. \tag{5.64}$$

To complete the transformation, Equations 5.56, 5.57 and 5.59 will be defined in the hodograph plane. Using polar coordinates, R and Φ, in hodograph plane, ξ_1 and ξ_2 are

written as:

$$\xi_1 = R\cos\Phi, \quad \xi_2 = R\sin\Phi. \tag{5.65}$$

When the asymptotic crack tip equations 5.57 and 5.60, 5.65 are used to define, R and Φ in terms of r and θ coordinates, the following is obtained:

$$R = \frac{K_{III}}{\mu_1\sqrt{2\pi r}}, \quad \Phi = \frac{1}{2}(\pi+\theta), \quad r \to \infty \quad -\pi \leq \theta < \pi \quad . \tag{5.66}$$

The Equation 5.66 demonstrates that, the points far away from the origin of $\Re$ plane transformed to the points close to the origin in hodograph plane, $\Re^H$.

It follows from Equation 5.50 that ζ is a function of $\mid \epsilon_{ij} \mid$ and $\mid \epsilon_{ij} \mid = {}^{\mid \nabla u_i \mid}/_{\sqrt{2}}$, where $\mid \nabla u_i \mid = R$, $\zeta = \zeta(R)$ and $\mu = \mu(R)$ therefore, the equilibrium equation, Equation 5.54, can be written in the hodograph plane as:

$$\frac{\partial(\mu(R)R\cos\Phi)}{\partial x} + \frac{\partial(\mu(R)R\sin\Phi)}{\partial y} = 0, \tag{5.67}$$

Equation 5.67 can be expanded as follows:

$$\frac{\partial R}{\partial x}\frac{\partial}{\partial R}\left[\mu R\cos\Phi\right] + \frac{\partial R}{\partial y}\frac{\partial}{\partial R}\left[\mu R\sin\Phi\right] + \frac{\partial \Phi}{\partial x}\frac{\partial}{\partial \Phi}\left[\mu R\cos\Phi\right] + \frac{\partial \Phi}{\partial y}\frac{\partial}{\partial \Phi}\left[\mu R\sin\Phi\right] = 0. \tag{5.68}$$

Which in a more simplified form becomes

$$(\mu R)'\left[\cos\Phi\frac{\partial R}{\partial x} + \sin\Phi\frac{\partial R}{\partial y}\right] + \mu R\left[-\sin\Phi\frac{\partial \Phi}{\partial x} + \cos\Phi\frac{\partial \Phi}{\partial y}\right] = 0. \tag{5.69}$$

"$'$" denotes the derivative with respect to R.

To solve the Equation 5.69 the following terms: $\frac{\partial R}{\partial x}$, $\frac{\partial R}{\partial y}$, $\frac{\partial \Phi}{\partial x}$, and $\frac{\partial \Phi}{\partial y}$ have to be defined in the hodograph plane. For this purpose $\frac{\partial \Phi}{\partial \xi_1}$, $\frac{\partial \Phi}{\partial \xi_2}$, $\frac{\partial R}{\partial \xi_1}$, and $\frac{\partial R}{\partial \xi_2}$ are written in terms of polar coordinates R and Φ.

$\frac{\partial R}{\partial \xi_1}$ and $\frac{\partial \Phi}{\partial \xi_1}$ are calculated from 5.65 as:

$$\frac{\partial R}{\partial \xi_1} = \cos\Phi, \tag{5.70}$$

$$\frac{\partial \Phi}{\partial \xi_1} = \frac{-\sin\Phi}{R}. \tag{5.71}$$

Similarly, $\frac{\partial R}{\partial \xi_2}$ and $\frac{\partial \Phi}{\partial \xi_2}$ are

$$\frac{\partial R}{\partial \xi_2} = \sin\Phi, \tag{5.72}$$

$$\frac{\partial \Phi}{\partial \xi_2} = \frac{\cos\Phi}{R}. \tag{5.73}$$

From Equation 5.63, x is evaluated as:

$$x = \frac{\partial U}{\partial R}\frac{\partial R}{\partial \xi_1} + \frac{\partial U}{\partial \Phi}\frac{\partial \Phi}{\partial \xi_1}, \tag{5.74}$$

when the Equations 5.70 and 5.71 are inserted into Equation 5.74:

$$x = \frac{\partial U}{\partial R}\cos\Phi - \frac{\partial U}{\partial \Phi}\frac{\sin\Phi}{R}, \tag{5.75}$$

Similarly using Equation 5.63, y is calculated as follows:

$$y = \frac{\partial U}{\partial R}\frac{\partial R}{\partial \xi_2} + \frac{\partial U}{\partial \Phi}\frac{\partial \Phi}{\partial \xi_2}, \tag{5.76}$$

then Equations 5.72 and 5.73 are substituted into Equation 5.76 to get y

$$y = \frac{\partial U}{\partial R}\sin\Phi + \frac{\partial U}{\partial \Phi}\frac{\cos\Phi}{R}. \tag{5.77}$$

From Equations 5.75 and 5.77, dx and dy are determined as follows:

$$dx = \frac{\partial}{\partial \Phi}\left[\frac{\partial U}{\partial R}\cos\Phi - \frac{\partial U}{\partial \Phi}\frac{\sin\Phi}{R}\right]d\Phi + \frac{\partial}{\partial R}\left[\frac{\partial U}{\partial R}\cos\Phi - \frac{\partial U}{\partial \Phi}\frac{\sin\Phi}{R}\right]dR, \tag{5.78}$$

$$dy = \frac{\partial}{\partial \Phi}\left[\frac{\partial U}{\partial R}\sin\Phi + \frac{\partial U}{\partial \Phi}\frac{\cos\Phi}{R}\right]d\Phi + \frac{\partial}{\partial R}\left[\frac{\partial U}{\partial R}\sin\Phi + \frac{\partial U}{\partial \Phi}\frac{\cos\Phi}{R}\right]dR. \tag{5.79}$$

dx and dy can be expanded as shown below:

$$dx = \left[-\sin\Phi\frac{\partial U}{\partial R} - \frac{\cos\Phi}{R}\frac{\partial U}{\partial \Phi} + \cos\Phi\frac{\partial^2 U}{\partial R\partial\Phi} - \frac{\sin\Phi}{R}\frac{\partial^2 U}{\partial \Phi^2}\right]d\Phi \tag{5.80}$$

$$+ \left[-\cos\Phi\frac{\partial^2 U}{\partial R^2} + \frac{\sin\Phi}{R^2}\frac{\partial U}{\partial \Phi} - \frac{\sin\Phi}{R}\frac{\partial U^2}{\partial R\Phi}\right]dR, \tag{5.81}$$

$$dy = \left[\cos\Phi\frac{\partial U}{\partial R} - \frac{\sin\Phi}{R}\frac{\partial U}{\partial \Phi} + \sin\Phi\frac{\partial^2 U}{\partial R\partial\Phi} + \frac{\cos\Phi}{R}\frac{\partial^2 U}{\partial \Phi^2}\right]d\Phi \tag{5.82}$$

$$+ \left[-\sin\Phi\frac{\partial^2 U}{\partial R^2} - \frac{\cos\Phi}{R^2}\frac{\partial U}{\partial \Phi} + \frac{\cos\Phi}{R}\frac{\partial U^2}{\partial R\Phi}\right]dR. \tag{5.83}$$

Which can be written in a simplified form follows:

$$dx = \alpha d\Phi + \beta dR, \tag{5.84}$$

$$dy = \gamma d\Phi + \delta dR, \tag{5.85}$$

supposing that the Jacobian of the system, $\nu = \alpha\delta - \beta\gamma$, is non–zero:

$$\frac{\partial R}{\partial x} = -\frac{\gamma}{\nu}, \quad \frac{\partial R}{\partial y} = \frac{\alpha}{\nu}, \quad \frac{\partial \Phi}{\partial x} = \frac{\delta}{\nu}, \quad \frac{\partial \Phi}{\partial y} = -\frac{\beta}{\nu} \tag{5.86}$$

where α, β, γ and δ are:

$$\alpha = -sin\Phi\frac{\partial U}{\partial R} - \frac{\cos\Phi}{R}\frac{\partial U}{\partial \Phi} + \cos\Phi\frac{\partial^2 U}{\partial R\partial\Phi} - \frac{\sin\Phi}{R}\frac{\partial^2 U}{\partial \Phi^2}, \tag{5.87}$$

$$\gamma = \cos\Phi\frac{\partial U}{\partial R} - \frac{\sin\Phi}{R}\frac{\partial U}{\partial \Phi} + \sin\Phi\frac{\partial^2 U}{\partial R\partial\Phi} + \frac{\cos\Phi}{R}\frac{\partial^2 U}{\partial \Phi^2}, \tag{5.88}$$

$$\beta = \cos\Phi\frac{\partial^2 U}{\partial R^2} + \frac{\sin\Phi}{R^2}\frac{\partial U}{\partial \Phi} - \frac{\sin\Phi}{R}\frac{\partial^2 U}{\partial R\partial\Phi}, \tag{5.89}$$

$$\delta = \sin\Phi\frac{\partial^2 U}{\partial R^2} - \frac{\cos\Phi}{R^2}\frac{\partial U}{\partial \Phi} + \frac{\cos\Phi}{R}\frac{\partial^2 U}{\partial R\partial\Phi}. \tag{5.90}$$

finally the equilibrium equation, Equation 5.54, reduces to,

$$(\mu R)' \left[-\gamma \cos\Phi + \alpha \sin\Phi\right] + \mu R \left[-\delta \sin\Phi - \beta \cos\Phi\right] = 0. \tag{5.91}$$

When $\alpha, \beta, \gamma, \delta$ are inserted into Equation 5.91 the following equation is obtained:

$$(\mu(R)R)' \left[\frac{\partial U}{\partial R} + \frac{1}{R}\frac{\partial U^2}{\partial \Phi^2}\right] + \mu(R)R \left[\frac{\partial U^2}{\partial R^2}\right] = 0. \tag{5.92}$$

Equation 5.92 is a linear and homogeneous PDE. The boundary conditions that are given in Equation 5.56 are translated to hodograph plane as follows:

$$\frac{\partial U}{\partial \Phi} = 0 \quad when \quad \Phi = 0, \quad \Phi = \pi, \quad \forall R > 0. \tag{5.93}$$

The asymptotic equations (Equations 5.57, 5.58, and 5.59) are inserted into Legendre equation (Equation 5.62) and the following equation is obtained for U:

$$U = x\left[-\frac{K_{III}}{\mu_1\sqrt{2\pi r}}\sin\left(\frac{\theta}{2}\right)\right] + y\left[\frac{K_{III}}{\mu_1\sqrt{2\pi r}}\cos\left(\frac{\theta}{2}\right)\right] - \left[\frac{K_{III}}{\mu_1}\sqrt{\frac{2r}{\pi}}\sin\left(\frac{\theta}{2}\right)\right], \tag{5.94}$$

then, Equations 5.74 and 5.76 are substituted into Equation 5.94, one gets:

$$\begin{aligned} U = &\left[\frac{\partial U}{\partial R}\cos\Phi - \frac{\partial U}{\partial \Phi}\frac{\sin\Phi}{R}\right]\left[-\frac{K_{III}}{\mu_1\sqrt{2\pi r}}\sin\left(\frac{\theta}{2}\right)\right] \\ &\left[+\frac{\partial U}{\partial R}\sin\Phi + \frac{\partial U}{\partial \Phi}\frac{\cos\Phi}{R}\right]\left[\frac{K_{III}}{\mu_1\sqrt{2\pi r}}\cos\left(\frac{\theta}{2}\right)\right] \\ &- \left[\frac{K_{III}}{\mu_1}\sqrt{\frac{2r}{\pi}}\sin\left(\frac{\theta}{2}\right)\right]. \end{aligned} \tag{5.95}$$

With the help of Equation 5.66, Equation 5.95 is simplified into the following:

$$U = \frac{K_{III}^2}{\mu_1^2 2\pi R} cos\Phi \quad \text{when} \quad R \to 0, \quad 0 \le \Phi \le \pi \tag{5.96}$$

When Equations 5.65, 5.75, and 5.77 are substituted into Equation 5.62 the following

expression for U is obtained:

$$U(\xi_1,\xi_2)=\left[\frac{\partial U}{\partial R}\cos\Phi-\frac{\partial U}{\partial \Phi}\frac{\sin\Phi}{R}\right]R\cos\Phi+\left[\frac{\partial U}{\partial R}\sin\Phi+\frac{\partial U}{\partial \Phi}\frac{\cos\Phi}{R}\right]R\sin\Phi-\omega(x,y), \tag{5.97}$$

Which in a more simplified form is:

$$\omega(x,y)=R^2\frac{\partial}{\partial R}\left(\frac{U(\xi_1,\xi_2)}{R}\right). \tag{5.98}$$

and once U is solved in the hodograph plane, ω can be obtained using Equation 5.97.

As a result, formulation of the the problem represented by Equations 5.54 and 5.56 are obtained now in hodograph plane (Equations 5.92 and 5.93). Using the constitutive equations (Equations 5.29, 5.30 and 5.31) together with the equilibrium equation (Equation 5.92) the phase transformation regions are determined in physical plane $\Re$.

When the boundary conditions is considered, the solution of the Equation 5.92 is obtained in the following form:

$$U(R,\Phi)=RI(R)cos\Phi. \tag{5.99}$$

where $I(R)$ is a singular integral to be evaluated.If Equation 5.99 is inserted back into Equation 5.92 the following integral equation is obtained:

$$I(R)=\frac{\sqrt{2}K_{III}^2}{\mu_1\pi}\int_R^\infty\frac{dt}{\tau(t)t^2}. \tag{5.100}$$

Using Equation 5.75, 5.77, and 5.99, x and y are defined as shown below:

$$x=I(R)+\frac{R}{2}I^{'}(R)-\frac{R}{2}I^{'}(R)\cos 2\Phi, \tag{5.101}$$

$$y=-\frac{R}{2}I^{'}(R)\sin 2\Phi. \tag{5.102}$$

When $r > 0$ and $\theta \in [-\pi, \pi]$, there exists a solution in terms of $R(r,\theta)$ and $\Phi(r,\theta)$, where $R > 0$ and $-\pi < \Phi < \pi$. Once R and ϕ are obtained, $\omega(x,y)$ can be evaluated by using the following:

$$\omega(x,y) = R^2 I^{'}(R)\cos\Phi. \tag{5.103}$$

Using $R = k\sqrt{2}$, the martensite fraction can be expressed as:

$$\zeta = \frac{\frac{R}{\sqrt{2}} - E}{F - E}. \tag{5.104}$$

5.5. Solution of the Problem

At first, $I(R)$ is calculated for each part of the constitutive relation namely $k \leq E, E \leq k \leq F and k \geq F$ (see Equations 5.49, 5.50 and 5.51) that are defined for austenitic, martensitic and transformation phases respectively. The displacement ω and martensite fraction ζ are calculated using Equations 5.103 and 5.104 as shown below:

When $k \leq E$:

$$I(R) = \frac{K_{III}^2}{\mu_1 \pi}\left[\int_R^{\sqrt{2}E} \frac{dt}{\mu_1 t^3} + \int_{\sqrt{2}E}^{\sqrt{2}F} \frac{dt}{At^2} + \int_{\sqrt{2}F}^{\infty} \frac{dt}{\mu_2 t^3}\right] \tag{5.105}$$

$$= \frac{K_{III}^2}{\mu_1 \pi}\left[\frac{1}{2\mu_1 R^2} + \frac{F-E}{AFE} + \frac{1}{4\mu_2 F^2} + \frac{1}{4\mu_1 E^2}\right], \tag{5.106}$$

where A is

$$A = 2\sqrt{\frac{l\mu_1\mu_2}{\mu_1 - \mu_2}}, \tag{5.107}$$

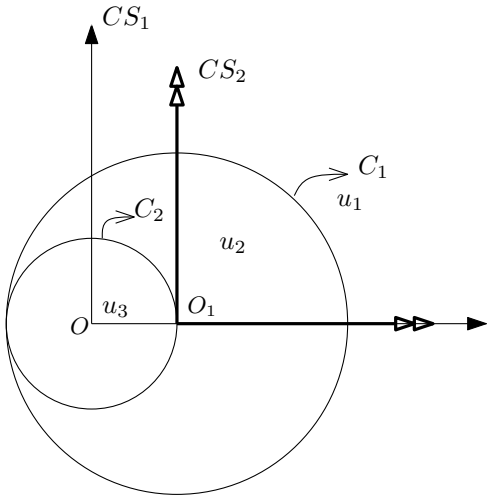


Figure 5.2. The domains of validity of the solution.

Using Equations 5.101, 5.102 and 5.105, R can be written in terms of x and y:

$$R = \sqrt{\frac{K_{III}^2}{2\mu_1^2\pi\left((x-H)^2+y^2\right)^{\frac{1}{2}}}}, \tag{5.108}$$

where

$$H = \frac{K_{III}^2}{\mu_1\pi}\left[\frac{1}{A}\frac{F-E}{AFE} + \frac{1}{4\mu_2F^2} - \frac{1}{4\mu_1E^2}\right]. \tag{5.109}$$

Because $R < \sqrt{2}E$, the solution is only valid outside of the region C_1 represented in Figure 5.2, where R is the radius of the circle C_1 and equal to $\frac{K_{III}^2}{4\mu_1^2E^2\pi}$. The center of circle C_1 is located at point $O(H,0)$ defined in coordinate system CS_1. For the sake of simplicity, R and Φ are defined relative to a new coordinate system CS_2 with the polar coordinated (r_1,θ_1), where the origin is transferred to the point O_1 as shown below:

$$R = \sqrt{\frac{K_{III}^2}{2\mu_2 \pi r_1}}, \tag{5.110}$$

$$\Phi = \frac{\pi + \theta_1}{2}. \tag{5.111}$$

The displacement in the first region, u_1 and ζ can be found with the help of Equations 5.104 and 5.103:

$$u_1 = \frac{K_{III}}{\mu_1}\sqrt{\frac{2r_1}{\pi}}\sin\frac{\theta_1}{2} \quad \text{and} \quad \zeta = 0. \tag{5.112}$$

In the transformation region $E \leq k \leq F$, $I(R)$ is calculated as:

$$I(R) = \frac{K_{III}^2}{\mu_1 \pi}\left[\frac{1}{4\mu_2 F^2} + \frac{\sqrt{2}}{AR} - \frac{1}{AF}\right], \tag{5.113}$$

using Equations 5.101, 5.102 and 5.113 R can be written in terms of x and y

$$R = \frac{K_{III}^2}{\sqrt{2}\mu_1\mu_2\pi F}\frac{\left(x + \dfrac{K_{III}^2}{4\mu_1\mu_2\pi F^2}\right)}{\left(x + \dfrac{K_{III}^2}{4\mu_1\mu_2\pi F^2}\right)^2 + y^2}. \tag{5.114}$$

The results for ζ and u_3 are then

$$\zeta = \frac{\dfrac{R}{\sqrt{2}} - E}{F - E}, \tag{5.115}$$

$$u_2 = \frac{K_{III}^2}{\sqrt{2}\mu_1\mu_2\pi F}\sqrt{1 + \frac{y}{\sqrt{x + \left(\dfrac{K_{III}^2}{4\mu_1\mu_2\pi F^2}\right)^2 + y^2}}}. \tag{5.116}$$

Because $\sqrt{2}E < R < \sqrt{2}F$, this solution is valid in the region that lies between circles C_1 and C_2 shown in Figure 5.2. The center of circle C_1 is on the positive x axis. C_1 is tangent to C_2 at the point $\left(-\frac{K_{III}^2}{4\mu_1\mu_2\pi F^2}, 0\right)$.

When $k \geq F$,

$$I(R) = \frac{K_{III}^2}{\mu_1 \pi}\left[\int_R^\infty \frac{dt}{\mu_2 t^3}\right], \tag{5.117}$$

$$= \frac{K_{III}^2}{\mu_1 \pi}\left[\frac{1}{2\mu_2 R^2}\right]. \tag{5.118}$$

Using Equations 5.101, 5.102 and 5.118 R can be written in terms of x and y as follows:

$$R = \sqrt{\frac{K_{III}^2}{2\mu_1\mu_2\pi\left(x^2+y^2\right)^{\frac{1}{2}}}}, \tag{5.119}$$

where

$$K_{III} = \mu_1 k^\infty \sqrt{\pi a}. \tag{5.120}$$

R is valid only inside the region C_2 which is shown in Figure 5.2. R is the radius of the circle with the origin located at $O(0,0)$ with a radius of $\frac{K_{III}^2}{4\mu_1\mu_2 F^2\pi}$; therefore, the solution for u and ζ at this region are:

$$u_3 = K_{III}\frac{\mu_1}{\mu_2}\sqrt{\frac{2r_1}{\pi}}\sin\frac{\theta_2}{2} \quad \text{and} \quad \zeta = 1. \tag{5.121}$$

5.6. Thermomechanical Coupling

In this section, the model that is summarized in Section 5.3 is improved by including temperature dependence in free energy density formulation. The heat density function associated with the phase change, $C(T)$ (see Figure 5.3), is now defined as

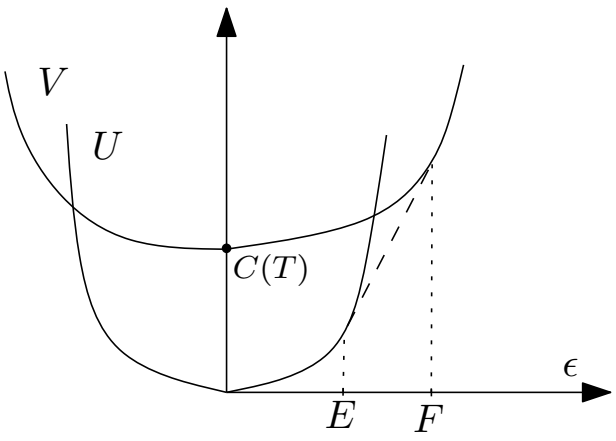


Figure 5.3. Free energy functions defined for each phase.

given below:

$$C(T) = \xi(T - A_f) + \kappa, \tag{5.122}$$

where ξ and κ are material properties. In this equation κ has a similar role with the term l. The modified free energy density functions are:

$$U(e_{ij}, e_{kk}) = \mu_1 e_{ij} e_{ij} + \frac{1}{2} B \epsilon_{kk}^2, \tag{5.123}$$

$$V(f_{ij}, f_{kk}) = \mu_2 f_{ij} f_{ij} + \frac{1}{2} B \epsilon_{kk}^2 + C(T). \tag{5.124}$$

The constraints are given as:

$$(1 - \zeta) e_{ij} + \zeta f_{ij} - \epsilon_{ij}^d = 0, \quad \zeta > 0, \quad and \quad 1 - \zeta > 0. \tag{5.125}$$

A constant specific heat capacity C_p, that is taken to be the same for austenite and martensite is added to the free energy density function Ψ as follows:

$$\Psi = (1 - \zeta) U(e) + \zeta V(f) + I(\zeta) + \rho C_p \left(T - T_0 - T ln \left(\frac{T}{T_0} \right) \right), \tag{5.126}$$

where ρ is the density of the alloy and T_0 is the reference temperature. The associated

Lagrangian function can therefore be written as:

$$\mathcal{L} = (1-\zeta)U(e_{ij}) + \zeta V(f_{ij}) + I(\zeta) - \lambda_{ij}((1-\zeta)e_{ij} + \zeta f_{ij} - \epsilon^d_{ij}) - \lambda_1(1-\zeta) - \lambda_2\zeta. \quad (5.127)$$

When the procedure explained in Section 5.5 is followed the constitutive relations written below are obtained:

$$|\epsilon^d_{ij}| \leq E \Rightarrow \begin{cases} \zeta = 0, \\ \sigma^d_{ij} = 2\mu_1\epsilon^d_{ij}, \\ P = B\epsilon_{kk} \end{cases} \quad (5.128)$$

$$E \leq |\epsilon^d_{ij}| \leq F \Rightarrow \begin{cases} \zeta = \frac{|\epsilon^d_{ij}|-E}{F-E}, \\ \sigma^d_{ij} = \frac{2\mu_1\mu_2\epsilon^d_{ij}}{\mu_1\zeta+(1-\zeta)\mu_2}, \\ P = B\epsilon_{kk} \end{cases} \quad (5.129)$$

$$|\epsilon^d_{ij}| \geq F \Rightarrow \begin{cases} \zeta = 1, \\ \sigma^d_{ij} = 2\mu_2\epsilon^d_{ij}, \\ P = B\epsilon_{kk} \end{cases} \quad (5.130)$$

where

$$|\epsilon^d_{ij}| = \sqrt{\epsilon^d_{ij}\epsilon^d_{ij}}, \quad E = \sqrt{\frac{C(T)\mu_2}{\mu_1^2 - \mu_1\mu_2}}, \quad F = \sqrt{\frac{C(T)\mu_1}{-\mu_2^2 + \mu_1\mu_2}}. \quad (5.131)$$

Figure 5.4 shows the transformation zones around the crack tip calculated using the material properties given in Table 5.1 and $K_{III} = 60$ MPa $\sqrt{m}$.

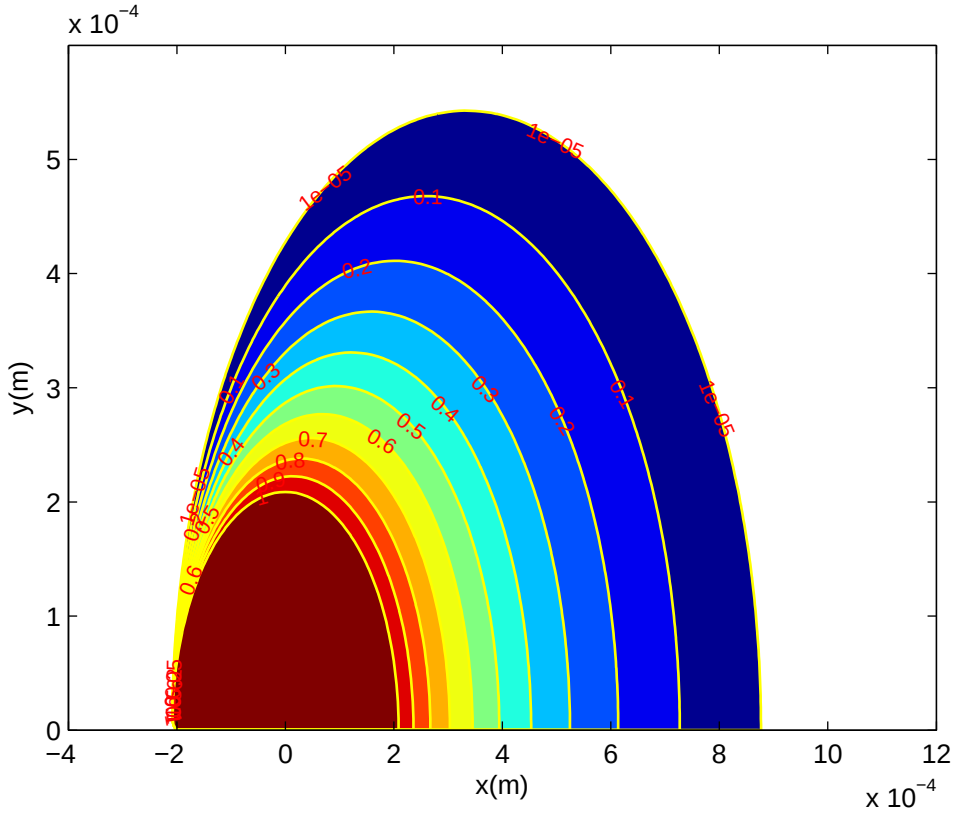


Figure 5.4. Martensite transformation region, thermomechanical coupling is not included, $T_0 = 343\ K$.

Table 5.1. Material properties used in the analysis.

E_A	61500 MPa
E_M	24000 MPa
κ	6.8920 MPa
ξ	0.2914 $MPa/^oC$
C_p	$0.440x10^{-3}\ J.kg^{-1}.K^{-1}$
ρ	$6500x10^6 kg.m^{-3}$
A_f	313 K
k	$18W.m^{-1}.K^{-1}$
a	6.8920 MPa
b	6.9091 MPa

5.7. Derivation of Heat Equation

In this work the reorientation of martensite is not included as an internal variable in the definition of the free energy density equation, only the dissipation due to martensite transformation is taken into account. Using the dissipation equation given by Zaki and Moumni [2] the pseudo potential of dissipation can be expressed as follows:

$$D = [a(1-\zeta) + b\zeta]\,|\dot{\zeta}|. \tag{5.132}$$

As it is summarised in the introduction chapter, the thermodynamic force related to phase change A_ζ is the sub-gradient of dissipation potential D, $A_\zeta \in \partial_{\dot{\zeta}} D(\zeta, \dot{\zeta})$, which is

$$D(\zeta, \dot{\zeta}) - D(\zeta, 0) \geq A_\zeta(\dot{\zeta} - 0). \tag{5.133}$$

Therefore, the intrinsic dissipation can be written as:

$$D_1 = A_\zeta \dot{\zeta} \geq 0. \tag{5.134}$$

The dissipation potential can be derived using the Clausius-Duhem inequality that is shown below:

$$\sigma_{ij}\dot{\epsilon_{ij}} + \rho(T\dot{s} - \dot{e}) - \frac{q_i}{T}T_{,i} \geq 0, \tag{5.135}$$

where e is the internal energy density and s is the entropy. The first law of thermodynamics can be written using the free energy function as follows:

$$\dot{\psi} + \dot{T}s + T\dot{s} = \sigma_{ij}\dot{\epsilon_{ij}} + r - q_{i,i}, \tag{5.136}$$

where r represents the amount of heat generated per unit volume per unit time in the body. Using Equation 5.136, the intrinsic dissipation part given in Equation 5.135 is

expressed as:

$$D_1 = T\dot{s} + q_{i,i} - r, \tag{5.137}$$

which can be rewritten as substituting $\dot{s}$

$$D_1 = -T\frac{\partial^2 \mathcal{L}}{\partial T \partial \dot{\epsilon}_{ij}}\dot{\epsilon}_{ij} - T\frac{\partial^2 \mathcal{L}}{\partial T \partial \zeta}\dot{\zeta} - T\frac{\partial^2 \mathcal{L}}{\partial T^2}\dot{T} + q_{i,i} - r. \tag{5.138}$$

The heat dissipation term D_2 is:

$$D_2 = -\frac{q_i}{T}T_{,i}. \tag{5.139}$$

When the heat capacity is added to the free energy density equation, the entropy, which is calculated from $s = -\partial\mathcal{L}/\partial T$, becomes:

$$s = \rho C_p ln\left(\frac{T}{T_0}\right) - \xi\zeta. \tag{5.140}$$

The following heat equation is derived using the Equations 5.140 5.134 and 5.138 [125]:

$$\rho C_p \dot{T} - kT_{,ii} = T\frac{\partial C(T)}{\partial T}\dot{\zeta} + [a(1-\zeta) + b\zeta]\,|\dot{\zeta}|. \tag{5.141}$$

In the next section to find the temperature increase around the crack tip during the phase change, the heat equation that is coupled with the equilibrium equation, will be solved numerically. The procedure is explained in the following section.

5.8. Numerical Analysis

The heat equation, Equation 5.141 and the equilibrium equation are coupled. They will be solved using MATLAB PDE solver, as it is summarized in Figure 5.6. In

MATLAB the heat equation is given as:

$$d\dot{T} - cT_{,ii} - aT = f. \tag{5.142}$$

During numeric solution the coefficients a and f are updated at each node upon evolution of martensite fraction.

Since the plate is taken to be very large compared to the region of interest, at the free edges insulated boundary conditions are applied. The geometry of the problem is shown in Figure 5.5 and the material parameters used are given in Table 5.1. A very fine mesh with an average length of 0.01 mm is used and the stability of the analysis is checked using the equation below [241]:

$$\Delta t > \frac{\rho C_p}{6k} \Delta L_e^2, \tag{5.143}$$

where L_e is the average length of side of elements. MATLAB function "parabolic" uses a method called " method of lines semi–discretization" to reduce parabolic equations to elliptic equations. The reduced elliptic equations are solved using finite element method but if the coefficients given in Equation 5.142 have time dependent data then these derivatives are calculated by finite difference of the given matrix of coefficients. In the numerical solution of the reduced elliptical function MATLAB ODE Suite Functions are used [242]. Using the time step is controlled with an error criterion; the coefficients are recalculated when the error tolerance is exceeded. To have a constant load rate during the solution, the time step obeying the condition given in Equation 5.143 is used and it is checked at the beginning of each increment.

The solution procedure is initiated with a load increment, Δk^{∞}, that is applied in a period of time Δt, and ΔK_{III} is calculated using $\Delta K_{III} = \mu_1 \Delta k^{\infty} \sqrt{\pi \alpha}$. Then using Equations 5.114 and 5.115, R and ζ are evaluated at each integration points. Next, Equation 5.141 is solved numerically and the temperature increase is obtained. By using the updated temperatures, $C(T)$, $F(T)$ and $E(T)$ are evaluated using Equations 5.122 and 5.131, and then Equation 5.115 used once again to find ζ. At this point

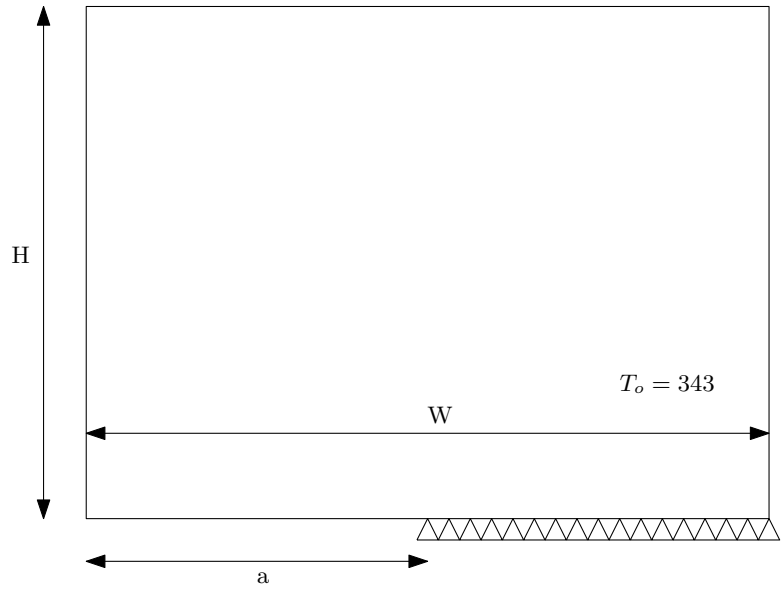


Figure 5.5. The geometry of the problem and the boundary conditions ($W = 100\ mm$, $H = 100\ mm$, $a = 50\ mm$).

a tolerance term, ζ_{tol} is defined (see Figure 5.6), if $\zeta_{tol} < 0.005$ then the solution passes to the next increment, else it returns to the solution of heat equation step and FE calculates the new temperature and then ζ is updated until the tolerance criterion is satisfied. In each iteration, the equilibrium equation is checked by means of hodograph method. Finally the analysis ends when $K_{III} = 60$ MPa $\sqrt{m}$.

As a result of the numerical calculations, the temperature contours under different load rates around the crack tip are plotted in Figures 5.8 and 5.9. In addition to that, the effect of strain rate on the size of the transformation region is shown in Figure 5.7.

5.9. Results and Discussion

In this chapter, the anti plane shear problem is solved and the temperature increase around the tip of a Mode-III crack is investigated. For this purpose, the solution represented by Moumni [117] is revisited and the hodograph solution is coupled with the heat equation to calculate latent heat generation and intrinsic dissipation during phase transformation. As a result, the temperature distribution around the tip of a

Initial conditions are $K_{III} = 0$, $T_0 = 343K$, $\zeta_0 = 0$, $k^{\infty} = 0$, in the algorithm below the subscripts represents the step number.

for $k = 0$ to 2.46×10^{-3} **do**

1) Using given Δk^{∞} calculate ΔK_{III} using $\Delta K_{III} = \mu_1 \Delta k^{\infty} \sqrt{\pi \alpha}$.

2) By substituting K_{III} and material properties given in Table 5.1 to Equations 5.114 and 5.115, R^2 and ζ^2 are calculated.

3) From Equation 5.141, ΔT is evaluated numerically using parabolic solver and T^3 is obtained.

4) Using T^3, Equations 5.122 and 5.131, $C(T)^4$, $F(T)^4$ and $E(T)^4$ are calculated.

5) $C(T)^4$, $F(T)^4$ and $E(T)^4$ and Equation 5.115 are used to calculate ζ^5.

6)A tolerance term is defined: ζ_{tol}=$(\zeta^5 - \zeta^2)/\zeta^2$

if $\zeta_{tol} < 0.005$ **then**

return to step 3

else

return to for statement and increase the increment

end if

end for

Figure 5.6. Algorithm of thermo-coupling analysis for anti-plane loading.

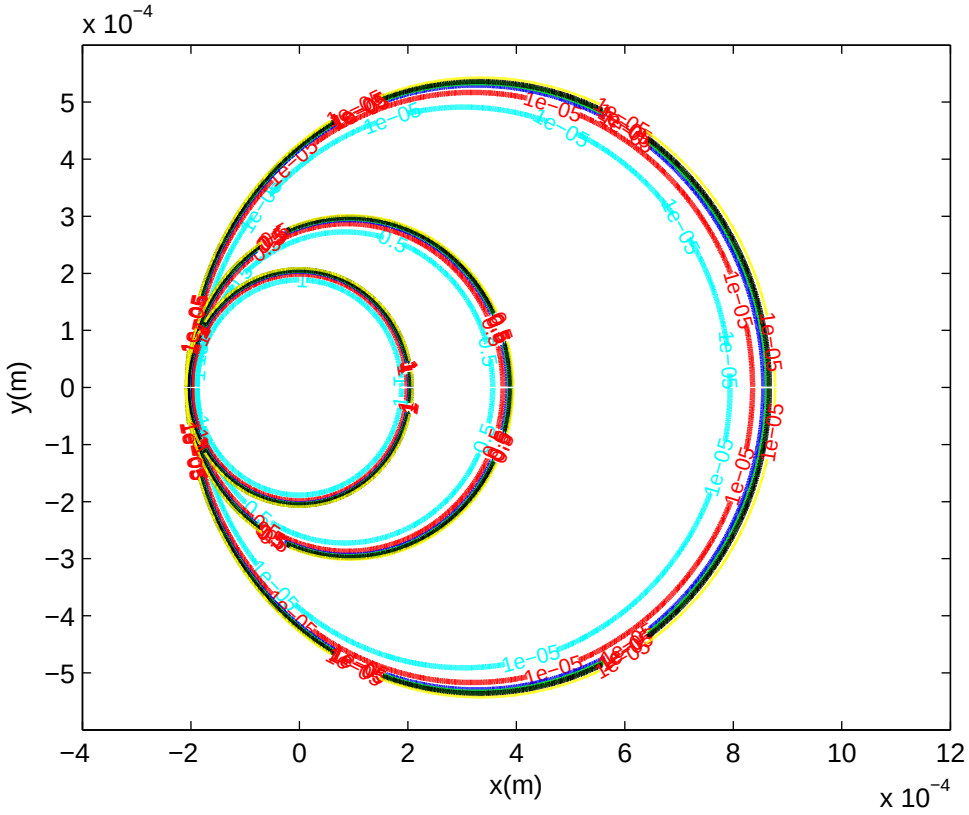
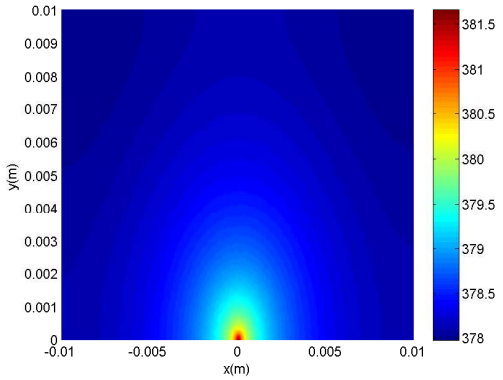
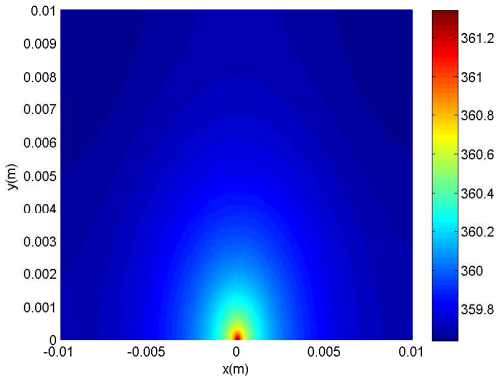


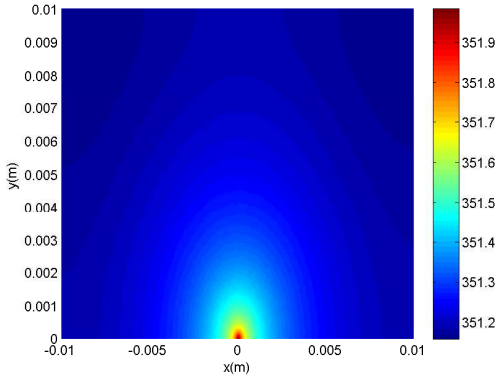
Figure 5.7. ζ contours. $\zeta = 1$ is the inner circle, $\zeta = 0.5$ is the middle circle, $\zeta = 1 \times 10^{-5}$ represents the outer circle. Colours: cyan: $\dot{k^{\infty}} = 2.56 \times 10^{-5}$ (1/s), red: $\dot{k^{\infty}} = 1.280 \times 10^{-5}$ (1/s), blue: $\dot{k^{\infty}} = 0.64 \times 10^{-5}$ (1/s), green: $\dot{k^{\infty}} = 0.43 \times 10^{-5}$ (1/s), black: $\dot{k^{\infty}} = 0.32 \times 10^{-5}$ (1/s) and yellow curve is when the latent heat generation is neglected.



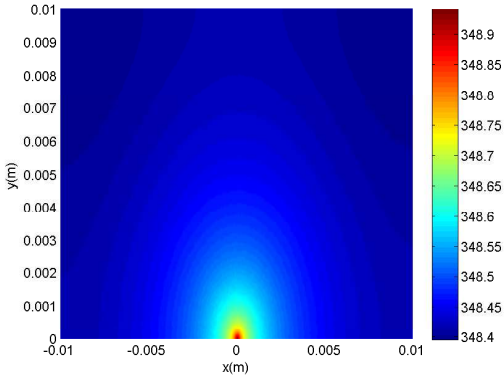
a $\dot{k^{\infty}} = 2.56 \times 10^{-5} s^{-1}$



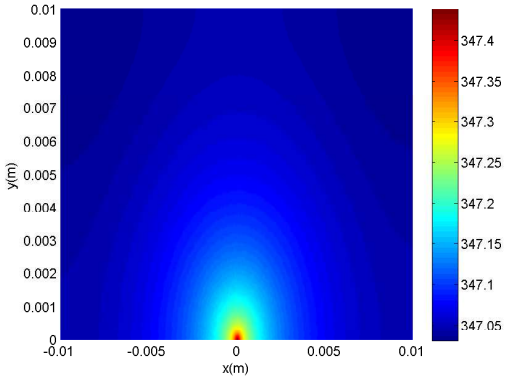
b $\dot{k^{\infty}} = 1.280 \times 10^{-5} s^{-1}$



c $\dot{k^{\infty}} = 0.64 \times 10^{-5} s^{-1}$



d $\dot{k^{\infty}} = 0.43 \times 10^{-5} s^{-1}$

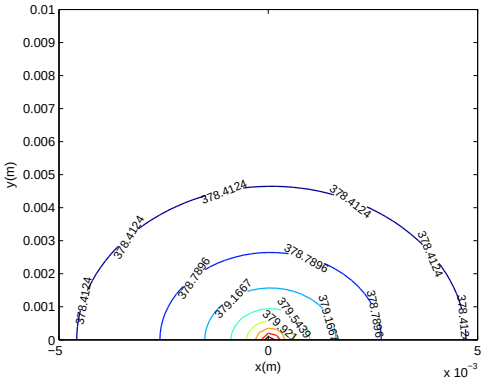


e $\dot{k^{\infty}} = 0.32 \times 10^{-5} s^{-1}$

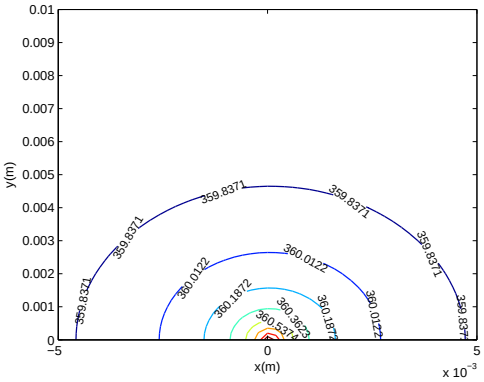
Figure 5.8. Temperature increase due to thermomechanical coupling.

crack under Mode III loading is determined. Contour plot given in Figure 5.8 and the isotherms in Figure 5.9 show that the temperature increase is highest for the highest load rate, $\dot{k^{\infty}} = 2.56 \times 10^{-5} s^{-1}$.

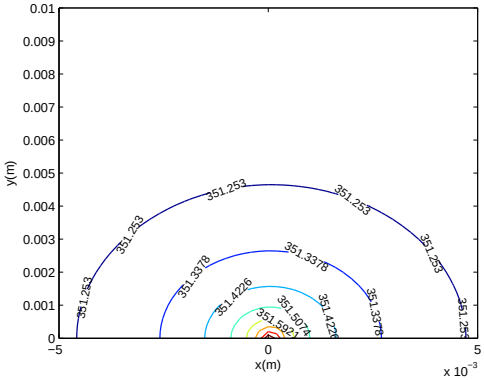
As shown in Figure 5.10, when the latent heat is neglected, and only the intrinsic



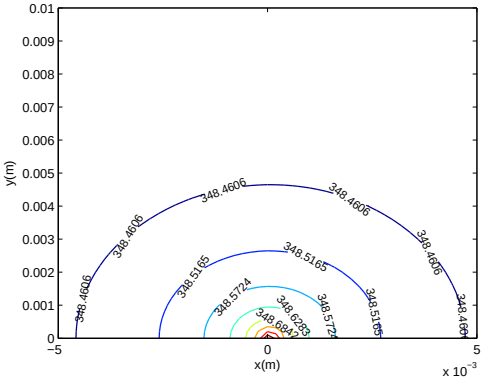
a $\dot{k^{\infty}} = 2.56 \times 10^{-5} s^{-1}$



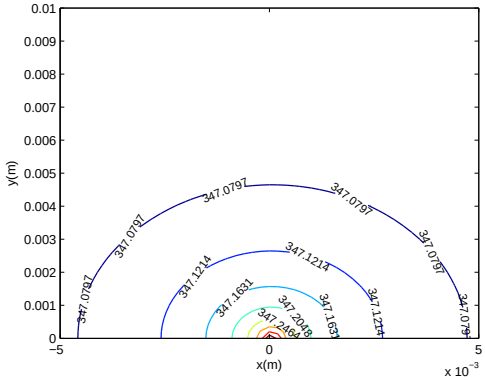
b $\dot{k^{\infty}} = 1.28 \times 10^{-5} s^{-1}$



c $\dot{k^{\infty}} = 0.64 \times 10^{-5} s^{-1}$



d $\dot{k^{\infty}} = 0.43 \times 10^{-5} s^{-1}$



e $\dot{k^{\infty}} = 0.32 \times 10^{-5} s^{-1}$

Figure 5.9. Isotherms around the crack tip.

dissipation is taken into account the temperature rise is very small. Therefore the effect of intrinsic dissipation on temperature rise can be neglected. This result is consistent with the study of Morin [125] where it is observed that the amount of temperature change due to intrinsic dissipation is very small.

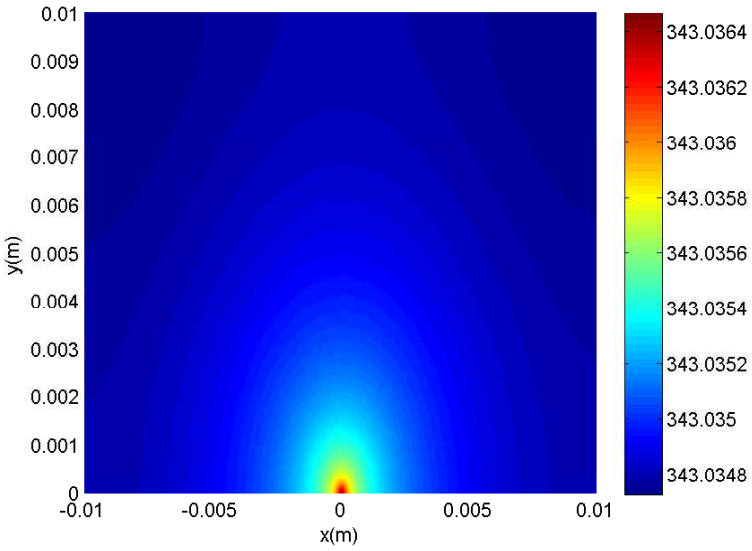


Figure 5.10. The temperature contour plot where only intrinsic dissipation is taken into consideration and the latent heat is neglected.

The constitutive model is enhanced by heat density function $C(T)$, providing that if the temperature increases, the transformation stresses also increase. The results of this study show that, when the transformation plateau shifts upwards, the size of the transformation region reduces. This finding supports the previous studies done by Daly *et al.* [243] and Simsek [57]. In both of these work, they investigated the effect of transformation stresses to size of phase transformation region in a NiTi specimen under Mode I loading, and concluded that transformation region gets smaller when the transformation plateau rises.

The difference between the area of the transformation region of the isothermal case,S_{iso}, and the area of the region where the thermomechanical coupling is considered, S_{cp}, is calculated for different load rates and results are plotted in Figure 5.11. As shown in Figure 5.11, at the regions where the latent heat generation is highly localized ($\zeta = 0.5$), more shrinkage on the transformed area is observed compared to regions where $\zeta = 0^+$. As the load rate increases, the generated latent heat mostly accumulates in the martensitic region $\zeta = 1$, and increases the transformation temperatures in fully martensite region, thus contracting phase transformation region more. As shown in Figure 5.11, the red curve represents the contraction of the area of fully

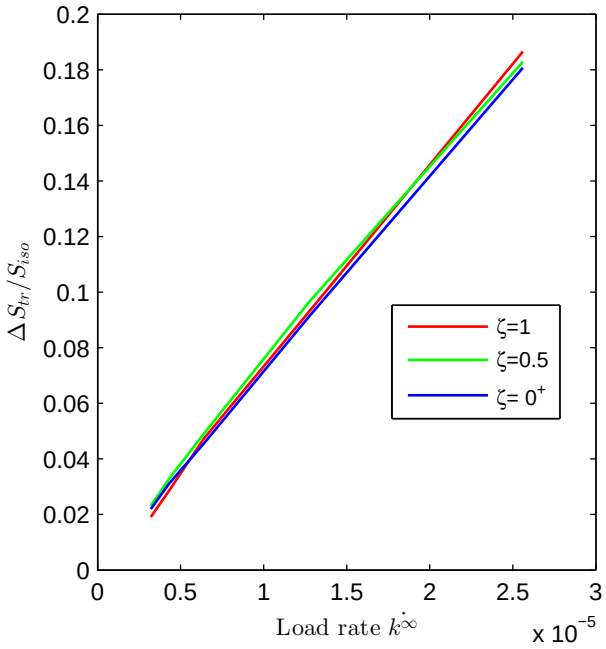


Figure 5.11. The change of the area of transformation region, $\Delta S_{tr}/S_{cp}$, where $\Delta S_{tr} = S_{iso} - S_{cp}$, versus the applied load $\dot{k}^{\infty}$.

transformation region, $\zeta = 1$, which is slightly greater than other curves when the load rate is maximum.

In this study, different than the previous works available in the literature, the variation of temperature around the tip of a crack subjected to Mode-III loading is analyzed. The results showed that, temperature around the tip increases when the load rate increases and the area of transformation region reduces.

To conclude, the results showed that, the latent heat generation affects the size of phase transformation region and increases the transformation stresses around the crack tip. In addition to that, it is observed that, the effect of intrinsic dissipation on thermomechanical behavior is small compared to the effect of latent heat effect. It can also be concluded that thermomechanical coupling should be considered in numerical evaluations of fracture parameters of SMAs. This approach could also be useful to investigate the effect latent heat generation on the toughness of SMAs. More experiments and calculations will be needed to study the effect of latent heat generation on fracture toughness. As a future study, the temperature contours obtained in this research can

be compared to experimental measurements; the model parameters can be calibrated, and a very good agreement with the model represented here can be obtained.

6. SUMMARY & CONCLUSION

In this thesis the effect of phase transformation on fracture of SMAs is investigated, the results are summarized as follows:

At first, the size of the martensitic region around the tip of an edge-cracked SMA plate is calculated analytically using ZM model. A good agreement with the experimental results of Robertson *et al.* [35] is obtained. Because the equation proposed to estimate the martensitic region is given in closed form, the size and the shape of the transformation region around the crack tip can be evaluated simply by inserting loading and material properties into the equation once the stress intensity factor is calculated properly. The next step (Chapter 3) is devoted to the investigation of SIF and other fracture parameters. In Chapter 3 the non-homogeneity around crack tip and contour dependent J-integrals are discussed and SIFs are calculated directly using strain energy output directly. The comparison of SIFs obtained using Auricchio's and ZM models showed that the energy dissipated through phase transformation decreases SIF. To support this conclusion one more comparison between superelastic SMA plate and fully austenite homogeneous plate is done and the results supported to the claim that phase transformation increases toughness. As a future work, this claim should be checked through experiments using NiTi with different transformation stresses. Besides that, in Chapter 3, in addition to previous studies in the literature, T-stresses are included in the formulation of the extent of phase transformation and results showed that, T-stresses should be considered in calculation of the extent of the phase transformation region. When the T-stresses are taken into account the extent of phase transformation region is closer to the that obtained using FE. The last topic discussed in this chapter was the effect of volumetric transformation strain on toughness. Unfortunately to get an accurate conclusion was impossible because the volume contraction showed a little effect on SIF.

So far the concern was to analyse the phase transformation region and fracture parameters for a static crack. In the fourth chapter, the stationary movement method is

implemented to investigate a steadily moving crack to observe the effect of crack growth on fracture of SMA. The phase transformation region of the tip of a steadily growing crack was found to be smaller when compared to that of a static crack. Moreover, for the growing crack, the martensitic regions determined under plane strain were smaller than the one obtained for the case of plane stress. This result is consistent with earlier work of Lexcellent *et al.* [139] and also with the results of McKelvey and Ritchie [207] who stated that phase transformation is inhibited in plane strain by means of the hydrostatic stress state ahead of the crack tip. In the steadily growing crack, in the cases with and without considering a reverse transformation, the height of volumetric martensite fraction contours are close near the tip. This result is in good agreement with Yan *et al.* [24] who noted that the reverse transformation in the wake region has negligible effect on transformation-induced stress intensity factor. In the case of phase transformation without reverse transformation, martensite volume fraction contours at the wake region were very similar to the case of dilatant martensitic transformation as was pointed out by Budiansky *et al.* [209]. In steady-state growth case without considering the reorientation of martensite, the size of the martensite transformation region around the crack tip was larger than case where the reorientation of martensite was taken into account. When stresses around the crack tip are computed, it is observed that the static crack yields higher stresses compared to all steady-state cases because of the energy that goes into steady-state crack growth. The stresses obtained for the steadily moving crack with and without reverse transformation were close. It can be concluded that the effect of reverse transformation on stress distribution around the crack is less than the effect of orientation of strain tensor.

In literature only Desindes and Daly [239] investigated the extent of phase transformation regions under anti-plane loading. The originality of the solution represented in Chapter 5 lies in the fact that, this is the first study that predicted temperature increase around the crack tip in an SMA using the analytical solution obtained from the hodograph method with numerical solution of the heat equation. The results showed that a considerable amount of temperature increase is obtained effecting the size of the transformation region around the crack tip.

From these discussions above the following conclusions are drawn:

(i) In this dissertation the size and the shape of the martensitic region calculated using ZM model is in a good agreement with the experimental results available in the literature.

(ii) The results obtained showed that the size of the phase transformation regions plays an important role on SIF calculations. The energy dissipated through phase change enhances the toughness of the SMA.

(iii) Comparison of CTODs, SIFs, and dissipated energies demonstrated that phase transformation plays an important role in toughness prediction.

(iv) For a steadily growing crack in an SMA plate, when stresses around the crack tip, J-integrals and CFODs are considered, it is concluded that the reorientation of martensite increases the fracture toughness. The reorientation of martensite should be taken into account if the specimen is subjected to non-proportional loading.

(v) The size of phase transformation region changes due to latent heat generation around the tip of the crack under anti-plane loading therefore this strong thermomechanical coupling effect should be taken into account in fracture analysis of SMAs. Based on this for future studies latent heat generation, especially when the load rate is high, should be taken into consideration.

The transformation region is calculated numerically and it is in good agreement with experimental results available in the literature. Using alternative approaches detailed analyses of fracture parameters of NiTi ate performed. For the first time a non-local stationary method is used to simulate a steady-state crack growth in an SMA and temperature distribution around the tip of a crack is obtained using a thermomechanically coupled algorithm.

Further studies of the discussed issues would be of interest. Clearly, further experiments might be needed to validate numerical methods proposed for the determination of fracture parameters. To quantify the effect of temperature increase around the crack tip due to latent heat generation high speed thermal camera measurements would be

very helpful. Several other questions remain to be addressed such as the effect of phase transformation on fatigue crack propagation. The dissipation through phase transformation may lead to an arrest of the propagating crack under fatigue loading. For this reason sub-critical crack growth under fatigue loading in an SMA specimen could be investigated. Transformation induced crack closure needs an experimental look to the problem as well.

REFERENCES

1. Abaqus, "UMAT and VUMAT routines for the simulation of Nitinol", Abaqus Inc., Pawtucket, RI, 2008.

2. Zaki, W. and Z. Moumni, "A Three-dimensional Model of the Thermomechanical Behavior of Shape Memory Alloys", *Journal of the Mechanics and Physics of Solids*, Vol.55, No. 11, pp. 2455–2490, 2007.

3. Auricchio, F., R. L. Taylor and J. Lubliner, "Shape-Memory Alloys: Macromodelling and Numerical Simulations of the Superelastic Behavior", *Computer Methods in Applied Mechanics and Engineering*, Vol.146, No. 3-4, pp. 281–312, 1997.

4. Ölander, A., "An Electrochemical Investigation of Solid Cadmium-gold Alloys", *Journal of the American Chemical Society*, Vol.54, No. 10, pp. 3819–3833, 1932.

5. Greninger, A. B. and V. G. Mooradian, "Strain Transformation in Metastable Copper- Zinc and Beta Copper-Tin Alloys", *Transactions of AIME*, Vol.128, pp. 337–368, 1938.

6. Buehler, W. J., J. V. Gilfrich and R. C. Wiley, "Effect of Low-Temperature Phase Changes on the Mechanical Properties of Alloys Near Composition TiNi", *Journal of Applied Physics*, Vol.34, No. 5, pp. 1475, 1963.

7. Buehler, W. J. and R. C. Wiley, "Nickel Base Alloys", United States Patent Office, Patent No:3174851, 1965.

8. Bhattacharya, K., *Why It Forms and How It Gives Rise to the Shape-Memory Effect*, Oxford University Press, 1998.

9. Otsuka, K. and C. M. Wayman, *Shape Memory Materials*, Cambridge University Press, 1998.

10. Tiyyagura, M., *Transmission Electron Microscopy Studies in Shape Memory Alloys*, Ph.D. Thesis, University of Central Florida, 2005.

11. ASTM, *Standard Test Method for Transformation Temperature of Nickel-titanium Alloys by Thermal Analysis*, volume 05, ASTM International, Standard Number F2004-05, 2004.

12. McMeeking, R. M. and A. G. Evans, "Mechanics of Transformation-toughening in Brittle Materials", *Fuel*, Vol.65, No. 5, pp. 242–246, 1981.

13. Eshelby, J. D., "The Determination of the Elastic Field of an Ellipsoidal Inclusion, and Related Problems", *Proceedings of the Royal Society A: Mathematical, Physical and Engineering Sciences*, Vol.241, No. 1226, pp. 376–396, 1957.

14. Stam, G. and E. van der ,Giessen, "Effect of Reversible Phase Transformations on Crack Growth", *Mechanics of Materials*, Vol.21, No. 1, pp. 51–71, 1995.

15. Sun, Q. and K. Hwang, "Micromechanics Modelling for the Constitutive Behavior of Polycrystalline Shape Memory Alloys—I. Derivation of General Relations", *Journal of the Mechanics and Physics of Solids*, Vol.41, No. I, 1993.

16. Sun, Q. and K. Hwang, "Micromechanics Modelling for the Constitutive Behavior of Polycrystalline Shape Memory Alloys—II. Study of the Individual Phenomena", *Journal of the Mechanics and Physics of Solids*, Vol.41, No. I, pp. 19–33, 1993.

17. Stam, G., E. van der ,Giessen and P. Meijers, "Effect of Transformation-induced Shear Strains on Crack Growth in Zirconia-containing Ceramics", *International Journal of Solids and Structures*, Vol.31, No. 14, pp. 1923–1948, 1994.

18. Birman, V., "On Mode I Fracture of Shape Memory Alloy Plates", *Smart Materials and Structures*, Vol.7, No. 4, pp. 433–437, 1998.

19. Tanaka, K., "A Thermomechanical Sketch of Shape Memory Effect: One-dimensional tensile Behavior", *Res Mechanica*, Vol.18, No. 3, pp. 251–263, 1986.

20. McKelvey, A. L. and R. O. Ritchie, "Fatigue-crack Propagation in Nitinol, a Shape-memory and Superelastic Endovascular Stent Material", *Journal of Biomedical Materials Research*, Vol.47, No. 3, pp. 301–308, 1999.

21. Simha, N., "Toughening by Phase Boundary Propagation", *Journal of Elasticity*, Vol.59, pp. 195–211, 2000.

22. Yi, S. and S. Gao, "Fracture Toughening Mechanism of Shape Memory Alloys Due to Martensite Transformation", *International Journal of Solids and Structures*, Vol.37, No. 38, pp. 5315–5327, 2000.

23. Evans, A. G., "Toughening Mechanisms in Zirconia Alloys", *Science and Technology of Zirconia II*, Vol.17, No. 15, pp. 193–212, 1983.

24. Yan, W., C. H. Wang, P. Z. Xin and Y. W. Mai, "Effect of Transformation Volume Contraction on the Toughness of Superelastic Shape Memory Alloys", *Smart Materials and Structures*, Vol.11, pp. 947–955, 2002.

25. Hutchinson, J. W., "On Steady Quasi-Static Crack Growth", Defense Technical Information Center, Technical Report, Report Number AF0SR-TR74-1042, 1974.

26. Yan, W., C. H. Wang, X. P. Zhang and Y.-W. W. Mai, "Theoretical Modelling of the Effect of Plasticity on Reverse Transformation in Superelastic Shape Memory Alloys", *Materials Science and Engineering A*, Vol.354, No. 1-2, pp. 146–157, 2003.

27. Lubliner, J. and F. Auricchio, "Generalized Plasticity and Shape Memory Alloys", *International Journal of Solids and Structures*, Vol.33, No. 7, pp. 991–1003, 1996.

28. Xiong, F., Y. Liu and E. Pagounis, "Fracture Mechanism of a Ni Mn Ga Ferromagnetic Shape Memory Alloy Single Crystal", *Journal of Magnetism and Magnetic Materials*, Vol.285, No. 3, pp. 410–416, 2005.

29. Wang, G., "Effects of Notch Geometry on Stress-strain Distribution, Martensite Transformation and Fracture Behavior in Shape Memory Alloy Niti", *Materials Science and Engineering: A*, Vol.434, No. 1-2, pp. 269–279, 2006.

30. Wang, G., "A Finite Element Analysis of Evolution of Stress–strain and Martensite Transformation in Front of a Notch in Shape Memory Alloy Niti", *Materials Science and Engineering: A*, Vol.460-461, pp. 383–391, 2007.

31. Wang, G. Z., "Effect of Martensite Transformation on Fracture Behavior of Shape Memory Alloy Niti in a Notched Specimen", *International Journal of Fracture*, Vol.146, No. 1-2, pp. 93–104, 2007.

32. ASTM, *Standard Test Method for Determination of Transformation Temperature of Nickel- Titanium Shape Memory Alloys by Bend and Free Recovery*, ASTM International, Standard Number F20082-06, 2014.

33. ASTM, *Standard Test Method for Tension Testing of Nickel-Titanium Superelastic Materials*, ASTM International, Standard Number F2516-07, 2014.

34. Wang, X., B. Xu, Z. Yue and X. Tong, "Fracture Behavior of the Compact Tension Specimens in Niti Shape Memory Alloys", *Materials Science and Engineering: A*, Vol.485, No. 1-2, pp. 14–19, 2008.

35. Robertson, S., A. Mehta, A. Pelton and R. Ritchie, "Evolution of Crack-tip Transformation Zones in Superelastic Nitinol Subjected to in Situ Fatigue: a Fracture Mechanics and Synchrotron X-ray Microdiffraction Analysis", *Acta Materialia*, Vol.55, No. 18, pp. 6198–6207, 2007.

36. Daly, S., A. Miller, G. Ravichandran and K. Bhattacharya, "An Experimental Investigation of Crack Initiation in Thin Sheets of Nitinol", *Acta Materialia*, Vol.55, No. 18, pp. 6322–6330, 2007.

37. Gollerthan, S., D. Herberg, A. Baruj and G. Eggeler, "Compact Tension Testing of Martensitic/pseudoplastic NiTi Shape Memory Alloys", *Materials Science and Engineering: A*, Vol.481-482, pp. 156–159, 2008.

38. ASTM, *Standard Test Method for Linear-Elastic Plane-Strain Fracture Toughness K(ic) of of Metallic Materials 399-12*, volume 399, ASTM International, Standard Number E399-12, 2013.

39. Xiong, F. and Y. Liu, "Effect of Stress-induced Martensitic Transformation on the Crack Tip Stress-intensity Factor in Ni–Mn– Ga Shape Memory Alloy", *Acta Materialia*, Vol.55, No. 16, pp. 5621–5629, 2007.

40. Tanaka, K. and Y. Sato, "Analysis of Superelastic Deformations During Isothermal Martensitic Transformation", *Res Mech.*, Vol.17, No. 3, pp. 241, 1986.

41. Freed, Y. and L. Banks-Sills, "Crack Growth Resistance of Shape Memory Alloys by Means of a Cohesive Zone Model", *Journal of the Mechanics and Physics of Solids*, Vol.55, pp. 2157–2180, 2007.

42. Panoskaltsis, V., S. Bahuguna and D. Soldatos, "On the Thermomechanical Modeling of Shape Memory Alloys", *International Journal of Non-Linear Mechanics*, Vol.39, No. 5, pp. 709–722, 2004.

43. Lexcellent, C. and F. Thiebaud, "Determination of the Phase Transformation Zone at a Crack Tip in a Shape Memory Alloy Exhibiting Asymmetry Between Tension and Compression", *Scripta Materialia*, Vol.59, No. 3, pp. 321–323, 2008.

44. Raniecki, B. and C. Lexcellent, "Thermodynamics of Isotropic Pseudoelasticity in Shape Memory Alloys", *European Journal of Mechanics - A/Solids*, Vol.17, No. 2, pp. 185–205, 1998.

45. Lexcellent, C. and P. Blanc, "Phase Transformation Yield Surface Determination for Some Shape Memory Alloys", *Acta Materialia*, Vol.52, No. 8, pp. 2317–2324, 2004.

46. Falvo, A., F. Furgiuele, A. Leonardi and C. Maletta, "Stress-Induced Martensitic Transformation in the Crack Tip Region of a NiTi Alloy", *Journal of Materials Engineering and Performance*, Vol.18, No. 5-6, pp. 679–685, 2009.

47. Ma, L., "Fundamental Formulation for Transformation Toughening", *International Journal of Solids and Structures*, Vol.47, No. 22-23, pp. 3214–3220, 2010.

48. Maletta, C. and F. Furgiuele, "Analytical Modeling of Stress-Induced Martensitic Transformation in the Crack Tip Region of Nickel–Titanium Alloys", *Acta Materialia*, Vol.58, No. 1, pp. 92–101, 2010.

49. Maletta, C. and M. L. Young, "Stress-Induced Martensite in Front of Crack Tips in NiTi Shape Memory Alloys: Modeling Versus Experiments", *Journal of Materials Engineering and Performance*, Vol.20, No. 4-5, pp. 597–604, 2011.

50. Gollerthan, S., M. Young, A. Baruj, J. Frenzel, W. Schmahl and G. Eggeler, "Fracture Mechanics and Microstructure in NiTi Shape Memory Alloys", *Acta Materialia*, Vol.57, No. 4, pp. 1015–1025, 2009.

51. Maletta, C. and F. Furgiuele, "Fracture Control Parameters for NiTi Based Shape Memory Alloys", *International Journal of Solids and Structures*, Vol.48, No. 11-12, pp. 1658–1664, 2011.

52. Baxevanis, T. and D. Lagoudas, "A Mode I Fracture Analysis of a Center-Cracked Infinite Shape Memory Alloy Plate Under Plane Stress", *International Journal of Fracture*, Vol.175, No. 2, pp. 151–166, 2012.

53. Dugdale, D., "Yielding of Steel Sheets Containing Slits", *Journal of the Mechanics and Physics of Solids*, Vol.8, No. 2, pp. 100–104, 1960.

54. Rice, J., *Fracture: An Advanced Treatise*, Academic Press, Chapter 3, pp. 191-311, 1968.

55. Baxevanis, T., Y. Chemisky and D. C. Lagoudas, "Finite Element Analysis of the Plane Strain Crack-Tip Mechanical Fields in Pseudoelastic Shape Memory Alloys", *Smart Materials and Structures*, Vol.21, No. 9, pp. 094012, 2012.

56. Lagoudas, D. C., Z. Bo and M. A. Qidwai, "A Unified Thermodynamic Constitutive Model for Sma and Finite Element Analysis of Active Metal Matrix Composites", *Mechanics of Composite Materials and Structures*, Vol.3, No. 2, pp. 153–179, 1996.

57. Simsek, M., *Fracture Mechanics Analysis of Shape Memory Alloys Using Finite Elements*, M.S. Thesis, Boğaziçi University, 2009.

58. Alkan, S., *Determination of Stress Distribution and Fracture Parameters Near Crack Tip for Shape Memory Alloy Plates*, M.S. Thesis, Boğaziçi University, 2013.

59. Yurtoglu, M., *Constitutive Modelling of Shape Memory Alloys and Its Implementation to Finite Elements*, M.S. Thesis, Boğaziçi University, 2011.

60. Altan, N. C., *Transformation Induced Crack Closure And Fatigue Life Analysis Of Shape Memory Alloys Using Finite Elements*, M.S. Thesis, Boğaziçi University, 2009.

61. Carnot, N., *Reflections on the Power of Heat*, John Wiley & Sons, New York, 1987.

62. Liang, C. and C. Rogers, "One-dimensional Thermomechanical Constitutive Relations for Shape Memory Materials", *Journal of Intelligent Material Systems and Structures*, Vol.1, No. 2, pp. 207–234, 1990.

63. Brinson, L., "One-Dimensional Constitutive Behavior of Shape Memory Alloys: Thermomechanical Derivation With Non-Constant Material Functions and Redefined Martensite Internal Variable", *Journal of Intelligent Material Systems and Structures*, Vol.4, No. 2, pp. 229–242, 1993.

64. Abeyaratne, R. and J. K. Knowles, "A Continuum Model of a Thermoelastic Solid Capable of Undergoing Phase Transitions", *Journal of the Mechanics and Physics of Solids*, Vol.41, No. 3, pp. 541–571, 1993.

65. Rajagopal, K. R. and A. R. Srinivasa, "On the Thermomechanics of Shape Memory Wires", *Zeitschrift für Angewandte Mathematik und Physik ZAMP*, Vol.50, No. 3, pp. 459–496, 1999.

66. Paiva, A., M. A. Savi, A. M. B. Braga and P. M. C. L. Pacheco, "A Constitutive Model for Shape Memory Alloys Considering Tensile–compressive Asymmetry and Plasticity", *International Journal of Solids and Structures*, Vol.42, No. 11-12, pp. 3439–3457, 2005.

67. Hall, G. J. and S. Govindjee, "Application of a Partially Relaxed Shape Memory Free Energy Function to Estimate the Phase Diagram and Predict Global Microstructure Evolution", *Journal of the Mechanics and Physics of Solids*, Vol.50, No. 3, pp. 501–530, 2002.

68. Juhász, L., E. Schnack, O. Hesebeck and H. Andrä, "Macroscopic Modeling of Shape Memory Alloys Under Non-Proportional Thermo-mechanical Loadings",

Journal of Intelligent Materials Systems and Structures, Vol.13, No. 12, pp. 825–836, 2002.

69. Savi, M. A. and A. Paiva, "Describing Internal Subloops Due to Incomplete Phase Transformations in Shape Memory Alloys", *Archive of Applied Mechanics*, Vol.74, No. 9, pp. 637–647, 2005.

70. Liang, C. and C. A. Rogers, "A Multi-dimensional Constitutive Model for Shape Memory Alloys", *Journal of Engineering Mathematics*, Vol.26, No. 3, pp. 429–443, 1992.

71. Leclercq, S. and C. Lexcellent, "A General Macroscopic Description of the Thermomechanical Behavior of Shape Memory Alloys", *Journal of the Mechanics and Physics of Solids*, Vol.44, No. 6, pp. 953–980, 1996.

72. Govindjee, S. and C. Miehe, "A Multi-Variant Martensitic Phase Transformation Model: Formulation and Numerical Implementation", *Computer Methods in Applied Mechanics and Engineering*, Vol.191, No. 3-5, pp. 215–238, 2001.

73. Helm, D. and P. Haupt, "Shape Memory Behaviour: Modelling Within Continuum Thermomechanics", *International Journal of Solids and Structures*, Vol.40, No. 4, pp. 827–849, 2003.

74. Shaw, J. A., "A Thermomechanical Model for a 1-d Shape Memory Alloy Wire with Propagating Instabilities", *International Journal of Solids and Structures*, Vol.39, No. 5, pp. 1275–1305, 2002.

75. Reese, S. and D. Christ, "Finite Deformation Pseudo-elasticity of Shape Memory Alloys – Constitutive Modelling and Finite Element Implementation", *International Journal of Plasticity*, Vol.24, No. 3, pp. 455–482, 2008.

76. Patoor, E., A. Ererhardt and M. Berveiller, "Thermomechanical Behavior by Martensitic Transformation in Single and Polycrystals of Metallic Alloys", *Revue de Physique Appliquée*, Vol.23, No. 4, pp. 702–702, 1988.

77. Boyd, J. G. and D. C. Lagoudas, "A Thermodynamical Constitutive Model for

Shape Memory Materials. Part I. the Monolithic Shape Memory Alloy", *International Journal of Plasticity*, Vol.12, No. 6, pp. 805–842, 1996.

78. Bo, Z. and D. C. Lagoudas, "Thermomechanical Modeling of Polycrystalline SMAs Under Cyclic Loading, Part I: Theoretical Derivations", *International Journal of Engineering Science*, Vol.37, No. 9, pp. 1089–1140, 1999.

79. Lagoudas, D. C. and Z. Bo, "Thermomechanical Modeling of Polycrystalline Smas under Cyclic Loading, Part II: Material Characterization and Experimental Results for a Stable Transformation Cycle", *International Journal of Engineering Science*, Vol.37, No. 9, pp. 1141–1173, 1999.

80. Bo, Z. and D. C. Lagoudas, "Thermomechanical Modeling of Polycrystalline SMAs Under Cyclic Loading, Part III: Evolution of Plastic Strains and Two-Way Shape Memory Effect", *International Journal of Engineering Science*, Vol.37, No. 9, pp. 1175–1203, 1999.

81. Bo, Z. and D. C. Lagoudas, "Thermomechanical Modeling of Polycrystalline SMAs Under Cyclic Loading, Part IV: Modeling of Minor Hysteresis Loops", *International Journal of Engineering Science*, Vol.37, No. 9, pp. 1205–1249, 1999.

82. Lagoudas, D. C. and P. B. Entchev, "Modeling of Transformation-induced Plasticity and Its Effect on the Behavior of Porous Shape Memory Alloys. Part I: Constitutive Model for Fully Dense Smas", *Mechanics of Materials*, Vol.36, No. 9, pp. 865–892, 2004.

83. Popov, P. and D. C. Lagoudas, "A 3-D Constitutive Model for Shape Memory Alloys Incorporating Pseudoelasticity and Detwinning of Self-accommodated Martensite", *International Journal of Plasticity*, Vol.23, No. 10-11, pp. 1679–1720, 2007.

84. Bowles, J. and J. Mackenzie, "The Crystallography of Martensite Transformations I", *Acta Metallurgica*, Vol.2, No. 1, pp. 129–137, 1954.

85. Wechsler, M. S., D. S. Lieberman and T. A. Read, "On the Theory of the Formation of Martensite", *Journal of Metals*, Vol.197, pp. 1503–1515, 1953.

86. Ball, J. M. and R. D. James, "Fine Phase Mixtures as Minimizers of Energy", *Archive for Rational Mechanics and Analysis*, Vol.100, No. 1, pp. 13–52, 1987.

87. Enkovaara, J., *Atomistic Simulation of Magnetic Shape Memory Alloys*, volume 119, Helsinki University of Technology, 2003.

88. Hildebrand, F. and R. Abeyaratne, "An Atomistic Investigation of the Kinetics of Detwinning", *Journal of the Mechanics and Physics of Solids*, Vol.56, No. 4, pp. 1296–1319, 2008.

89. Kibey, S., *Mesoscale Models for Stacking Faults, Deformation Twins and Martensitic Transformations: Linking Atomistics to Continuum*, Ph.D. Thesis, University of Illinois at Urbana-Champaign, 2007.

90. Chan, C., S. Chan, H. Man and P. Ji, "1-D Constitutive Model for Evolution of Stress-Induced R-Phase and Localized Lüders-Like Stress-Induced Martensitic Transformation of Super-Elastic NiTi Wires", *International Journal of Plasticity*, Vol.32-33, pp. 85–105, 2012.

91. Auricchio, F. and E. Sacco, "A One-Dimensional Model for Superelastic Shape-Memory Alloys With Different Elastic Properties Between Austenite and Martensite", *International Journal of Non-Linear Mechanics*, Vol.32, No. 6, pp. 1101–1114, 1997.

92. Kamita, T. and Y. Matsuzaki, "One-Dimensional Pseudoelastic Theory of Shape Memory Alloys", *Smart Materials and Structures*, Vol.7, No. 4, pp. 489–495, 1998.

93. Govindjee, S. and E. P. Kasper, "Computational Aspects of One-Dimensional Shape Memory Alloy Modeling With Phase Diagrams", *Computer Methods in Applied Mechanics and Engineering*, Vol.171, No. 3-4, pp. 309–326, 1999.

94. Song, Y. and S. Liu, "One-dimensional Tensile Constitutive Equation Cannot Be Directly Generalized to Deal with Two-dimensional Bulging Mechanical Problems", *Science in China Series E: Technological Sciences*, Vol.45, No. 6, 2002.

95. Chrysochoos, A., C. Licht and R. Peyroux, "Une Modélisation Thermomécanique Unidimensionnelle de la Propagation d'un Front de Changement de Phase dans

un Monocristal d'AMF", *Comptes Rendus Mécanique*, Vol.331, No. 1, pp. 25–32, 2003.

96. Falk, F. and P. Konopka, "Three-Dimensional Landau Theory Describing the Martensitic Phase Transformation of Shape-Memory Alloys", *Journal of Physics: Condensed Matter*, Vol.2, No. 1, pp. 61–77, 1990.

97. Achenbach, M., "A Model for an Alloy With Shape Memory", *International Journal of Plasticity*, Vol.5, No. 4, pp. 371–395, 1989.

98. Koistinen, D. and R. Marburger, "A General Equation Prescribing the Extent of the Austenite-martensite Transformation in Pure Iron-carbon Alloys and Plain Carbon Steels", *Acta Metallurgica*, Vol.7, No. 1, pp. 59–60, 1959.

99. Patoor, E., A. Eberhardt and M. Berveiller, "Micromechanical Modelling of Superelasticity in Shape Memory Alloys", *Le Journal de Physique IV*, Vol.06, No. C1, pp. C1–277–C1–292, 1996.

100. Gall, K. and H. Sehitoglu, "The Role of Texture in Tension–compression Asymmetry in Polycrystalline NiTi", *International Journal of Plasticity*, Vol.15, No. 1, pp. 69–92, 1999.

101. Patoor, E., M. El Amrani, A. Eberhardt and M. Berveiller, "Determination of the Origin for the Dissymmetry Observed Between Tensile and Compression Tests on Shape Memory Alloys", *Le Journal de Physique IV*, Vol.05, No. C2, pp. C2–495–C2–500, 1995.

102. Arghavani, J., F. Auricchio, R. Naghdabadi, A. Reali and S. Sohrabpour, "A 3-D Phenomenological Constitutive Model for Shape Memory Alloys Under Multiaxial Loadings", *International Journal of Plasticity*, Vol.26, No. 7, pp. 976–991, 2010.

103. Gao, X., M. Huang and L. Brinson, "A Multivariant Micromechanical Model for SMAs Part 1. Crystallographic Issues for Single Crystal Model", *International Journal of Plasticity*, Vol.16, No. 10-11, pp. 1345–1369, 2000.

104. Oliveira, S. A., M. A. Savi and A. L. Kalamkarov, "A Three-dimensional

Constitutive Model for Shape Memory Alloys", *Archive of Applied Mechanics*, Vol.80, No. 10, pp. 1163–1175, 2010.

105. Saleeb, A., S. Padula and A. Kumar, "A Multi-axial, Multimechanism Based Constitutive Model for the Comprehensive Representation of the Evolutionary Response of Smas under General Thermomechanical Loading Conditions", *International Journal of Plasticity*, Vol.27, No. 5, pp. 655–687, 2011.

106. Luo, J., M. Li, X. Li and Y. Shi, "Constitutive Model for High Temperature Deformation of Titanium Alloys Using Internal State Variables", *Mechanics of Materials*, Vol.42, No. 2, pp. 157–165, 2010.

107. Brocca, M., L. Brinson and Z. Bažant, "Three-Dimensional Constitutive Model for Shape Memory Alloys Based on Microplane Model", *Journal of the Mechanics and Physics of Solids*, Vol.50, No. 5, pp. 1051–1077, 2002.

108. Auricchio, F., A. Reali and U. Stefanelli, "A Three-Dimensional Model Describing Stress-Induced Solid Phase Transformation With Permanent Inelasticity", *International Journal of Plasticity*, Vol.23, No. 2, pp. 207–226, 2007.

109. Wang, X. and Z. Yue, "Three-dimensional Thermomechanical Modeling of Pseudoelasticity in Shape Memory Alloys with Different Elastic Properties Between Austenite and Martensite", *Materials Science and Engineering: A*, Vol.425, No. 1-2, pp. 83–93, 2006.

110. Souza, A. C., E. N. Mamiya and N. Zouain, "Three-dimensional Model for Solids Undergoing Stress-induced Phase Transformations", *European Journal of Mechanics - A/Solids*, Vol.17, No. 5, pp. 789–806, 1998.

111. Zhang, Y., Y.-T. Cheng and D. S. Grummon, "Finite Element Modeling of Indentation-Induced Superelastic Effect Using a Three-dimensional Constitutive Model for Shape Memory Materials with Plasticity", *Journal of Applied Physics*, Vol.101, No. 5, pp. 053507–053513, 2007.

112. Zhou, B., S. H. Yoon and J. S. Leng, "A Three-dimensional Constitutive Model for Shape Memory Alloy", *Smart Materials and Structures*, Vol.18, No. 9, pp. 95016, 2009.

113. Tanaka, K. and R. Iwasaki, "A Phenomenological Theory of Transformation Superplasticity", *Engineering Fracture Mechanics*, Vol.21, No. 4, pp. 709–720, 1985.

114. Tanaka, K. and Al., "Phenomenological Analysis on Subloops and Cyclic Behavior in Shape Memory Alloys under Mechanical and/or Thermal Loads", *Mechanics of Materials*, Vol.19, pp. 281–292, 1995.

115. Tanaka, K. and S. Nagaki, "A Thermomechanical Description of Materials with Internal Variables in the Process of Phase Transitions", *Archive of Applied Mechanics*, Vol.51, No. 5, pp. 287–299, 1982.

116. Halphen, B. and Q. S. Nguyen, "Plastic and Visco-plastic Materials with Generalized Potential", *Mechanics Research Communications*, Vol.1, No. 1, pp. 43–47, 1974.

117. Moumni, Z., *Sur la Modelisation du Changement de Phase Solide : Application aux Materiaux a Memorie de forme et a l'endommagement fragile partiel*, Ph.D. Thesis, École Nationale des Ponts et Chaussées, 1995.

118. Moumni, Z., W. Zaki and Q. S. Nguyen, "Theoretical and Numerical Modeling of Solid–solid Phase Change: Application to the Description of the Thermomechanical Behavior of Shape Memory Alloys", *International Journal of Plasticity*, Vol.24, No. 4, pp. 614–645, 2008.

119. Morin, C., Z. Moumni and W. Zaki, "Thermomechanical Coupling in Shape Memory Alloys under Cyclic Loadings: Experimental Analysis and Constitutive Modeling", *International Journal of Plasticity*, Vol.27, No. 12, pp. 1959–1980, 2011.

120. Morin, C., Z. Moumni and W. Zaki, "A Constitutive Model for Shape Memory Alloys Accounting for Thermomechanical Coupling", *International Journal of Plasticity*, Vol.27, No. 5, pp. 748–767, 2011.

121. Zaki, W. and Z. Moumni, "A 3D Model of the Cyclic Thermomechanical Behavior of Shape Memory Alloys", *Journal of the Mechanics and Physics of Solids*, Vol.55, No. 11, pp. 2427–2454, 2007.

122. Zaki, W., "An Approach to Modeling Tensile-compressive Asymmetry for Martensitic Shape Memory Alloys", *Smart Materials and Structures*, Vol.19, No. 2, pp. 025009–025026, 2010.

123. Zaki, W., S. Zamfir and Z. Moumni, "An Extension of the Zm Model for Shape Memory Alloys Accounting for Plastic Deformation", *Mechanics of Materials*, Vol.42, No. 3, pp. 266–274, 2010.

124. Coleman, B. D., "Thermodynamics with Internal State Variables", *The Journal of Chemical Physics*, Vol.47, No. 2, pp. 597, 1967.

125. Morin, C., *A Comprehensive Approach for Fatigue Analysis of Shape Memory Alloys*, Ph.D. Thesis, Ecole Polytechnique, 2011.

126. Van Humbeeck, J., "Non-medical Applications of Shape Memory Alloys", *Materials Science and Engineering: A*, Vol.273-275, pp. 134–148, 1999.

127. Kauffman, G. B. and I. Mayo, "The Story of Nitinol: the Serendipitous Discovery of the Memory Metal and Its Applications", *The Chemical Educator*, Vol.2, No. 2, pp. 1–21, 1997.

128. Abadie, J., N. Chaillet and C. Lexcellent, "Modeling of a new SMA micro-actuator for active endoscopy applications", *Mechatronics*, Vol.19, No. 4, pp. 437–442, 2009.

129. Song, G., N. Ma and H.-N. Li, "Applications of Shape Memory Alloys in Civil Structures", *Engineering Structures*, Vol.28, No. 9, pp. 1266–1274, 2006.

130. Fugazza, D., *Shape-Memory Alloy Devices for Earthquake Engineering: Mechanical Properties, Constitutive Modeling and Numerical Simulations*, M.S. Thesis, Rose School, Pavia, Italy, 2003.

131. Lagoudas, D. C., *Shape Memory Alloys*, Springer US, Boston, MA, 2008.

132. Fremond, M., "Matériaux à Mémoire de Forme", *Comptes rendus de l'Académie des sciences. Série 2, Mécanique, Physique, Chimie, Sciences de l'univers, Sciences de la Terre*, Vol.304, No. 7, pp. 239–244.

133. Moreau, J. J., *New Variational Techniques in Mathematical Physics*, Springer, 2011.

134. Irwin, G., *Plastic Zone Near a Crack and Fracture Toughness*, Proceedings of 7th Sagamore Conference, Raquette Lake, New York, pp.63-76, 1961.

135. Barenblatt, G. I., "The Mathematical Theory of Equilibrium Cracks in Brittle Fracture", *Advances in Applied Mechanics*, Vol.7, pp. 55–129, 1962.

136. Bulbich, A. A., "Nucleation on the Crack Tip and Transformation Toughness in Crystals Undergoing Structural Phase Transitions", *Journal of Materials Science*, Vol.27, No. 4, pp. 1070–1080, 1992.

137. Wang, X., Y. Wang, A. Baruj, G. Eggeler and Z. Yue, "On the Formation of Martensite in Front of Cracks in Pseudoelastic Shape Memory Alloys", *Materials Science and Engineering: A*, Vol.394, No. 1-2, pp. 393–398, 2005.

138. Daly, S. H. *Deformation and Fracture of Thin Sheets of Nitinol*. PhD Thesis, California Institute of Technology, 2007.

139. Lexcellent, C., M. R. Laydi and V. Taillebot, "Analytical Prediction of the Phase Transformation Onset Zone at a Crack Tip of a Shape Memory Alloy Exhibiting Asymmetry Between Tension and Compression", *International Journal of Fracture*, Vol.169, No. 1, pp. 1–13, 2010.

140. Taillebot, V., C. Lexcellent and P. Vacher, "About the Transformation Phase Zones of Shape Memory Alloys' Fracture Tests on Single Edge-cracked Specimen", *Functional Materials Letters*, Vol.05, No. 01, pp. 1250007–12500012, 2012.

141. Du, Z. and J. Hancock, "The Effect of Non-Singular Stresses on Crack-Tip Constraint", *Journal of the Mechanics and Physics of Solids*, Vol.39, No. 4, pp. 555–567, 1991.

142. Carka, D. and C. M. Landis, "On the Path-Dependence of the J-Integral Near a Stationary Crack in an Elastic-Plastic Materiall", *Journal of Applied Mechanics*, Vol.78, No. 1, pp. 011006–011009, 2011.

143. Young, M., S. Gollerthan, A. Baruj, J. Frenzel, W. Schmahl and G. Eggeler, "Strain Mapping of Crack Extension in Pseudoelastic Niti Shape Memory Alloys During Static Loading", *Acta Materialia*, Vol.61, No. 15, pp. 5800–5806, 2013.

144. Williams, M. L., "On the Stress Distribution at the Base of a Stationary Crack", *Journal of Applied Mechanics*, Vol.24, pp. 109–114, 1957.

145. Oral, A., J. Lambros and G. Anlas, "Crack Initiation in Functionally Graded Materials under Mixed Mode Loading: Experiments and Simulations", *Journal of Applied Mechanics*, Vol.75, No. 5, pp. 051110–051118, 2008.

146. Pelton, A., J. Dicello and S. Miyazaki. "Optimisation of Processing and Properties of Medical Grade Nitinol Wire". In *Proceedings of the International Conference on Shape Memory and Superelastic Technologies*. SMST, 2000.

147. Anderson TL, *Fracture Mechanics: Fundamentals and Applications*, CRC Press, 3rd ed. edition, 2004.

148. Paris, P. C., R. M. McMeeking and H. Tada, "The Weight Function Method for Determining Stress Intensity Factors", *Cracks and Fracture, ASTM STP*, Vol.601, pp. 471–489, 1976.

149. Yi, S., S. Gao and L. Shen, "Fracture Toughening Mechanism of Shape Memory Alloys under Mixed-mode Loading Due to Martensite Transformation", *International Journal of Solids and Structures*, Vol.38, No. 24-25, pp. 4463–4476, 2001.

150. Rice, J. R., "A Path Independent Integral and the Approximate Analysis of Strain Concentration by Notches and Cracks", *Journal of Applied Mechanics*, Vol.35, No. 2, pp. 379, 1968.

151. Rice, J. and G. Rosengren, "Plane Strain Deformation near a Crack Tip in a Power-law Hardening Material", *Journal of the Mechanics and Physics of Solids*, Vol.16, No. 1, pp. 1–12, 1968.

152. Jin, Z. and R. Batra, "Some Basic Fracture Mechanics Concepts in Functionally Graded Materials", *Journal of the Mechanics and Physics of Solids*, Vol.44, No. 8, pp. 1221–1235, 1996.

153. Anlas, G., M. Santare and J. Lambros, "Numerical Calculation of Stress Intensity Factors in Functionally Graded Materials", *International Journal of Fracture*, Vol.104, No. 2, pp. 131–143, 2000.

154. Shih, C. F., "Relationships Between the J-integral and the Crack Opening Displacement for Stationary and Extending Cracks", *Journal of the Mechanics and Physics of Solids*, Vol.29, No. 4, pp. 305–326, 1981.

155. Hoffmann, M. and T. Seeger, *Dugdale Solutions for Strain Hardening Materials*, Springer, Berlin, Heidelberg, 1986.

156. Schwalbe, K.-H., *The Prediction of Failure Situations Using the Ctod Concept Based on the Engineering Treatment Model (ETM)*, Springer, 1986.

157. Woo, C. and C. Chow. "Finite Element Analysis of Crack Instability". In *Numerical Methods in Fracture Mechanics, Proceeding of the Second International Conference*, Swansea, Wales, pp. 83-92, 1980.

158. Parks, D., "The Virtual Crack Extension Method for Nonlinear Material Behavior", *Computer Methods in Applied Mechanics and Engineering*, Vol.12, No. 3, pp. 353–364, 1977.

159. Hellen, T. K., "On the Method of Virtual Crack Extensions", *International Journal for Numerical Methods in Engineering*, Vol.9, No. 1, pp. 187–207, 1975.

160. López, H., "Transformation Induced Toughening in a Ni–Ti 52 Shape Memory Alloy", *Materials Letters*, Vol.51, No. 2, pp. 144–150, 2001.

161. Chen, J. H., G. Z. Wang and W. Sun, "Investigation on the Fracture Behavior of Shape Memory Alloy NiTi", *Metallurgical and Materials Transactions A*, Vol.36, No. 4, pp. 941–955, 2005.

162. Robertson, S. W. and R. O. Ritchie, "A Fracture-mechanics-based Approach to Fracture Control in Biomedical Devices Manufactured from Superelastic Nitinol Tube", *Journal of Biomedical Materials Research Part B: Applied Biomaterials*, Vol.84, No. 1, pp. 26–33, 2008.

163. Baxevanis, T., A. Parrinello and D. Lagoudas, "On the Fracture Toughness Enhancement Due to Stress-Induced Phase Transformation in Shape Memory Alloys", *International Journal of Plasticity*, Vol.50, pp. 158–169, 2013.

164. Dauskardt, R., T. Duerig and R. Ritchie, "Effects of In Situ Phase Transformation on Fatigue-Crack Propagation in Titanium–Nickel Shape-Memory Alloys", *Proceedings of the MRS International Meeting*, Vol.9, pp. 243–249, 1988.

165. Mehta, a., V. Imbeni, R. Ritchie and T. Duerig, "On the Electronic and Mechanical Instabilities in Ni50.9Ti49.1", *Materials Science and Engineering: A*, Vol.378, No. 1-2, pp. 130–137, 2004.

166. Holtz, R., K. Sadananda and M. A. Imam, "Fatigue Thresholds of Ni-Ti Alloy Near the Shape Memory Transition Temperature", *International Journal of Fatigue*, Vol.21, No. Supplement 1, pp. 137–145, 1999.

167. Jackson, C., "55-Nitinol-the Alloy with a Memory: It's Physical Metallurgy Properties, and Applications", *NASA Special Publication*, Vol.SP-5110, 1972.

168. Robertson, S. W. *On the Mechanical Properties and Microstructure of Nitinol for Biomedical Stent Applications*. PhD Thesis, University of California, Berkeley, 2006.

169. Varias, A. and C. Shih, "Quasi-static Crack Advance under a Range of Constraints—steady-state Fields Based on a Characteristic Length", *Journal of the Mechanics and Physics of Solids*, Vol.41, No. 5, pp. 835–861, 1993.

170. Tvergaard, V., "Effect of T-stress on Crack Growth under Mixed Mode I–iii Loading", *International Journal of Solids and Structures*, Vol.45, No. 18-19, pp. 5181–5188, 2008.

171. Hellmann, D. and K.-H. Schwalbe, *On the Experimental Determination of CTOD Based R-Curves*, Springer, Berlin, Heidelberg, 1986.

172. Dean, R. H. and J. W. Hutchinson, "Quasi-Static Steady Crack Growth in Small Scale Yielding", *Fracture Mechanics: 12th Conference, ASTM*, Vol.STP 700, pp. 383–405, 1980.

173. Rice, J. R., W. J. Drugan and T. L. Sham, "Elastic Plastic Analysis of Growing Cracks", *Fracture Mechanics: Twelfth Conference, ASTM*, Vol.STP 700, pp. 189–221, 1979.

174. Stahle, P., "Easy Adaptation of a Commercial Fem Code for Self-similarity", *Communications in Numerical Methods in Engineering*, Vol.11, pp. 117–125, 1995.

175. Niordson, C., "Analysis of Steady-state Ductile Crack Growth along a Laser Weld", *International Journal of Fracture*, Vol.111, pp. 53–69, 2001.

176. Landis, C. M., "On the Fracture Toughness of Ferroelastic Materials", *Journal of the Mechanics and Physics of Solids*, Vol.51, No. 8, pp. 1347–1369, 2003.

177. Landis, C. M., "On the Fracture Toughness Anisotropy of Mechanically Poled Ferroelectric Ceramics", *International Journal of Fracture*, Vol.126, No. 1, pp. 1–16, 2004.

178. Sheng, J. and C. M. Landis, "Toughening Due to Domain Switching in Single Crystal Ferroelectric Materials", *International Journal of Fracture*, Vol.143, No. 2, pp. 161–175, 2007.

179. Martiny, P., F. Lani, A. Kinloch and T. Pardoen, "Numerical Analysis of the Energy Contributions in Peel Tests: a Steady-state Multilevel Finite Element Approach", *International Journal of Adhesion and Adhesives*, Vol.28, No. 4-5, pp. 222–236, 2008.

180. Martiny, P., F. Lani, A. Kinloch and T. Pardoen, "A Maximum Stress at a Distance Criterion for the Prediction of Crack Propagation in Adhesively-bonded Joints", *Engineering Fracture Mechanics*, Vol.97, pp. 105–135, 2013.

181. Nielsen, K., C. Niordson and J. Hutchinson, "Strain Gradient Effects on Steady State Crack Growth in Rate-sensitive Materials", *Engineering Fracture Mechanics*, Vol.96, pp. 61–71, 2012.

182. Nielsen, K. and C. Niordson, "Rate Sensitivity of Mixed Mode Interface Toughness of Dissimilar Metallic Materials: Studied at Steady State", *International Journal of Solids and Structures*, Vol.49, No. 3-4, pp. 576–583, 2012.

183. Sobotka, J. C. and R. H. Dodds, "Steady Crack Growth in a Thin, Ductile Plate under Small-scale Yielding Conditions: Three-dimensional Modeling", *Engineering Fracture Mechanics*, Vol.78, pp. 343–363, 2011.

184. Baxevanis, T., C. M. Landis and D. C. Lagoudas, "On the Fracture Toughness of Pseudoelastic Shape Memory Alloys", *Journal of Applied Mechanics*, Vol.81, No. 4, pp. 041005–041013, 2013.

185. Nguyen, Q. and M. Rahimian, "Mouvement Permanent d'une Fissure En Milieu elastoplastique", *Journal de Mécanique appliquée*, Vol.5, pp. 95–120, 1981.

186. Van, K. and M. Maitournam, "Steady-state Flow in Classical Elastoplasticity: Applications to Repeated Rolling and Sliding Contact", *Journal of the Mechanics and Physics of Solids*, Vol.41, No. 1981, 1993.

187. Nguyen-Tajan, T., H. Maitournam and Thomas Jean-Jacques, "Une Méthode de Calcul de Structures Soumises à des Chargements Mobiles", *Revue Européenne des Éléments*, Vol.11, pp. 247–261, 2002.

188. Lê Minh, B., M. Maitournam and V. Doquet, "A Cyclic Steady-state Method for Fatigue Crack Propagation: Evaluation of Plasticity-induced Crack Closure in 3D", *International Journal of Solids and Structures*, Vol.49, No. 17, pp. 2301–2313, 2012.

189. Sun, Q. P., K. C. Hwang and S. W. Yu, "A Micromechanics Constitutive Model of Transformation Plasticity with Shear and Dilatation Effect", *Journal of the Mechanics and Physics of Solids*, Vol.39, pp. 507–524, 1991.

190. Gollerthan, S., M. Young, K. Neuking, U. Ramamurty and G. Eggeler, "Direct Physical Evidence for the Back-Transformation of Stress-Induced Martensite in the Vicinity of Cracks in Pseudoelastic NiTi Shape Memory Alloys", *Acta Materialia*, Vol.57, No. 19, pp. 5892–5897, 2009.

191. McNaney, J., V. Imbeni, Y. Jung, P. Papadopoulos and R. Ritchie, "An Experimental Study of the Superelastic Effect in a Shape-memory Nitinol Alloy under Biaxial Loading", *Mechanics of Materials*, Vol.35, No. 10, pp. 969–986, 2003.

192. Grabe, C. and O. Bruhns, "Path Dependence and Multiaxial Behavior of a Polycrystalline NiTi Alloy Within the Pseudoelastic and Pseudoplastic Temperature Regimes", *International Journal of Plasticity*, Vol.25, No. 3, pp. 513–545, 2009.

193. Chemisky, Y., A. Duval, E. Patoor and T. Ben Zineb, "Constitutive Model for Shape Memory Alloys Including Phase Transformation, Martensitic Reorientation and Twins Accommodation", *Mechanics of Materials*, Vol.43, No. 7, pp. 361–376, 2011.

194. Pan, H., P. Thamburaja and F. Chau, "Multi-axial Behavior of Shape-memory Alloys Undergoing Martensitic Reorientation and Detwinning", *International Journal of Plasticity*, Vol.23, No. 4, pp. 711–732, 2007.

195. Liu, Y., D. Favier and L. Orgeas, "Mechanistic Simulation of Martensite Reorientation Deformation of Polycrystalline Niti", *Smart Materials and Structures*, Vol.14, No. 5, pp. S207–S210, 2005.

196. Sedlák, P., M. Frost, B. Benešová, T. Ben Zineb and P. Šittner, "Thermomechanical Model for Niti-based Shape Memory Alloys Including R-phase and Material Anisotropy under Multi-axial Loadings", *International Journal of Plasticity*, Vol.39, pp. 132–151, 2012.

197. Piotrowski, B., T. Ben Zineb, E. Patoor and A. Eberhardt, "Modeling of Niobium Precipitates Effect on the Ni47ti44nb9 Shape Memory Alloy Behavior", *International Journal of Plasticity*, Vol.36, pp. 130–147, 2012.

198. Yu, C., G. Kang and Q. Kan, "Crystal Plasticity Based Constitutive Model of Niti Shape Memory Alloy Considering Different Mechanisms of Inelastic Deformation", *International Journal of Plasticity*, Vol.54, pp. 132–162, 2014.

199. Zaki, W., "Time Integration of a Model for Martensite Detwinning and Reorientation under Nonproportional Loading Using Lagrange Multipliers", *International Journal of Solids and Structures*, Vol.49, No. 21, pp. 2951–2961, 2012.

200. Zaki, W., "An Efficient Implementation for a Model of Martensite Reorientation in Martensitic Shape Memory Alloys under Multiaxial Nonproportional Loading", *International Journal of Plasticity*, Vol.37, pp. 72–94, 2012.

201. Sehitoglu, H., J. Wang and H. Maier, "Transformation and Slip Behavior of Ni2fega", *International Journal of Plasticity*, Vol.39, pp. 61–74, 2012.

202. Wang, J., H. Sehitoglu and H. Maier, "Dislocation Slip Stress Prediction in Shape Memory Alloys", *International Journal of Plasticity*, Vol.54, pp. 247–266, 2014.

203. Yu, C., G. Kang, Q. Kan and D. Song, "A Micromechanical Constitutive Model Based on Crystal Plasticity for Thermo-mechanical Cyclic Deformation of Niti Shape Memory Alloys", *International Journal of Plasticity*, Vol.44, pp. 161–191, 2013.

204. Kato, H. and K. Sasaki, "Transformation-Induced Plasticity As the Origin of Serrated Flow in an NiTi Shape Memory Alloy", *International Journal of Plasticity*, Vol.50, pp. 37–48, 2013.

205. Rice, J. R. "The Mechanics of Quasi-static Crack Growth". In *Proceedings of the Eighth U.S. National Congress of Applied Mechanics*. University of California Los Angeles, pp. 191-216, 1979.

206. Rice, J. R. and E. P. Sorensen, "Continuing Crack-tip Deformation and Fracture for Plane-strain Crack Growth in Elastic-plastic Solids", *Journal of the Mechanics and Physics of Solids*, Vol.26, pp. 163–186, 1978.

207. McKelvey, A. L. and R. O. Ritchie, "Fatigue-crack Growth Behavior in the Superelastic and Shape-memory Alloy Nitinol", *Metallurgical and Materials Transactions A*, Vol.32, No. 3, pp. 731–743, 2001.

208. Lagoudas, D. C., P. B. Entchev, P. Popov, E. Patoor, L. C. Brinson and X. Gao, "Shape Memory Alloys, Part II: Modeling of Polycrystals", *Mechanics of Materials*, Vol.38, No. 5-6, pp. 430–462, 2006.

209. Budiansky, B., J. W. Hutchinson and J. C. Lambropoulos, "Continuum Theory of Dilatant Transformation Toughening in Ceramics", *International Journal of Solids and Structures*, Vol.19, pp. 337–355, 1983.

210. Simha, N., F. Fischer, G. Shan, C. Chen and O. Kolednik, "J-integral and Crack

Driving Force in Elastic–plastic Materials", *Journal of the Mechanics and Physics of Solids*, Vol.56, No. 9, pp. 2876–2895, 2008.

211. Kolednik, O., J. Predan, G. Shan, N. Simha and F. Fischer, "On the Fracture Behavior of Inhomogeneous Materials—a Case Study for Elastically Inhomogeneous Bimaterials", *International Journal of Solids and Structures*, Vol.42, No. 2, pp. 605–620, 2005.

212. Zaki, W., Z. Moumni and C. Morin, "Modeling Tensile-compressive Asymmetry for Superelastic Shape Memory Alloys", *Mechanics of Advanced Materials and Structures*, Vol.18, No. 7, pp. 559–564, 2011.

213. Moussa, M. O., Z. Moumni, O. Doare, C. Touze and W. Zaki, "Non-linear Dynamic Thermomechanical Behaviour of Shape Memory Alloys", *Journal of Intelligent Material Systems and Structures*, Vol.23, No. 14, pp. 1593–1611, 2012.

214. Moumni, Z., W. Zaki and H. Maitournam, "Cyclic Behavior and Energy Approach to the Fatigue of Shape Memory Alloys", *Journal of Mechanics of Materials and Structures*, Vol.4, No. 2, pp. 395–411, 2009.

215. Morin, C., Z. Moumni and W. Zaki, "Direct Numerical Determination of the Asymptotic Cyclic Behavior of Pseudoelastic Shape Memory Structures", *Journal of Engineering Mechanics*, Vol.137, No. 7, pp. 497–503, 2011.

216. Chrysochoos, A. and R. Peyroux, "Analyse Expérimentale et Modélisation Numérique des Couplages Thermomécaniques dans les Matériaux Solides", *Revue Générale de Thermique*, Vol.37, No. 7, pp. 582–606, 1998.

217. Peyroux, R., A. Chrysochoos, C. Licht and M. Löbel, "Thermomechanical Couplings and Pseudoelasticity of Shape Memory Alloys", *International Journal of Engineering Science*, Vol.36, No. 4, pp. 489–509, 1998.

218. Churchill, C., J. Shaw and M. Iadicola, "Tips and Tricks for Characterizing Shape Memory Alloy Wire: Part 4 - Thermo-Mechanical Coupling", *Experimental Techniques*, Vol.34, No. 2, pp. 63–80, 2010.

219. Zhang, X., P. Feng, Y. He, T. Yu and Q. Sun, "Experimental Study on Rate Dependence of Macroscopic Domain and Stress Hysteresis in Niti Shape Memory Alloy Strips", *International Journal of Mechanical Sciences*, Vol.52, No. 12, pp. 1660–1670, 2010.

220. Shaw, J. A. and S. Kyriakides, "Thermomechanical Aspects of Niti", *Journal of the Mechanics and Physics of Solids*, Vol.43, No. 8, pp. 1243–1281, 1995.

221. Entemeyer, D., E. Patoor, A. Eberhardt and M. Berveiller, "Strain Rate Sensitivity in Superelasticity", *International Journal of Plasticity*, Vol.16, No. 10-11, pp. 1269–1288, 2000.

222. Auricchio, F. and E. Sacco, "Thermo-Mechanical Modelling of a Superelastic Shape-Memory Wire Under Cyclic Stretching–bending Loadings", *International Journal of Solids and Structures*, Vol.38, No. 34-35, pp. 6123–6145, 2001.

223. Bouvet, C., S. Calloch and C. Lexcellent, "A Phenomenological Model for Pseudoelasticity of Shape Memory Alloys Under Multiaxial Proportional and Nonproportional Loadings", *European Journal of Mechanics - A/Solids*, Vol.23, No. 1, pp. 37–61, 2004.

224. Müller, C. and O. Bruhns, "A Thermodynamic Finite-strain Model for Pseudoelastic Shape Memory Alloys", *International Journal of Plasticity*, Vol.22, No. 9, pp. 1658–1682, 2006.

225. Rice, J. R., "Stresses Due to a Sharp Notch in a Work-hardening Elastic-plastic Material Loaded by Longitudinal Shear", *Journal of Applied Mechanics*, Vol.34, No. 2, pp. 287, 1967.

226. Knowles, J. K. and E. Sternberg, "Discontinuous Deformation Gradients near the Tip of a Crack in Finite Anti-plane Shear: an Example", *Journal of Elasticity*, Vol.10, No. 1, pp. 81–110, 1980.

227. Abeyaratne, R., "Discontinuous Deformation Gradients Away From the Tip of a Crack in Anti-Plane Shear", *Journal of Elasticity*, Vol.11, No. 4, pp. 373–393, 1981.

228. Rice, J. R. and R. Nikolic, "Anti-plane Shear Cracks in Ideally Plastic Crystals", *Journal of the Mechanics and Physics of Solids*, Vol.33, No. 6, pp. 595–622, 1985.

229. Knowles, J. K. and E. Sternberg, "Anti-plane Shear Fields with Discontinuous Deformation Gradients near the Tip of a Crack in Finite Elastostatics", *Journal of Elasticity*, Vol.11, No. 2, pp. 129–164, 1981.

230. Yuan, F. G. and S. Yang, "Analytical Solutions of Fully Plastic Crack-tip Higher Order Fields under Antiplane Shear", *International Journal of Fracture*, Vol.69, No. 1, pp. 1–26, 1995.

231. Jin, Z.-H. and C. Sun, "A Comparison of Cohesive Zone Modeling and Classical Fracture Mechanics Based on Near Tip Stress Field", *International Journal of Solids and Structures*, Vol.43, No. 5, pp. 1047–1060, 2006.

232. Wang, T. and K. Kishimoto, "Higher Order Fields for Damaged Nonlinear Antiplane Shear Notch, Crack and Inclusion Problems", *European Journal of Mechanics - A/Solids*, Vol.18, No. 6, pp. 963–986, 1999.

233. Silling, S. A., "Consequences of the Maxwell Relation for Anti-plane Shear Deformations of an Elastic Solid", *Journal of Elasticity*, Vol.284, No. 19, pp. 241–284, 1988.

234. Silling, S. A., "Dynamic Growth of Martensitic Plates in an Elastic Material", *Journal of Elasticity*, Vol.28, pp. 143–164, 1992.

235. Silling, S. A., "Numerical Studies of Loss of Ellipticity near Singularities in an Elastic Material", *Journal of Elasticity*, Vol.19, No. 3, pp. 213–239, 1988.

236. Amazigo, J. C., "Fully Plastic Crack in an Infinite Body Under Anti-Plane Shear", *International Journal of Solids and Structures*, Vol.10, No. 9, pp. 1003–1015, 1974.

237. Silling, S. A., "Numerical Analysis of Crack-tip Fields Using the Hodograph Transformation", *International Journal for Numerical Methods in Engineering*, Vol.28, No. 11, pp. 2503–2515, 1989.

238. Gao, X. L., "A Mathematical Analysis of the Elastoplastic Anti-Plane Shear Problem of a Power-Law Material and One Class of Closed-Form Solutions",

International Journal of Solids and Structures, Vol.33, No. 15, pp. 2213–2223, 1996.

239. Desindes, S. and S. Daly, "The Small-Scale Yielding of Shape Memory Alloys Under Mode III Fracture", *International Journal of Solids and Structures*, Vol.47, No. 5, pp. 730–737, 2010.

240. Long, R. and C.-Y. Hui, "Effects of Finite Chain Extensibility on the Stress Fields near the Tip of a Mode III Crack", *Proceedings of the Royal Society A: Mathematical, Physical and Engineering Sciences*, Vol.467, No. 2135, pp. 3170–3187, 2011.

241. Abaqus, "Uncoupled Heat Transfer Analysis", Abaqus Analysis User's Guide, Section: 6.5.2.

242. Matlab, "Reducing Parabolic Equations to Elliptic Equations", The MathWorks Inc., 2014.

243. Daly, S., G. Ravichandran and K. Bhattacharya, "Stress-Induced Martensitic Phase Transformation in Thin Sheets of Nitinol", *Acta Materialia*, Vol.55, No. 10, pp. 3593–3600, 2007.